Mode Spectrum Analysis for Microwave Components Formed by Nonstandard Waveguides

by

Seng Yong Yu

B.Sc., in Physics, East China Normal University, China, 1985
M.Sc., in Solid State and Optical Physics, Kumamoto University, Japan, 1996

A Thesis Submitted in Partial Fulfillment of the Requirements for the Degree of

DOCTOR OF PHILOSOPHY

In the Department of Electrical and Computer Engineering

Mode Spectrum Analysis for Microwave Components Formed by Nonstandard Waveguides

by

Seng Yong Yu

B.Sc., in Physics, East China Normal University, China, 1985
M.Sc., in Solid State and Optical Physics, Kumamoto University, Japan, 1996

Supervisory Committee

Dr. Jens Bornemann, Department of Electrical and Computer Engineering

Supervisor

Dr. Wolfgang J.R. Hoefer, Department of Electrical and Computer Engineering

Departmental Member

Dr. Poman P. M. So, Department of Electrical and Computer Engineering

Departmental Member

Dr. Colin Bradley, Department of Mechanical Engineering

Outside Member

Supervisory Committee

Dr. Jens Bornemann
Supervisor
Dr. Wolfgang J.R. Hoefer
Departmental Member
Dr. Poman P. M. So
Departmental Member
Dr. Colin Bradley
Outside Member

ABSTRACT

Microwave telecommunication systems employ a large number of waveguide components operating at microwave and millimeter-wave frequencies. Accurate design of these components for optimum performance of the overall system is critical and, therefore, computationally efficient and accurate numerical methods are indispensable. The objective of this work is to develop a framework for the computer-aided analysis and design of microwave components containing cross sections with arbitrarily positioned ridges.

A new formulation to obtain the eigenmode spectra of irregular waveguides is presented. The method uses modified modes of regular waveguide housings as expansion terms and leads to a classical eigenvalue problem. A constraint function is introduced to satisfy the boundary conditions for TM modes; TE modes are obtained straightforwardly. This procedure is then combined with a mode-matching code in order to analyze and optimize waveguide structures involving resonating components.

The general approach is applied to multiple ridged waveguide structures in rectangular and circular waveguide technologies. Convergence is demonstrated, and applicability of the developed algorithm is tested through the design of waveguide filters, transformers, polarizers and polarization-rotating components. Two new configurations of circular T-septum and key-shaped below-cutoff filters are introduced. Whenever possible, the designs are validated by independent means. Excellent agreement is obtained between the approach presented in this thesis and other full-wave field solvers.

List of Contents

List of Figures

List of Tables

Acknowledgments

I would like to express my sincere thanks and heartfelt gratitude to my supervisor, Dr. Jens Bornemann, Professor of Electrical and Computer Engineering at the University of Victoria, for the constant encouragement, valuable suggestions and advice as well as continues support that he provided during the entire duration of this study. His remarkable patience and continued confidence have made it possible for me to reach this successful conclusion.

My special thanks to Prof. Wolfgang J. R. Hoefer, whose presence throughout the tenure of my studies has been of great value.

Acknowledgements and gratitude are extended to Prof. Poman P.M. So and Prof. Colin Bradley for their great efforts in proofing and recognizing the contribution to the field that I have proposed in this thesis.

I wish to express my thanks to the external examiner, Prof. Qi-Jun Zhang, at the Department of Electronics, Carleton University for his precious suggestions and time spent on my thesis.

A word of gratitude to all my friends at the University of Victoria for their encouragement and help during the days of my studying. My special thanks to the members of the CADMIC group for their valuable critique, discussions and supports.

My heartfelt acknowledgments now go to my wife and daughter for their patience, forbearance and encouragements in the pursuit of my goal, both academic and otherwise. Finally, for the endless supports that I received from my parents, who are both no more but whose blessings, I am sure, are always with me.

Dedication

To my wife and daughter

Chapter 1 OVERVIEW

1.1 Introduction

RF/microwave and satellite communication systems employ a large number of waveguide components operating in the MHz to GHz frequency ranges. The accurate design of these components for optimum performance of the overall system is critical. To achieve this goal, computationally efficient and accurate numerical methods are indispensable and necessary in the design of components and subsystems, as well as in their optimization stages.

Among the large variety of potentially suitable numerical methods, two kinds of techniques may be grouped as finite-element or finite difference methods [1]–[3] and the method of moments [4] with eigenmode transformation technique. The advantage of the first group lies in the fact that they can be applied to a wide range of structures with less analytical and mathematical preprocessing. However, a price one has to pay is the numerical inefficiency compared to techniques partly involving analytical solutions. On the other hand, as one example of the second group, the mode matching method [5], [6] in conjunction with the generalized scattering matrix technique [7] has been found to be a more reliable and straightforward technique. A minor handicap of such methods is that they heavily rely on the knowledge of the mode spectra when nonstandard waveguide analysis is involved. In the past, the singular value technique has been mostly used to determine the mode spectrum of these nonstandard cross sections. Due to their feature of finding cutoff frequencies as zeros (or minima) of the determinant of a matrix, whose elements are functions of the frequency, the computational time is still fairly long, especially if many higher order modes must be computed. Several techniques have been proposed to formulate the task in form of a classical eigenvalue matrix problem [8], [9] to speed up the computations. In this thesis, a new algorithm for the calculation of the mode spectra of nonstandard waveguides is presented within a modal-based approach. The main procedure of the algorithm is to employ the method of moments to convert the wave

equation to a matrix eigenvalue problem using a set of known solutions of a standard waveguide as basis functions. Galerkin's method is applied to yield a standard eigenvalue matrix equation, which can be solved by conventional numerical routines [10], [11]. Both nonstandard rectangular and circular waveguides analyses are involved in this discussion.

This thesis begins with a brief introduction of the basic principles of an eigenvalue approach for rectangular waveguides with ridged features. These principles are then applied to the analysis of different rectangular ridged waveguides, followed by an eigenvalue analysis of ridged circular waveguides. In order to use a single coordinate system, conically shaped ridges rather than rectangular ones are considered in circular waveguide. The approach is then used to treat the discontinuity problem at the interface between the empty waveguide and ridged waveguide. To verify the computed mode spectrum and scattering parameters, standard mode-matching technique calculations and commercial software (HFSS, μWave Wizard) simulation results are chosen as comparators. Better performances in efficiency as well as good agreements are achieved.

Although only a few irregular waveguide problems are treated in this thesis, the basic framework for the eigenvalue approach combined with mode-matching techniques in nonstandard waveguide has been established and can now be extended to more general problems. This can be the subject of future work to analyze and design filters, transformers and many other waveguide components.

1.2 General Numerical Techniques

Waveguides of non-standard cross section are frequently employed in microwave and millimeter-wave front-end systems. In the literature, many techniques are presented for the analysis of these non-standard waveguides. The fundamental formulations are based on Maxwell's equations of electric and magnetic fields. For a homogeneous, isotropic, source free region, Maxwell's equations can be reformulated to obtain the equation

$$\nabla^2 \vec{\psi} + k^2 \vec{\psi} = 0$$

where $k = \omega\sqrt{\mu\varepsilon}$. For simple cases, it is possible to explicitly determine $\vec{\psi}$, the vector potential, from which the field in a homogeneous source free region can be evaluated. However, for some cases, where analytic solutions are not possible, a numerical evaluation must be sought. The numerical techniques themselves can be classified as time domain and frequency domain techniques, depending on whether the solution is obtained using spatial discretization (frequency domain method) alone or time discretization (time domain method) of Maxwell's equations. Some of these methods are discussed below.

1.2.1 Finite Difference Methods

There are two popular finite difference methods: Finite Difference Frequency Domain method (FDFD) and Finite Difference Time Domain method (FDTD) [12], [13]. In FDFD, the partial differential forms of Maxwell's equations are solved by approximating the derivatives of functions of continuous variables in space by finite differences using Taylor's series. Thus, the region of interest is divided into mesh points. The value of the function at each node is derived from the value of the functions at the neighboring points. The number of nodes is determined by the convergence in the value of the function. As in FDTD [14], the electromagnetic fields vary both in time and space. The partial derivatives with respect to time and space are approximated by finite differences. The frequency domain response is obtained from the time domain characteristic using Fourier transforms. More details can be found in [15].

This method is well known to be the least analytical. The fullwave mathematical derivation is minimal, and it can handle arbitrary and complicated structures including components involving open structures. However, the drawback is the numerical inefficiency. In order to get accurate solutions, the number of nodes usually must be increased extensively. Therefore, more memory space and computation time are necessary.

1.2.2 Finite Element Method (FEM)

The finite element method [3], [16] is similar to the finite difference method, but with variational features in the algorithm. In this method, the region of interest is divided into

a number of sub-regions called finite elements. A triangle is the simplest of the surface elements used to approximate most of the arbitrarily shaped structures. In this small element, the function is approximated by a polynomial with unknown coefficients. A Rayleigh-Ritz procedure transforms the variational form into a linear system of algebraic equations, which is then solved to obtain the unknown coefficients of the functions. Using a number of small elements with higher order polynomials to approximate the function, accurate solutions to field problems can be obtained using this method. Eigenvalue analysis of various structures like finlines in rectangular, ridged rectangular and circular waveguide components has been performed using FEM.

Even though the FEM procedure is general and can be used on arbitrary shapes, memory space and computational time required are still high. Another problem of finite methods is the existence of spurious zeros. Such zeros correspond to nonphysical field solutions. If the additional constraint $\nabla \cdot H = 0$ is added to the variational expression, it is possible to reduce or eliminate these zeros.

1.2.3 Transmission Line Matrix Method (TLM)

In the TLM method [17], [18], the electromagnetic field problem is converted to a three-dimensional equivalent network problem based on Huygen's principle of wave propagation. This method is essential for the simulation of wave propagation phenomena. After the time-domain response is obtained, the frequency response is found by Fourier transforms. This method is very general and can handle arbitrarily shaped structures and open boundaries with special absorbing boundary conditions. Also here, the time and memory space required during computation can be large for some problems.

1.2.4 Spectral Domain Approach (SDA)

The spectral domain approach [19] is well suited for the analysis of planar transmission lines such as microstrips, finlines and coplanar waveguides. It is one of the most preferred methods using a Fourier-transformed version of the integral equation. Basis functions are chosen to approximate the current in the metallization of the transmission line. Galerkin's procedure is then used to yield a homogeneous system of equations to

determine the propagation constants, current distribution and the characteristic impedance of the transmission lines. Except for the time-consuming procedure to find the zeros of the system determinant, this highly analytical method has excellent computational efficiency.

1.2.5 Method of Moments (MoM) and Galerkin's Method

This method [4], [20] is more analytical when compared to the above numerical methods. A sum of basis functions with unknown coefficients is used as an approximate solution to a differential or integral equation. The following step of the method of moments is to take the inner product of the basis functions with a set of testing functions. The result is a set of linear equations, which is solved in order to obtain an approximate solution to the problem. The choice of basis functions depends on the problem itself and the boundary conditions. The testing function can be a delta function, pulse function or any other function. If the basis functions and the testing functions are identical, then this procedure is referred to as Galerkin's method. The matrix size can be smaller than in other approaches, but the cost is that double integrals usually have to be evaluated for each matrix element. In general, a judicious choice of the functions used in this approach can minimize computation time and memory space and yet produce numerically accurate results. The method of moments may encounter poor convergence if the dimension of the matrix becomes too large.

1.2.6 Mode-Matching Technique (MMT)

The mode-matching technique [6], [21], [22] was initially developed for waveguide discontinuity problems. In this method, the fields on both sides of the discontinuity are first expanded in terms of their respective modal functions. Using the continuity condition of the field at the interface of regions along with applying the orthogonality property of the modal functions, results in a set of algebraic equations. The solution of these algebraic equations yields the eigenvalues and scattering parameters of the fundamental and higher order modes. These are the values of the propagation constants that make the determinant of the system of equations vanish. Also, the modal representation of the fields directly provides the generalized scattering matrix, which

enables one to evaluate the field at any point close to the discontinuity including the effects of evanescent higher order modes along with the propagating fundamental mode. Consequently, a rigorous analysis of the component is possible by cascading the generalized scattering matrices of subsequent discontinuities.

The mode-matching technique has been proved to be a reliable and rigorous numerical technique to design waveguide components. If the modal functions can be expressed analytically, this method rapidly depicts the characteristics of components. However, when the applications involve arbitrarily shaped structures, the mode-matching method has less handling ability due to the absence of explicit expressions for the modal functions. Another drawback of this method is the relative convergence problem found in the evaluation of the matching equations.

1.2.7 Summary

A brief introduction of most commonly used numerical techniques in microwave systems is given above. Each method comes with its own advantages and disadvantages. For instance, the finite element method may petition a large amount of computation resources to fulfill an accurate simulation. But it is a versatile technique. In contrast, the mode-matching technique is much more efficient. However, it can only handle those structures where the modal functions can be expressed analytically. In view of the advantages of certain numerical methods, many researchers have focused attention on the combination of a number of techniques to accelerate numerical processing. Such hybrid techniques are attractive as they apply to more applications in microwave components design.

In this thesis, various numerical techniques are firstly presented in order to find a suitable method for nonstandard waveguide analysis. The mode-matching technique is believed to be a fast and rigorous numerical tool. Combined with singular value decomposition, this techniques searches for the zeros of the system determinant, which contain the unknown wavenumbers. This type of numerical processing is usually costly both in computation time and resources. Another approach is based on the moment method of the integral formulation associated with Galerkin's method, in which a wave function is expanded in

a sum of known standard waveguide functions. For instance, Omar and Schünemann [8] and Lin, Li, Yeo and Leong [9] propose different modules to implement this method. In [8], edge conditions must be introduced which do not allow for an arbitrary placement and numbers of ridges. To the best of the author's knowledge, the method proposed in [9] has not been applied to waveguide component design.

To achieve the goal of accuracy and efficiency, a new and more general design is presented in this thesis by combining the two methods published in [8], [9]. With the new method developed in this thesis, the eigenmodes of nonstandard cross-section waveguides are expressed in terms of standard waveguide modes. (Note that in this thesis, 'standard' refers to a waveguide for which analytical solutions of eigenmodes exist.) The resulting eigenvalue system covers a large variety of cross sections involving metal inserts in standard waveguides. Additional to the modal spectrum analysis, a prototype design for components using non-standard waveguides is proposed. The mode-matching method is used to generate the scattering matrix and circuits' characteristics. Comparisons with results obtained from commercially available field solvers and other numerical techniques are carried out to validate the theory proposed.

1.3 Techniques for Nonstandard Waveguide Analysis

Over the last two decades, an increasing number of passive waveguide devices have appeared with an arbitrary cross section defined by linear, circular, and or elliptical arcs. For instance, ridged rectangular and ridged circular waveguides, as well as cross-shaped irises are frequently found in dual-mode and/or dielectric-loaded resonator waveguide filters. Multi-ridged rectangular waveguides have been also employed as tuning elements in reentrant coaxial filters [71]. Recently, and due to the utilization of the most common manufacturing techniques of waveguide components, the presence of rounded corners in rectangular waveguides has been under investigation in both guided and filter applications [72], [73]. The electromagnetic-wave propagation in hollow conducting waveguides of arbitrary cross section has become a problem of considerable practical interest, and many different approaches dealing with the calculation of the full modal spectrum of such waveguides have been published in the microwave engineering

literature. Over the past years, several techniques were introduced in order to cope with the efficient modal computation of particular arbitrarily shaped waveguides such as non-symmetric uniform waveguides or triangular-waveguides. The keys are to calculate the distribution of the resonant modes and frequencies of a two-dimensional structure, which is equivalent to finding the modal fields and corresponding cutoff wave numbers. To achieve this goal, the approach of equivalent circuits is historically developed. In the literature, the analysis of electromagnetic characterization of ridge waveguides is presented by Cohn [23] and Hopfer [24]. However, the integral transform and variational techniques employed within the equivalent circuit approach are only valid for the dominant mode. This leads to low accuracy for problems of multi-discontinuity structures.

Since then, a variety of numerical and analytical methods have been developed to provide rigorous theoretical solutions of electromagnetic fields in ridged waveguide structures. These include the finite element method [25], method of moments [26], mode matching technique [22], and all subsets of variations [27]-[36], each with its own unique advantages and disadvantages. From a mathematics' point of view, there are two main group of techniques for solving the modal problem under consideration: the first one is based on the solution of integral equations through different methods and solves for the zeros of the determinant of the system matrix. The second one consists of field expansions in term of normal modes of hollow waveguide which leads to a solution of classical eigenvalue matrix equation.

Obtaining the numerical solution of a problem involving a source-free region is one of the most frequent tasks in electromagnetic field analysis. Among the first category, formulations are based on expansions in space-harmonics functions, which finally lead to a homogeneous matrix equation. The solutions, i.e., the roots of the characteristic equation, must then be found by means of a search procedure. A number of different approaches have been presented over the years and their solutions combined with different forms of modal analysis. These include standard Ritz-Galerkin approaches [37], [38], the finite-element technique [36], the electric and magnetic field integral equation

technique [29], [31], transverse resonant technique [30], [35], and others such as neural network models. These numerical methods have been successfully applied to the analysis and prediction of the characteristics of nonstandard waveguides and their applications. However, there are two drawbacks in this category. One disadvantage lies in the fact that these methods partly rely on the use of harmonic expansion formulations for the transverse fields; thus, they are not flexible for treating arbitrarily shaped ridged waveguides. Another main limitation is the long computation time required for the search of cutoff frequencies for the higher order modes. Due to the nature of the formulation, it is the issue of locating the zeros of the determinant in the homogeneous matrix equation in the form of $A \cdot x=0$. Some efficient methods are presented in [39]-[41] to speed up the process of finding the accurate solutions. Furthermore, a singular-value decomposition method is developed to ensure that zeros are clearly distinguished, thus, no false solution is produced and no true eigenvalue is missed [42], [43]. It should be noted that these methods have been successfully applied to T-junctions and waveguide corners, as well as other complex waveguides components, and accomplished the desired goals [44]-[46].

The classical eigenvalue approach is the second category which consists of techniques based on the solution of integral equations by algorithms such as the method of moments. Omar and Schunemann applied the generalized spectral domain technique, which uses the mode distributions of the surrounding regular waveguides as expansion and testing functions, to analyze rectangular waveguides with metal inserts [47]. However, it was found that in the presence of sharp edges, the method requires the use of edge-conditioned basis functions, which limits general applicability to structures with predefined edge structure. An interesting approach, which leads to a classical symmetric eigenvalue matrix equation, is presented in [48], [49]. However, the use of polynomial approximations involving Gamma functions limits efficient code implementation and, therefore, only simple discontinuities have been presented so far [50], [51].

The classical eigenvalue approach might be less efficient when applied to analyzing muti-ridged cross-section waveguides. The formulations usually lead to large-size standard

eigenvalue matrix problems, thus in some cases, do require time-consuming procedures for the computation of the required cutoff frequencies.

In view of the advantages of different numerical techniques, many researchers recently focused attention on hybrid techniques as a combination of two different approaches. These procedures have been applied when there are complex elements in the waveguide housing, or, in general, to problems which involve mixed systems. When combining MoM with MMT, the eigenvalue analysis of arbitrarily shaped structures is done using MoM. Subsequently, the discontinuity from a structure that is well suited for a MMT analysis is made possible by a combination of techniques. Since the structure that is sandwiched on either side by a region where fields can be expressed as modes, application of the matching condition and orthogonality of modes results in integrals which can be performed as summation. Therefore, the modal representation gets directly incorporated, and a generalized scattering matrix is obtained. Such hybrid techniques are attractive due to the ability to handle structures that are arbitrarily shaped.

In this work, a combination method which solves first a two-dimensional problem by an eigenvalue method and then the third dimension through mode-matching will be examined.

1.4 Research Objective

Since rigorous analysis and design of microwave components, like filters, transformers, matching networks, is essential for the modern communication industry, this research focuses on the computer-aided analysis and design of certain microwave passive components used in telecommunication systems. The main objective has been to develop computer-aided design algorithms for the design of components in waveguide technology using a field theoretical approach. The numerical technique used in this work for the design and analysis of waveguide components is a variation of the Method of Moments in integral form. By combing the mode spectrum eigenvalue formulation with the MMT, a flexible algorithm is developed to analyze a variety of waveguide components. The fact that this technique lends itself to the approach of handling basic discontinuities makes it

suitable for handling components composed of many cascaded discontinuities. Also, an integrated system can be analyzed rigorously once the sub-components have been individually analyzed. The most important feature of the approach is that it is rigorous and yet enables the optimization of the parameters of an initial design.

The present work begins with a study of the well-known structures in rectangular waveguides. The principles of this study are later utilized to rigorously design components in nonstandard waveguide technologies. In order to validate the proposed algorithm's correctness, some numerical results have been compared with those obtained with commercially available field solvers and other numerical tools. The target of this research is to make contributions in the area of computer-aided design of passive waveguide networks.

1.5 Organization of the Thesis

As mentioned in previous sections, this research adopts a two-phase approach in the development of computer-aided design algorithms for irregular waveguide components. The following chapters present the theoretical treatment of waveguide discontinuities and then a series of rectangular and circular waveguide components which incorporate such discontinuities. A few design examples will be used to demonstrate the applicability of the algorithm upon validation by measured data and/or other simulation tools and software.

Chapter 2 begins with the study of the fundamental concepts and formulations of the mode-matching technique. A full-wave analysis of the T-septum waveguide is performed to generate the mode spectrum and propagation characteristics. Once the rectangular-to-T-septum waveguide discontinuity is solved, a complete numerical algorithm can be developed.

Chapter 3 gives full details of a ridged rectangular waveguide structure using the eigenvalue mode spectrum analysis. A classical eigenvalue approach is employed to handle the irregular waveguide cross sections. By combining this method with a mode-

matching technique, the generalized scattering matrix is determined. The complete algorithm is then applied to analyze a regular-ridged-regular waveguide structure. The proposed method is validated by comparing the obtained results with those computed via other simulation software.

A rigorous analysis of multiple transverse discontinuities in rectangular waveguide is presented in Chapter 4. The fundamental formulations derived in Chapter 3 are expanded to include the theoretical and numerical analysis of nonstandard multi-ridged waveguide structures. After the validation of convergence of the multiple-ridged waveguide cross-section analysis, the design of waveguide filters, waveguide transformers, below-cutoff waveguide filters, and a 90-degree waveguide twist component are featured.

Chapter 5 presents a study on circular ridged waveguide structures. The mathematical approach used for multiple ridged rectangular waveguides is extended to multiple ridged circular waveguides, and the eigenvalue mode-spectrum analysis involving Bessel functions is applied. Based on the complete theory, designs of a circular ridged waveguide polarizer, novel below-cutoff circular ridged waveguide filters and a new polarization rotator demonstrate the validity of the algorithms presented in this chapter.

The final Chapter 6 summarizes the proposed algorithms and theory. Although only two-port problems are treated in this thesis, the basic framework for the eigenvalue spectrum analysis method in both rectangular and circular waveguides has been established and can be extended to multi-ports problems. This will be the subject of future work to analyze and design waveguide components.

1.6 Contributions of Thesis

The overall contribution of this thesis is the development of an accurate numerical technique, which combines the method of moments and mode-marching techniques for the design of passive components in nonstandard waveguide technology.

- First, a new method that uses well-known modes of empty regular waveguides to find mode distributions of irregular waveguides is proposed.

- Secondly, a new two-dimensional formulation to enforce boundary conditions for the TM modes calculations of irregular waveguides is presented.
- And finally, this method is combined with MMT routing schemes for the analysis and design of rectangular and circular waveguide components for wide-band and narrow-band applications.

Chapter 2 TRADITIONAL MODE-MACHING APPROACH

2.1 Introduction

In the analysis and design of passive microwave components, a variety of numerical and analytical methods have been applied. The mode-matching technique is preferably used where the structures in question have regular boundary cross-sections with discontinuities in the direction of propagation. The most important advantage of this method is that the analysis includes higher-order mode excitations at the discontinuities, thus accounting for the contributions of propagating and evanescent TE/TM modes to the electromagnetic field [52]. This traditional method is also beneficial in the sense that it can be easily incorporated with other numerical techniques to solve for a waveguide's propagation constants, cutoff frequencies, or characteristic impedances. Combining the mode-matching technique with optimization algorithms, it can be made into a design tool. However, it should be noted that the mode-matching technique can straightforwardly handle only those structures where the modal functions can be expressed analytically. This means that highly arbitrary sharped structures cannot be analyzed using this method. Only simple irregular cross sections have been analyzed using modal techniques; an example will be given in Section 2.2.

The traditional mode-matching method has proven effective in numerous waveguide discontinuities problems. Generally, in mode-matching techniques, the unknown electromagnetic fields on both sides of the discontinuity are first expanded in terms of their respective modal functions and then matched at the common interface by applying field continuity conditions. This approach eventually leads to a set of linear simultaneous equations for the unknown modal coefficients and, hence, the generalized scattering matrix of the discontinuity. In the design algorithm, the Generalized S-matrix Method [52], which combines the mutual interactions of all discontinuities involved via the dominant and high-order modes, is used routinely to characterize cascaded and interconnected discontinuities. In this chapter, the basic concept of mode-matching will

be explained and illustrated for a T-septum waveguide discontinuity problem. Further discussion topics such as power normalization, generalized scattering matrix, and cascaded discontinuities are involved. The chapter concludes with comments on this general mode-matching technique.

2.2 Transverse Analysis

The basic problem in electromagnetic applications is to solve Maxwell's equations under the constraints of boundary conditions. For some simple boundary value problems involving standard waveguides, such as rectangular, circular or elliptic waveguides, a direct analytical solution is possible. For other more complicated cross sections, referred to as nonstandard waveguides, a numerical evaluation is the only approach.

Consider a homogeneous, isotropic and source-free waveguide structure. Then the electric and magnetic field vectors are described by Maxwell's equations:

$$\begin{aligned} \nabla \times \overline{E} &= -j\omega\mu\overline{H} \\ \nabla \times \overline{H} &= j\omega\varepsilon\overline{E} \\ \nabla \cdot \overline{E} &= 0 \\ \nabla \cdot \overline{H} &= 0 \end{aligned} \tag{2.1}$$

The solutions can be derived from the electric and magnetic vector potentials $\vec{\psi}^{e}$ and $\vec{\psi}^{h}$, respectively, which satisfy the Helmholtz equations

$$\begin{aligned} \vec{E} &= -\nabla \times \vec{\psi}^{e} + \frac{1}{j\omega\varepsilon}\nabla \times \nabla \times \vec{\psi}^{h} \\ \vec{H} &= \nabla \times \vec{\psi}^{h} + \frac{1}{j\omega\mu}\nabla \times \nabla \times \vec{\psi}^{e} \\ \nabla^2 \vec{\psi}^{e(h)} &+ k^2 \vec{\psi}^{e(h)} = 0 \end{aligned} \tag{2.2}$$

where $k = \omega\sqrt{\mu\varepsilon}$. As mentioned earlier, it is possible to determine vector potentials $\vec{\psi}^{e}$ and $\vec{\psi}^{h}$ analytically for simple cross sections. However, for most cases in modern waveguide technology, analytic solutions are not possible and numerical evaluations must be sought. The numerical techniques involved can be classified as frequency-

domain and time-domain techniques depending on whether the solution is obtained using spatial discretization alone or including time discretization as well solving Maxwell's equations. These methods are, for example, the Finite Element Method, the Boundary Element Method, the Finite Difference Method, the Integral Equation Method, the Method of Moments, the Transmission Line Matrix Method and the Mode-Matching Method, each with its own unique advantages and disadvantages (c.f. Chapter 1). The choice of the numerical method depends largely on the geometry of the structure itself. When investigating three-dimensional waveguide geometries of arbitrary shape, where the distribution of the electromagnetic field cannot be described in closed form, one must inevitably resort to numerical methods.

For the class of problems in which the waveguide components contain discontinuities from fixed boundary cross sections, such as rectangular, circular, elliptical, etc., specific solutions for the electromagnetic field exist due to the careful selection of the analytical and numerical methods. As stated earlier, among the variety of analytical and numerical methods, the mode-matching technique has been highly preferred.

Fig. 2.1 shows the geometry of the T-septum waveguide with corresponding regional subdivisions for the mode-matching formulation. The coordinate system is set-up for the two-dimensional analysis of this waveguide.

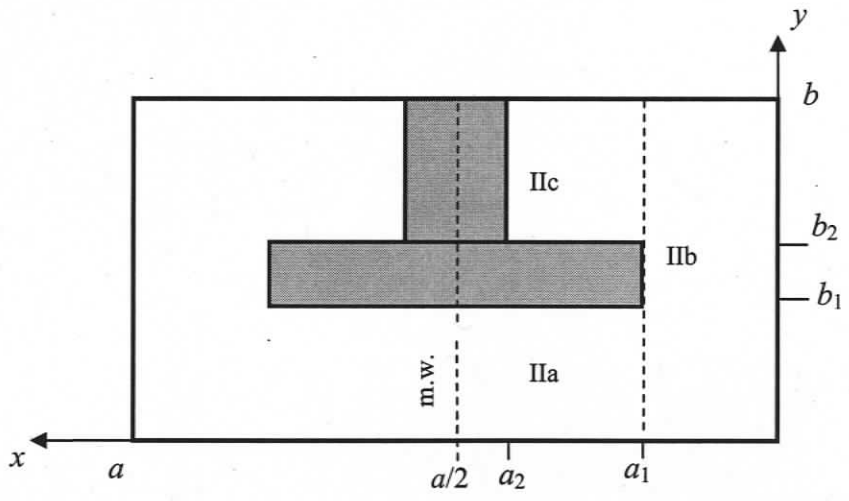

Fig. 2.1 Cross section of T-septum waveguide.

The solution to the electromagnetic field in an homogeneous source-free waveguide is derived from the electric and magnetic vector potentials $\vec{\psi}^e$ and $\vec{\psi}^h$, respectively, and these are chosen such that they individually satisfy the Helmholz equations. In the above coordinate system, if the waveguide axis is parallel to the z-direction, the field is readily divided into a sum of TE and TM modes, which can be represented by the scalar wave potential ψ^h and ψ^e, respectively. They can be written as

$$\psi^h(x,y,z) = \sum_{q=1}^{\infty} \sqrt{Y_q^h} T_q^h(x,y) \zeta_q^h(z) \tag{2.3}$$

$$\psi^e(x,y,z) = \sum_{p=1}^{\infty} \sqrt{Z_p^e} T_p^e(x,y) \zeta_p^e(z)$$

where Z_p^e and Y_q^h are the wave impedance and admittance, respectively. The Helmholtz equations with boundary conditions are:

$$\nabla_z^2 \psi^{h(e)} + k_c^2 \psi^{h(e)} = 0$$

$$\frac{\partial \psi^e}{\partial n} = 0 \tag{2.4.a}$$

$$\psi^h = 0$$

where the derivative is taken in a direction normal to the waveguide surface. The functions $\zeta^{e,m}$, which generally contain two unknown coefficients, are solutions to the second-order ordinary differential equation

$$\frac{d^2\zeta}{dz^2} + k_z^2 \zeta = 0 \tag{2.4.b}$$

The cutoff wavenumbers are related to the propagation constants by

$$k_c^2 + k_z^2 = k^2 \tag{2.4.c}$$

where $k^2 = \omega^2 \mu\varepsilon$. The indices p and q in eq. (2.3) are ordered in increasing mode cutoff frequencies. The propagation constants are determined from eq. (2.4.c) after the cutoff wavenumbers are found by solving the boundary value problem.

When applying the mode-matching method to a waveguide discontinuity problem, the junction is subdivided into suitable regions. The TE mode cross-section functions in their respective subregions can be described as

$$T^{hIIa}(x,y)=\sum_{r=0}^{R}A_r^{IIa}\sqrt{\frac{2}{b_1}}\frac{\sin\left\{k_{xr}^{hIIa}(x-a/2)\right\}}{k_{xr}^{hIIa}}\frac{\cos(r\pi y/b_1)}{\sqrt{1+\delta_{0r}}}$$

$$T^{hIIb}(x,y)=\sum_{s=0}^{S}A_n^{IIa}\sqrt{\frac{2}{b}}\cos(k_{xs}^{hIIb}x)\frac{\cos(s\pi y/b)}{\sqrt{1+\delta_{0s}}} \tag{2.5}$$

$$T^{hIIc}(x,y)=\sum_{t=0}^{T}A_t^{IIc}\sqrt{\frac{2}{b-b_2}}\cos\left\{k_{xt}^{hIIc}(x-a_2)\right\}\frac{\cos[(t\pi(y-b_2)/(b-b_2)]}{\sqrt{1+\delta_{0t}}}$$

where δ_{0i} is the Kronecker delta function. The respective cross-section functions for the TM modes are:

$$T^{eIIa}(x,y)=\sum_{r=1}^{R}D_r^{IIb}\sqrt{\frac{2}{b_1}}\cos\left\{k_{xr}^{eIIa}(x-a/2)\right\}\sin(\frac{r\pi}{b_1}y)$$

$$T^{eIIb}(x,y)=\sum_{s=1}^{S}D_s^{IIb}\sqrt{\frac{2}{b}}\frac{\sin(k_{xs}^{eIIb}x)}{k_{xs}^{IIb}}\sin(\frac{s\pi}{b}y) \tag{2.6}$$

$$T^{eIIc}(x,y)=\sum_{t=1}^{T}D_t^{IIc}\sqrt{\frac{2}{b-b_2}}\frac{\sin\left\{k_{xt}^{hIIc}(x-a_2)\right\}}{k_{xt}^{mIIc}}\sin\left\{\frac{t\pi}{b-b_2}(y-b_2)\right\}$$

with

$$\begin{Bmatrix}(k_{xr}^{hIIa,eIIa})\\(k_{xs}^{hIIb,eIIb})\\(k_{xt}^{hIIc,eIIc})\end{Bmatrix}^2=\omega^2\mu_0\varepsilon_0-\begin{Bmatrix}(k_{yr}^{IIa})\\(k_{ys}^{IIb})\\(k_{yt}^{IIc})\end{Bmatrix}^2 \tag{2.7}$$

and

$$\begin{Bmatrix}(k_{yr}^{IIa})\\(k_{ys}^{IIb})\\(k_{yt}^{IIc})\end{Bmatrix}^2=\begin{Bmatrix}(r\pi/b_1)\\(s\pi/b)\\(t\pi/(b-b_2)\end{Bmatrix}^2$$

The field matching conditions for both the TE and TM modes at the common interface of $x=a_1$ are

$$\left.\begin{aligned}\overline{E_{x,y}^{IIa}} &= \overline{E_{x,y}^{IIb}} \\ \overline{H_{x,y}^{IIa}} &= \overline{E_{x,y}^{IIb}}\end{aligned}\right\} \text{ at } x=a_1 \quad \text{and} \quad \left.\begin{aligned}\overline{E_{x,y}^{IIc}} &= \overline{E_{x,y}^{IIb}} \\ \overline{H_{x,y}^{IIc}} &= \overline{H_{x,y}^{IIb}}\end{aligned}\right\} \text{ at } x=a_1 \tag{2.8}$$

The matching operations for subregion functions, as well as their derivatives with respect to x, yield two matrix equations, each relating the unknown amplitude coefficients to each other. Thus, homogeneous characteristic matrix equations are derived for the unknown coefficients A^{IIb} and D^{IIb} in region IIb first. These are

$$\begin{aligned}&\Big[diag\left(-k_{xs}^{hIIb}\sin k_{xs}^{hIIb}a_1\right)\\ &-(J^{h(IIa-IIb)})^T diag\left(-k_{xr}^{hIIa}\cot k_{xr}^{hIIa}(a_1-a/2)\right)J^{h(IIa-IIb)}diag\left(\cos k_{xs}^{hIIb}a_1\right)\\ &+J^{h(IIb-IIc)}diag\left(-k_{xt}^{hIIc}\tan k_{xt}^{hIIc}(a_1-a_2)\right)(J^{h(IIb-IIc)})^T diag\left(\cos k_{xs}^{hIIb}a_1\right)\Big]A^{IIb}=0\end{aligned} \tag{2.9}$$

and

$$\begin{aligned}&\left[diag\left(\frac{-\sin k_{xs}^{eIIb}a_1}{k_{xs}^{eIIb}}\right)\right.\\ &-(J^{e(IIa-IIb)})^T diag\left(\frac{\cot k_{xr}^{eIIa}(a_1-a/2)}{k_{xr}^{eIIa}}\right)J^{e(IIa-IIb)}diag(\cos k_{xs}^{eIIb}a_1)\\ &\left.+J^{e(IIb-IIc)}diag\left(\frac{\tan k_{xt}^{eIIc}(a_1-a_2)}{k_{xt}^{eIIc}}\right)(J^{e(IIb-IIc)})^T diag(\cos k_{xs}^{eIIb}a_1)\right]D^{IIb}=0\end{aligned} \tag{2.10}$$

where diag (·) denotes a diagonal matrix, and the coupling matrices are:

$$\begin{aligned}J_{rs}^{h(IIa-IIb)} &= \int_0^{b_1}\sqrt{\frac{2}{b_1}}\sqrt{\frac{2}{b}}\frac{\cos k_{yr}^{hIIa}y}{\sqrt{1+\delta_{0r}}}\frac{\cos k_{ys}^{hIIb}y}{\sqrt{1+\delta_{0s}}}dy\\ J_{rs}^{h(IIb-IIc)} &= \int_{b_2}^{b}\sqrt{\frac{2}{b}}\sqrt{\frac{2}{b-b_2}}\frac{\cos k_{ys}^{hIIb}y}{\sqrt{1+\delta_{0s}}}\frac{\cos k_{yt}^{hIIc}(y-b_2)}{\sqrt{1+\delta_{0t}}}dy\\ J_{rs}^{e(IIa-IIb)} &= \int_0^{b_1}\sqrt{\frac{2}{b_1}}\sqrt{\frac{2}{b}}\sin k_{yr}^{eIIa}y\sin k_{ys}^{eIIb}ydy\\ J_{rs}^{e(IIb-IIc)} &= \int_{b_2}^{b}\sqrt{\frac{2}{b}}\sqrt{\frac{2}{b-b_2}}\sin k_{ys}^{eIIb}y\sin k_{yt}^{eIIc}(y-b_2)dy\end{aligned} \tag{2.11}$$

The terms in the square brackets in (2.9) and (2.10) represent the characteristic matrices for the TE and TM modes, respectively, and must be solved for the zeroes of the determinant by varying the frequency f to specify the corresponding mode cutoff frequencies. The amplitude coefficients A^{IIb} and D^{IIb} may once again be determined where a zero is detected. By using the coupling matrices and diagonal matrices, these, in turn, are related to the amplitude coefficients A^{IIa}, D^{IIa}, A^{IIc} and D^{IIc} in regions IIa and IIc,

$$
\begin{aligned}
A^{IIa} &= diag\left(k_{xr}^{hIIa}\csc k_{xr}^{hIIa}(a_1-a/2)\right)J^{h(IIa-IIb)}diag\left(\cos k_{xs}^{hIIb}a_1\right)A^{IIb} \\
D^{IIa} &= diag\left(\frac{-\csc k_{xr}^{eIIa}(a_1-a/2)}{k_{xr}^{eIIa}}\right)J^{e(IIa-IIb)}diag\left(\cos k_{xs}^{eIIb}a_1\right)D^{IIb} \\
A^{IIc} &= diag\left(k_{xt}^{hIIc}\sec k_{xt}^{hIIc}(a_1-a_2)\right)\left(J^{h(IIb-IIc)}\right)^T diag\left(\cos k_{xs}^{hIIb}a_1\right)A^{IIb} \\
D^{IIc} &= diag\left(\cos k_{xt}^{eIIc}(a_1-a_2)\right)\left(J^{e(IIb-IIc)}\right)^T diag\left(\cos k_{xs}^{eIIb}a_1\right)D^{IIb}
\end{aligned}
\tag{2.12}
$$

and, hence, the cross-section functions are determined completely.

Since the general homogeneous matrix equations (2.9), (2.10) are in the form of $(A)\square x = 0$, the evaluation of $\det(A) = 0$ could be computationally expensive for most numerical calculation techniques. Two algorithms are employed to located the zeros of the determinant for these characteristic equations. The first algorithm is based on the sign reversal of a logarithmic function of the determinant, given by

$$f\left(\det(A)\right) = \beta \cdot \mathrm{sgn}[\det(A)] \cdot \log_{10}[1+|\det(A)|]$$

where β is a scaling factor, sgn is the signum function, and $\det(A)$ denotes the determinant. This is especially useful when the actual value of the determinant become very large [53]. The second algorithm is a minimum search algorithm for the smallest singular value. The characteristic matrix A, for which the zeros of the determinant are to be found, is decomposed into three matrices [54]

$$A = W\Sigma V^T$$

where Σ is a diagonal matrix formed by the singular values σ ordered in decreasing value, and where the columns of W and V are the left and right singular vectors of A, respectively. Using the property

$$\sigma_{\min} = 0, \quad \text{if and only if} \quad \det(A) = 0$$

the algorithm searches over the frequency spectrum for the minima of the smallest element $\sigma_{\min}$ in Σ. Singular value decomposition is the appropriate procedure applied to the matrix A. However, whether all minima are found, particularly when solutions are very close in frequency, depends largely on the efficiencies and computational complexity of the search algorithm.

By taking into account all mode contributions of the subregions, the above two-dimensional mode-matching formulation in conjunction with the singular value decomposition has successfully been incorporated into component design to calculate the cutoff frequencies and propagation constants of the T-septum waveguide [53]. The obtained modal amplitude coefficients provide precise knowledge for the longitudinal mode-matching analysis, in which they are used for the efficient cascading of discontinuities in the propagation direction. Therefore, the mode-matching formulation to compute eigenvalues and eigenfunctions has been accepted to be a fundamental numerical algorithm to solve the cross-sectional boundary value problems of irregular waveguides.

2.3 Longitudinal Analysis

This section presents the basic procedure for applying the mode-matching technique in longitudinal direction and obtaining the generalized modal scattering matrix for the step discontinuity formed by connecting a rectangular and a T-septum waveguide. The analysis of such a discontinuity or other longitudinal discontinuities involves the following steps:

1. The fields on both sides of the discontinuity are expanded in terms of a series of modes of incident and reflected waves.
2. All mode amplitudes are normalized such that the magnitude of power carried by each mode is unity.
3. The continuity conditions for the transverse components of the electric and magnetic fields are imposed.

4. Using the principle of orthogonality of the modes, the equations of the continuity conditions are transformed into matrix equations relating the expansion coefficients of incident and reflected waves at the discontinuity.
5. The matrices are rearranged and inverted suitably to obtain the generalized scattering matrix which describes the discontinuity in terms of the dominant and higher order modes.

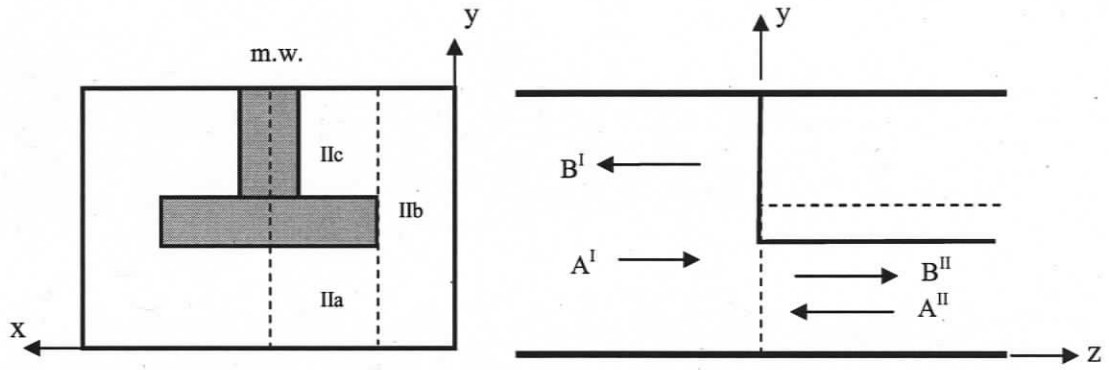

Fig. 2.2 Geometry of a rectangular to T-septum waveguide discontinuity.

The geometry of the rectangular to T-septum waveguide discontinuity is shown in Fig. 2.2. The rectangular waveguide (region I) and the T-septum waveguide (region II) are joined at $z = 0$ to create a building block discontinuity of waveguide components. The solutions to the Helmholtz equation for each region, i = I and II, are

$$\Psi^{hi}(x,y,z) = \sum_{p=1}^{n^{hi}} \sqrt{Z_p^{hi}}\, T_p^{hi}(x,y)\left\{A_p^{hi}\exp(-jk_{zp}^{hi}z) + B_p^{hi}\exp(+jk_{zp}^{hi}z)\right\} \tag{2.13}$$

$$\Psi^{ei}(x,y,z) = \sum_{q=1}^{n^{ei}} \sqrt{Y_q^{ei}}\, T_q^{hi}(x,y)\left\{A_q^{ei}\exp(-jk_{zq}^{ei}z) - B_q^{ei}\exp(+jk_{zq}^{ei}z)\right\}$$

where $A^{hi,ei}, B^{hi,ei}$ are the amplitudes of the forward and backward traveling waves. Considering the magnetic-wall symmetry introduced in Fig. 2.1 and Fig. 2.2, the cross-section functions of waveguide I are well-known rectangular waveguide modes

$$T_p^{hI}(x,y) = C_{mn}^{I}\cos\left(\frac{(2m-1)\pi}{a}x\right)\frac{\cos\left(\dfrac{2n\pi}{b}y\right)}{\sqrt{1+\delta_{0n}}} \tag{2.14}$$

$$T_q^{eI}(x,y) = D_{mn}^{I} \sin\left(\frac{(2m-1)\pi}{a}x\right)\sin\left(\frac{2n\pi}{b}y\right)$$

where $m,n \rightarrow p$, $m,n \rightarrow q$, and m, $n = 0,1,2,\ldots$; a, b are the waveguide dimensions. For the T-septum waveguide II, the cross-section functions are a sum of the functions of each subregion,

$$T_p^{hII}(x,y) = \sum_{r=1}^{n^{hIIa}} T_r^{hIIa}(x,y) + \sum_{s=1}^{n^{hIIb}} T_s^{hIIb}(x,y) + \sum_{t=1}^{n^{hIIc}} T_t^{hIIc}(x,y) \tag{2.15}$$

$$T_q^{eII}(x,y) = \sum_{r=1}^{n^{eIIa}} T_r^{eIIa}(x,y) + \sum_{s=1}^{n^{eIIb}} T_s^{eIIb}(x,y) + \sum_{t=1}^{n^{eIIc}} T_t^{eIIc}(x,y)$$

The TE and TM modes are ordered in increasing cutoff frequencies with $m,n \rightarrow r$, $m,n \rightarrow s$, $m,n \rightarrow t$. The subregions cross-section functions are those of (2.5), (2.6).

The cross-section functions in both region I and II are now normalized by

$$\iint_{S^i} \left[\nabla T^{hi,ei}\right]^2 ds = 1 \tag{2.16}$$

so that the power carried by a mode through the cross section S^i is

$$P^{hi,ei} = \begin{cases} 1W & \text{for propagating modes} \\ +j1W & \text{for evancescent TE modes} \\ -j1W & \text{for evancescent TM modes} \end{cases} \tag{2.17}$$

if the corresponding wave amplitude equals $1\sqrt{W}$, where W is the unit of power.

To apply the field continuity conditions, the following equations must be satisfied at the joined position $z = 0$.

$$\left.\begin{array}{ll} \vec{E}_T^{I} = \vec{E}_T^{II} & \text{on } IIa, IIb, IIc \\ \vec{E}_T^{I} = 0 & \text{otherwise} \\ \vec{H}_T^{I} = \vec{H}_T^{II} & \text{on } IIa, IIb, IIc \end{array}\right\} \text{at } z = 0 \tag{2.18}$$

This yields the modal scattering matrix of the discontinuity

$$\begin{bmatrix} B^I \\ A^{II} \end{bmatrix} = \begin{bmatrix} S_{11} & S_{12} \\ S_{21} & S_{22} \end{bmatrix} \cdot \begin{bmatrix} A^I \\ B^{II} \end{bmatrix} \tag{2.19}$$

where

$$\begin{aligned} S_{11} &= -\left[I + MM^T\right]^{-1}\left[I - MM^T\right] \\ S_{12} &= 2\left[I + MM^T\right]^{-1} M \\ S_{21} &= M^T\left[I - S_{11}\right] \\ S_{22} &= I - M^T S_{12} \end{aligned} \tag{2.20}$$

and

$$M = diag\left(\sqrt{Y_{p,q}^{hI,eII}}\right)\begin{bmatrix} J^{hI-hII} & 0 \\ J^{eI-hII} & J^{eI-eII} \end{bmatrix} diag\left(\sqrt{Z_{r,s}^{hI,eII}}\right) \tag{2.21}$$

In (2.20) and (2.21), I is the unit matrix, 'T' means transposed, and 'diag' denotes a diagonal matrix. The elements of the coupling matrix in (2.21) are

$$\begin{aligned} J_{pr}^{hI-hII} &= \iint_{S^{II}} \left(\nabla T_p^{hI}\right)\cdot\left(\nabla T_r^{hII}\right) ds \\ J_{qr}^{eI-hII} &= \iint_{S^{II}} \left(\nabla T_q^{eI}\right)\cdot\left(\nabla T_r^{hII} \times \hat{u}_z\right) ds \\ J_{qs}^{eI-eII} &= \iint_{S^{II}} \left(\nabla T_q^{eI}\right)\cdot\left(\nabla T_s^{eII}\right) ds \end{aligned} \tag{2.22}$$

Once the modal scattering matrix of a single discontinuity is determined, waveguide structures can be analyzed by cascading waveguide sections and modal scattering matrices of subsequent discontinuities. The combination of multiple scattering matrices is done by the generalized scattering matrix cascading algorithm, which will be given in Section 3.3.

2.4 Conclusions

The mode matching technique presents an accurate and complete full-wave solution of waveguide structures involving discontinuities. Through the incorporation of higher-order mode excitations and interactions, the theoretical treatment of irregular waveguides, such as T-septum waveguides, using mode matching forms a powerful numerical tool for the design of waveguide components. The fundamental concepts, such as (a) the

waveguide fields are derived from the superposition of the standard electric and magnetic vector potentials, (b) the so-obtained field expansions are matched in the plane of discontinuity in order to derive the generalized scattering matrix, and (c) the matrices of other discontinuities can be cascaded to analyze passive structures and components, will be extended in Chapter 3.

Chapter 3 FUNDAMENTAL FORMULATIONS

3.1 Introduction

In the preceding section, the mode-matching technique is presented as a numerical method for matching the electric and magnetic field components at a discontinuity deriving the generalized scattering matrix, combining and cascading discontinuities. This is a reliable and numerically stable technique, since exponents with only negative arguments appear in the numerical characterization of structures or components. However, there are a few drawbacks due to the nature of the formulation and its complexity to determine the eigenmode characteristics of nonstandard waveguide cross sections. This traditional algorithm also lacks the flexibility to handle a large variety of irregular waveguide cross sections. The other disadvantage is that the mode-matching technique encounters numerical difficulties when searching for the zeros of the determinant. The following sub-sections discuss these issues in more details.

3.1.1 Singular Value Problem

As shown in Chapter 2, the mode spectrum of the T-septum waveguide can be solved using the mode-matching technique. Let us now assume that the original T-septum structure depicted in Fig. 3.1a is changed to a cross section where the horizontal bar is narrower than the ridge it is attached to. The resulting cross section is that of Fig. 3.1b. Upon comparison with the analysis presented in Section 2.2, it is found that the boundary conditions in Fig. 3.1.b are different from those in Fig. 3.1a and, hence, a completely new analysis routine will have to be developed to consider such a case. (Note that it is often required to vary cross-sectional dimensions in an optimization routine so that the analysis of both configurations (Fig. 3.1a and Fig. 3.1b) might be required within the same optimization run.) Therefore, the introduction of an irregular (nonstandard) waveguide cross section necessitates that also its many dimensional variations be solved theoretically and programmed separately.

Another problem is encountered if the division into subregions is changed such as shown in Fig. 3.1c for the T-septum waveguide and Fig. 3.1d for its dimensional variation. Theoretically, such a change in subregions should not alter the results as long as enough terms are considered in the respective series expansions of (2.5) and (2.6). However, even modern computers cannot handle the fact that the respective matrices become ill conditioned [35] which essentially limits the number of terms available in the analysis (cf. second paragraph on p.28). With a smaller number of terms in the series expansions, the results obtained for a horizontal rather than a vertical subdivision of the cross section are notably different. This has been demonstrated in [55]. Thus using the subregions of Fig. 3.1c instead of those of Fig. 3.1a or, alternatively, using Fig. 3.1d instead of Fig. 3.1b, will lead to slightly different results for an entire waveguide component containing such cross sections. It is therefore advisable to develop a method, which refrains from dividing the cross section into subregions.

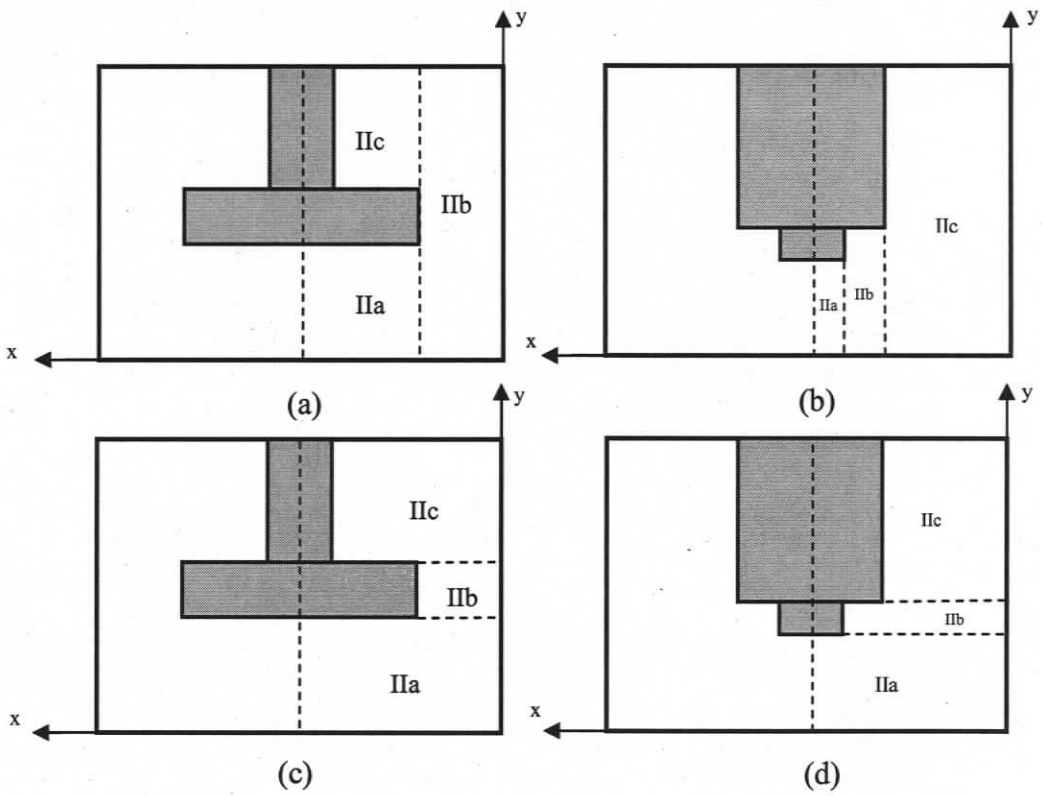

Fig. 3.1 Cross sections of T-septum waveguides with different subregions.

Two other disadvantages of the transverse analysis in the mode-matching technique become apparent when implementing such an algorithm. First, the search algorithms for either the zeros of the system determinant or the smallest singular value become increasingly complex if two cutoff frequencies in the mode spectrum are located very close together or are even identical within the smallest frequency variation acceptable in the search. This leads to extremely high CPU times because every new frequency in (2.7) will require the entire matrix to be recomputed and solved for its determinant or singular values. The only alternative towards a faster solution is to limit the frequency resolution. This, however, leads to a situation where legitimate solutions in the mode spectrum may remain undetected; then the field expansions in the irregular waveguide are missing individual components whose effect on the entire numerical accuracy is unknown.

Secondly, the coupling matrix in (2.21) has to be computed after all mode-spectrum information has been found during the search. In this context, note that the separation constants k_x in (2.7) become purely imaginary for increasing series terms r, s and t. In the field expansions (2.5), (2.6), in the system matrices (2.9), (2.10), in the subregion coefficients (2.12) and in the coupling matrix (2.21), (2.22), this leads to hyperbolic sine and cosine functions, which have to be truncated or evaluated in the limit in order to remain within the valid numerical range of floating point precision.

It is apparent that the mode-matching technique as introduced in Chapter 2 is not an ideal tool to determine the mode spectra of irregular waveguides. The main problem results from the fact that the solutions of the system matrix reside within that same matrix via separation constants k_x in (2.7). This is a direct consequence of subdividing the cross section and applying the related boundary conditions and continuities of field components at the subregion boundaries. The only alternative is to reformulate the task as a classical eigenvalue problem.

3.1.2 Eigenvalue Problem

In order to obtain a classical eigenvalue problem, we have to select a set of expansion functions, which do not depend on the actual size and location of ridges. Such set of

functions can be polygons as in the finite-element method [3], [16] or polynomials as used in [50], [51]. Within the framework of modal matching techniques, and in order to utilize the availability of existing mode-matching algorithms, it is advisable to select expansion functions, which compare well with the modes of common empty waveguides. In such a case, the computation of the inner products of empty-waveguide modes and those of the irregular waveguides can be performed straightforwardly and without a heavy burden on computer resources.

Therefore, in this thesis, we will use the well-known mode spectra of the empty waveguide housing as expansion functions for the individual modes of irregular waveguides. It will be demonstrated in the following sections that such an approach has several advantages compared to the transverse analysis using traditional mode-matching techniques. These advantages are:

1. The number of ridges and their locations within the waveguide housing are arbitrary. An example of four ridges is shown in Fig. 3.2.
2. A division into subregions is not required.
3. The formulation results in a classical eigenvalue problem with real and symmetric matrices for whose solutions a large variety of routines are available.
4. All inner product calculations can be performed over the surface areas of the ridges so that integration over the actual cross section of the waveguide becomes unnecessary.
5. The power normalizations of the irregular waveguide modes follow from the eigenvalue solutions and need not be recomputed.
6. Two submatrices of the coupling matrix in (2.21), (2.22) also follow from the eigenvalue solutions. Only TM-to-TE-mode coupling must be recomputed. And this is accomplished without the use of hyperbolic functions.

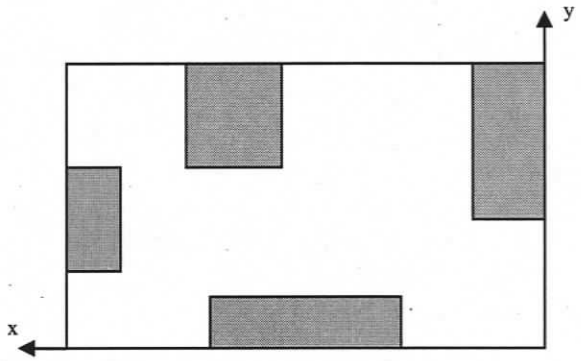

Fig. 3.2 Cross section of a waveguide with four arbitrarily located ridges.

The only extra effort, when using this method, consists in satisfying the boundary conditions for the TM modes in the irregular waveguide. As will be shown in the next section, this problem is easily solved by introducing a new function, which forces the E_z components of the TM modes to be zero over the cross sections of the ridges.

3.2 Transverse Eigenvalue Analysis

Consider a rectangular waveguide in Cartesian coordinates. The waveguide cross-section is assumed to be in the *x-y* plane, and it is uniform in the direction of propagation, the *z* axis, with corresponding propagation constant β. Let the longitudinal electric and magnetic field dependence be expressed as $e^{jk_z z}$, and $\{h_z\}$, $\{e_z\}$ be the complete sets of axial electric and magnetic fields which characterize the *TE* and *TM* modes, respectively, of the waveguide.

$$E_z = \sum_i c_i e_{zi}$$

$$H_z = \sum_j c_j h_{zj} \tag{3.1}$$

When the time variation $e^{j\omega t}$ is suppressed, the wave equation can be written as:

$$\nabla_T^2 \begin{bmatrix} E_Z \\ H_Z \end{bmatrix} + k_c^2 \begin{bmatrix} E_Z \\ H_Z \end{bmatrix} = 0 \tag{3.2}$$

where k_c^2 is the cutoff wavenumber, and ∇_T denotes the two-dimensional Laplacian operator in the *x-y* transverse plane. The *TE* waves must satisfy the Neumann boundary

condition and the *TM* waves follow the Dirichlet boundary condition. This can be written as

$$\frac{\partial H_z}{\partial \vec{n}}\Big|_D = 0 \qquad (3.3)$$
$$E_z\big|_D = 0$$

where D is the boundary of the waveguide and $\vec{n}$ represents the normal direction to the boundary. The two sets of axial electric and magnetic fields $\{h_z\}$, $\{e_z\}$ must satisfy the orthogonality relationship

$$\int_S h_{zm} h_{zn} dS = P_{nh}\delta_{nm} \qquad (3.4)$$
$$\int_S e_{zm} e_{zn} dS = P_{ne}\delta_{nm}$$

where P_{ne}, P_{nh} are power normalized factors, S is the waveguide's cross-section area, and δ_{nm} is the Kronecker delta function. Once the complete set of functions is solved, the transverse electric and magnetic fields can be found as [8]

$$\nabla_t \times \vec{e} = -j\omega\mu_0 H_z \vec{u}_z$$
$$\nabla_t \times \vec{h} = j\omega\varepsilon_0 E_z \vec{u}_z \qquad (3.5)$$
$$\nabla_t H_z + j\beta\vec{h} = j\omega\varepsilon_0(\vec{u}_z \times \vec{e})$$
$$\nabla_t E_z + j\beta\vec{e} = -j\omega\mu_0(\vec{u}_z \times \vec{h})$$

One way to determine the sets of axial fields is to employ the method of moments and Galerkin's procedure to express the electromagnetic energy as a function of an unknown longitudinal field *T(x,y)*. According to the moment method formulation [56], the axial *E/H* fields can be expanded in terms of suitable basis functions. In this approach, when each mode in the cross section of a waveguide is expressed as a sum of empty waveguide functions, the longitudinal field *T(x,y)* is written as

$$T(x,y) = \sum_{i=1}^{m} c_i \phi_i \qquad (3.6)$$

where c_i are the unknown coefficients to be determined, and ϕ_i are the functions which satisfy the boundary condition over the empty waveguide enclosure. Consequently, the electromagnetic energy function is written as

$$W(T) = \frac{1}{2}\iint_S \left[\left(\frac{\partial T}{\partial x}\right)^2 + \left(\frac{\partial T}{\partial y}\right)^2 \right] dxdy - \frac{k_c^2}{2}\iint_S T^2 dxdy \tag{3.7}$$

$$W(T) = \frac{1}{2}\iint_S [C]^T \left[\left(\frac{\partial \phi}{\partial x}\right)\left(\frac{\partial \phi}{\partial x}\right)^T + \left(\frac{\partial \phi}{\partial y}\right)\left(\frac{\partial \phi}{\partial y}\right)^T \right] [C] dxdy - \frac{k_c^2}{2}\iint_S [C]^T [\phi][\phi]^T [C] dxdy$$

$[C] = [C_1, C_2, \ldots, C_m]^T$ and $[\phi] = [\phi_1, \phi_2, \ldots, \phi_m]^T$ are column matrices. Taking the derivation of the energy function and forcing it to zero (minimizing the energy function) leads to the following matrix equation system [8], [9]

$$[K][C] = k_c^2 [M][C] \tag{3.8}$$

where the entries of the matrices $[K]$ and $[M]$ are in the form of

$$\begin{aligned} k_{i,j} &= \iint_S \left(\frac{\partial \phi_i}{\partial x}\frac{\partial \phi_j}{\partial x} + \frac{\partial \phi_i}{\partial y}\frac{\partial \phi_j}{\partial y} \right) dxdy \\ m_{i,j} &= \iint_S \phi_i \phi_j dxdy \end{aligned} \tag{3.9}$$

It is apparent that matrix equation (3.8) represents a standard generalized eigenvalue problem. In particular, eigenvalues k_c correspond to the square of the modal transverse eigenvalues (cutoff wavenumbers), while eigenvectors $[C]$ denote the coefficients of the transverse field components along the cross section of the waveguide corresponding to each mode. Treating k_c as a varying parameter and solving the matrix problem for k_c and $[C]$, one obtains cutoff frequencies and field distributions for the modes of a waveguide of interest. Once the eigenvalue matrix problem is solved, the cutoff wavenumbers can be back substituted into the matrix equation. Both the unknown coefficients and field components are easily calculated and depicted. Consequently, a complete mode distribution of the waveguide can be obtained theoretically.

Since the field components can be expressed as expansions in terms of hollow waveguide sets, which are defined everywhere over the cross section, they satisfy the boundary conditions of the enclosure but not necessarily those of the irregular waveguides. The

longitudinal components of the electric field are continuous close to the contour and vanish on the contour, where the transverse magnetic field must vanish too. On the other hand, both the longitudinal components of the magnetic field and the transverse components of the electrical field have step discontinuities in the cross section of the irregular waveguides, and they do not vanish. Therefore, we can define the field components as

$$T(x,y)_h = \sum_{i=1}^{m} c_i h_{zi}(x,y) \tag{3.10}$$

for a *TE* wave, where the boundary condition is $\left.\frac{\partial h_{zi}}{\partial \vec{n}}\right|_D = 0$, and

$$T(x,y)_e = \sum_{i=1}^{n} c_i e_{zi}(x,y) \tag{3.11}$$

for a *TM* wave, where the boundary condition is $e_{zi}\big|_D = 0$.

It is clear that the proper choice of the basis functions is an important procedure in the method of moments. If sharp-edge cross-section waveguides are involved, the elimination of the singularity at these corners becomes a challenge. Omar and Schünemann's [47] construction for the basis functions include edge-condition terms to model field singularities. Lin, Li, Yeo and Leong [51] use polynomial expansions as the proposed basis function. It results in large ill conditioned matrix equations, leading to less efficiency than the general method of moments procedure. In this study, sine and cosine functions with respect to rectangular waveguide analysis are chosen as basis functions due to their features of the spatial period of the waveform and relatively fast convergence. Based on the same approach, the ridged circular waveguide using Bessel functions as approximate trial functions is also investigated. A more detailed discussion of circular ridged waveguides will be presented in Chapter 5.

3.3 Modeling of Single-Ridged Waveguide Discontinuity

In order to confirm the correctness and applicability of this method, a single ridged cross section structure is analyzed. The example is set up for prospective use in formulating the basic building block discontinuity for various waveguide design algorithms. The theory is

then verified by comparison with the standard mode-matching technique, HFSS or with previously published results. Since field components are expressed in terms of pure sine and cosine functions combined with constraint functions for different cross sections, very good agreement is exhibited in most rectangular waveguide cases. It is demonstrated that the proposed method has the accuracy and efficiency compared to other methods in dealing with non-standard waveguides problems. The complete results of multiple ridged rectangular and circular waveguides are discussed later in Chapter 4 and Chapter 5, respectively.

3.3.1 Characteristics of Single Ridged Waveguide

Fig. 3.3 shows the cross section of a single ridged waveguide. It has been widely used in microwave components and systems, such as in broadband filters, orthomode transducers and antenna feed systems. The cutoff wave numbers of different modes in the ridged waveguide are computed using the proposed method.

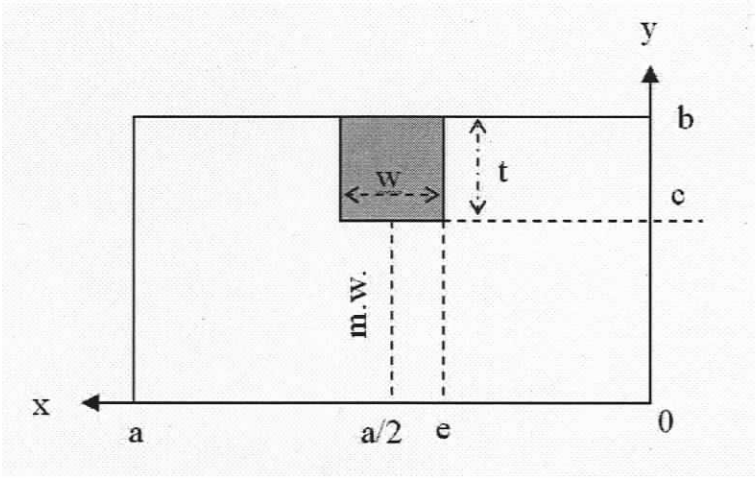

Fig. 3.3 Cross-sectional dimensions of single ridged waveguide.

TE Modes

The longitudinal *TE* field components, h_z, of the rectangular waveguide with perfectly conducting walls can be written as

$$h_{zi}(x,y)=\frac{\cos(k_{xm}x)}{\sqrt{1+\delta_{om}}}\frac{\cos(k_{yn}y)}{\sqrt{1+\delta_{on}}} \tag{3.12}$$

$$h_{zj}(x,y)=\frac{\cos(k_{xl}x)}{\sqrt{1+\delta_{ol}}}\frac{\cos(k_{yk}y)}{\sqrt{1+\delta_{ok}}}$$

where $k_{xm}=\frac{m\pi}{a}, k_{yn}=\frac{n\pi}{b}$ and $k_{xl}=\frac{l\pi}{a}, k_{yk}=\frac{k\pi}{b}$. δ is the Kronecker delta function, and i, j, m, n, l, k are integers. Since the axial components of the magnetic field do not necessarily vanish on the contour of the ridge or within the ridge, (3.12) represents a longitudinal set of functions to approximate the axial magnetic field of the ridge waveguide. Then the entries of matrix equation

$$[K][C]=k_c^2[M][C] \tag{3.13}$$

are written as

$$\begin{aligned} k_{i,j} &= \iint_S \left(\frac{\partial h_{zi}}{\partial x}\frac{\partial h_{zj}}{\partial x}+\frac{\partial h_{zi}}{\partial y}\frac{\partial h_{zj}}{\partial y}\right)dxdy \\ m_{i,j} &= \iint_S h_{zi}h_{zj}dxdy \end{aligned} \tag{3.14}$$

The computation can be simplified by substituting the integral over S with that of the empty waveguide and subtracting the integral over the ridges. Assuming that integers m, n are assigned to term i, and l, k are assigned to term j, then the detailed expression becomes as follows

$$\begin{aligned} k_{ij} =[k_{xi}^2+k_{yi}^2]\frac{ab}{4}-k_{xi}k_{xj}&\left\{\int_e^{e+w}\sin(k_{xi}x)\sin(k_{xj}x)dx\int_c^b\frac{\cos(k_{yi}y)}{\sqrt{1+\delta_{0n}}}\frac{\cos(k_{yj}y)}{\sqrt{1+\delta_{0k}}}dy\right\} \\ -k_{yi}k_{yj}&\left\{\int_e^{e+w}\frac{\cos(k_{xi}x)}{\sqrt{1+\delta_{0m}}}\frac{\cos(k_{xj}x)}{\sqrt{1+\delta_{0l}}}dx\int_c^b\sin(k_{yi}y)\sin(k_{yj}y)dy\right\} \end{aligned} \tag{3.15a}$$

$$m_{ij}=\frac{ab}{4}-\int_e^{e+w}\frac{\cos(k_{xi}x)}{\sqrt{1+\delta_{0m}}}\frac{\cos(k_{xj}x)}{\sqrt{1+\delta_{0l}}}dx\int_c^b\frac{\cos(k_{yi}y)}{\sqrt{1+\delta_{0n}}}\frac{\cos(k_{yj}y)}{\sqrt{1+\delta_{0k}}}dy \tag{3.15b}$$

TM Modes

Similar to the *TE* mode analysis, the longitudinal field components e_z of the *TM* modes in a rectangular waveguide can be written as

$$\begin{aligned} e_{zi}(x,y)&=\sin(k_{xm}x)\sin(k_{yn}y) \\ e_{zj}(x,y)&=\sin(k_{xl}x)\sin(k_{yk}y) \end{aligned} \tag{3.16}$$

where k_{xm}, k_{yn}, k_{xl}, k_{yk}, m, n, l, k, i, j hold same meaning as in the *TE* case. However, the boundary condition that $e_z|_D = 0$ on the contour and surface of the ridge must be enforced. Therefore, we define a special constraint function that forces the ridge to satisfy the required boundary condition. Let this constraint function $\Omega(x,y)$ be defined as

$$\Omega\left(\frac{x-x_0}{\Delta x},\frac{y-y_0}{\Delta y}\right)=\begin{cases}0, & x_0 \le x \le x_0+\Delta x \text{ and } y_0 \le y \le y_0+\Delta y\\ 1, & \text{elsewhere}\end{cases} \tag{3.17}$$

After rewriting the field component expressions, e_{zi}, e_{zj} become

$$\begin{aligned} e_{zi}(x,y)&=\Omega\left(\frac{x-e}{w},\frac{y-c}{t}\right)\sin(k_{xm}x)\sin(k_{yn}y)\\ e_{zj}(x,y)&=\Omega\left(\frac{x-e}{w},\frac{y-c}{t}\right)\sin(k_{xl}x)\sin(k_{yk}y)\end{aligned} \tag{3.18}$$

For the matrix equation $[K][C]=k_c^2[M][C]$, the elements in $[M]$ are

$$\begin{aligned} m_{i,j} &= \iint_S e_{zi}e_{zj}\,dxdy\\ &= \frac{ab}{4}-\int_e^{e+w}\sin(k_{xi}x)\sin(k_{xj}x)dx\int_c^b\sin(k_{yi}y)\sin(k_{yj}y)dy\end{aligned} \tag{3.19}$$

The entries in $[K]$ need some mathematical manipulation. The derivatives of $e_z(x,y)$ lead to delta functions for which the sampling theorem is applied:

$$\int_{-\infty}^{\infty}\delta(x-x_0)f(x)dx=f(x_0) \tag{3.20}$$

Thus

$$\begin{aligned} k_{i,j} &= \iint_S\left(\frac{\partial e_{zi}}{\partial x}\frac{\partial e_{zj}}{\partial x}+\frac{\partial e_{zi}}{\partial y}\frac{\partial e_{zj}}{\partial y}\right)dxdy\\ &= \iint_S\left\{\left[\left(\frac{\partial\Omega}{\partial x}\right)\sin(k_{xi}x)\sin(k_{yi}y)+k_{xi}\cos(k_{xi}x)\sin(k_{yi}y)\right]\left[\left(\frac{\partial\Omega}{\partial x}\right)\sin(k_{xj}x)\sin(k_{yj}y)+k_{xj}\cos(k_{xj}x)\sin(k_{yj}y)\right]\right.\\ &\quad\left.+\left[\left(\frac{\partial\Omega}{\partial y}\right)\sin(k_{xi}x)\sin(k_{yi}y)+k_{yi}\sin(k_{yi}x)\cos(k_{yi}y)\right]\left[\left(\frac{\partial\Omega}{\partial y}\right)\sin(k_{xj}x)\sin(k_{yj}y)+k_{yj}\sin(k_{yj}x)\cos(k_{yj}y)\right]\right\}dxdy\end{aligned} \tag{3.21a}$$

$$
\begin{aligned}
k_{i,j} = {} & k_{xi}k_{xj}\iint_S \left[\cos(k_{xi}x)\cos(k_{xj}x)\sin(k_{yi}y)\sin(k_{yj}y)\right]dxdy \\
& + k_{yi}k_{yj}\iint_S \left[\sin(k_{xi}x)\sin(k_{xj}x)\cos(k_{yi}y)\cos(k_{yj}y)\right]dxdy \\
& + \Big\{\sin(k_{xi}e)\sin(k_{xj}e) + \sin(k_{xi}(e+w))\sin(k_{xj}(e+w)) \\
& \quad + k_{xj}\left(-\sin(k_{xi}e)\cos(k_{xj}e) + \sin(k_{xi}(e+w))\cos(k_{xj}(e+w))\right) \\
& \quad + k_{xi}\left(-\cos(k_{xi}e)\sin(k_{xj}e) + \cos(k_{xi}(e+w))\sin(k_{xj}(e+w))\right)\Big\} \\
& \qquad \int_c^b \sin(k_{yi}y)\sin(k_{yj}y)dy \\
& + \Big\{\sin(k_{yi}c)\sin(k_{yj}c) + \sin(k_{yi}b)\sin(k_{yj}b) \\
& \quad + k_{yj}\left(-\sin(k_{yi}c)\cos(k_{yj}c) + \sin(k_{yi}b)\cos(k_{yj}b)\right) \\
& \quad + k_{yi}\left(-\cos(k_{yi}c)\sin(k_{yj}c) + \cos(k_{yi}b)\sin(k_{yj}b)\right)\Big\} \\
& \qquad \int_e^{e+w} \sin(k_{xi}x)\sin(k_{xj}x)dx \\
= {} & \left[k_{xi}^2 + k_{yi}^2\right]\frac{ab}{4} - k_{xi}k_{xj}\int_e^{e+w}\cos(k_{xi}x)\cos(k_{xj}x)dx\int_c^b \sin(k_{yi}y)\sin(k_{yj}y)dy \\
& \qquad - k_{yi}k_{yj}\int_e^{e+w}\sin(k_{xi}x)\sin(k_{xj}x)dx\int_c^b \cos(k_{yi}y)\cos(k_{yj}y)dy \\
& - \Big\{\sin(k_{xi}e)\sin(k_{xj}e) + \sin(k_{xi}(e+w))\sin(k_{xj}(e+w)) \\
& \quad + k_{xj}\left(-\sin(k_{xi}e)\cos(k_{xj}e) + \sin(k_{xi}(e+w))\cos(k_{xj}(e+w))\right) \\
& \quad + k_{xi}\left(-\cos(k_{xi}e)\sin(k_{xj}e) + \cos(k_{xi}(e+w))\sin(k_{xj}(e+w))\right)\Big\} \\
& \qquad \int_c^b \sin(k_{yi}y)\sin(k_{yj}y)dy \\
& - \Big\{\sin(k_{yi}c)\sin(k_{yj}c) + \sin(k_{yi}b)\sin(k_{yj}b) \\
& \quad + k_{yj}\left(-\sin(k_{yi}c)\cos(k_{yj}c) + \sin(k_{yi}b)\cos(k_{yj}b)\right) \\
& \quad + k_{yi}\left(-\cos(k_{yi}c)\sin(k_{yj}c) + \cos(k_{yi}b)\sin(k_{yj}b)\right)\Big\} \\
& \qquad \int_e^{e+w} \sin(k_{xi}x)\sin(k_{xj}x)dx
\end{aligned}
\tag{3.21b}
$$

Based on the above formulation, the cutoff frequencies for both *TE* and *TM* modes in the single ridged waveguide (a=19.05mm, b=9.5250mm, w=0.9mm, c=5.3625mm) have been computed and compared with the results from the simulation software HFSS. Very

good agreement is observed for both fundamental and higher-order modes as shown in Table 3.1 and Table 3.2.

TE mode	HFSS [GHz]	This method [GHz]	Difference [GHz]
TE(1)	5.77285	5.77205	+0.00080
TE(2)	16.70546	16.68992	+0.01554
TE(3)	23.39411	23.34991	+0.04420
TE(4)	27.86508	27.79041	+0.07467
TE(5)	32.18672	32.07066	+0.11606
TE(6)	38.59963	38.91791	-0.31828
TE(7)	39.12663	40.14490	-1.01827
TE(8)	46.94210	46.72370	+0.21840
TE(9)	47.86536	47.48739	+0.37797
TE(10)	50.23119	49.87987	+0.35132

Table 3.1 Cutoff frequencies of TE modes in single ridged waveguide.

TM mode	HFSS [GHz]	This method [GHz]	Difference [GHz]
TM(1)	25.84913	25.85423	-0.00510
TM(2)	33.00922	32.85336	+0.15586
TM(3)	39.16782	38.95492	+0.21290
TM(4)	46.40113	46.13283	+0.26830
TM(5)	52.06671	51.62487	+0.44184
TM(6)	53.88586	53.33155	+0.55431
TM(7)	61.29735	60.40758	+0.88977
TM(8)	62.18429	61.31525	+0.86904
TM(9)	66.58203	65.61001	+0.97202
TM(10)	67.93441	66.88086	+1.05355

Table 3.2 Cutoff frequencies of TM modes in single ridged waveguide.

The proposed analysis introduced here will serve as a fundamental tool to be developed into a general numerical algorithm. More examples of irregular ridged waveguides with rectangular enclosure are investigated in Chapter 4.

3.3.2 Characteristics of Single Ridged Waveguide

The eigenvalue analysis of ridged waveguides was discussed in the previous sections. However, this is only the first step in the design of ridged waveguide components. For a rigorous design, it is essential to evaluate the S-parameters of every discontinuity based on the interaction of the fundamental and higher order modes. An E-plane ridged waveguide discontinuity is used as an example to verify the formulations and computer codes.

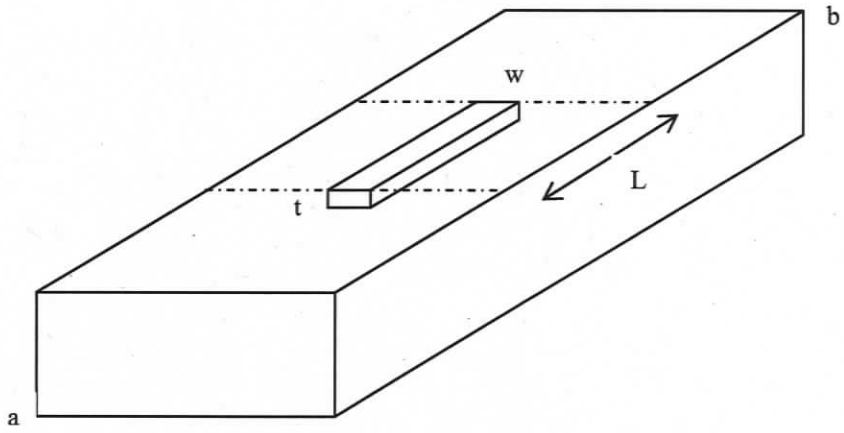

Fig. 3.4 Geometry of rectangular-to-ridge waveguide junctions with L=20mm.

In this example, a discontinuity from a rectangular waveguide to a single ridged rectangular waveguide is analyzed. As shown in Fig. 3.4, the junction connects a standard WR75 rectangular waveguide on both sides to a ridged waveguide of length 20 mm. The metallic ridge is w = 6mm wide and has a height of t = 4.5 mm. For the rigorous analysis of waveguide components in the longitudinal direction, the MMT is used and combined with the current approach. The main procedures of the MMT can be found in [22]. The structure in Fig 3.4 is divided into two blocks: standard to ridged waveguide and the ridged to standard waveguide. In order to evaluate the characteristics of these junctions including the effect of higher order modes, the generalized scattering matrices of two

individual sections is evaluated first. Cascading the two single modal scattering matrices leads to the overall generalized S-matrix of the structure. All TE_{mn} and TM_{mn} modes as well as all mode coupling effects must be taken into account for the full-wave field analysis. As the evaluation of the coupling coefficients is the fundamental step in the MMT, a more detailed derivation will be shown below.

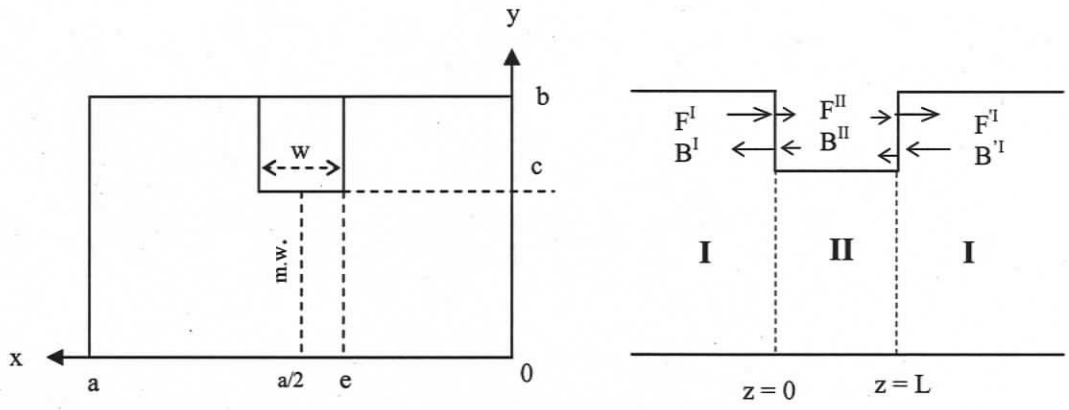

Fig. 3.5 Waveguide discontinuity of finite length L; coordinate system, discontinuity region and wave amplitudes.

The rectangular-to-ridged waveguide junctions are shown in Fig. 3.5. Waveguide I and II are joined in the $z = 0$ plane, and the length of the ridged part is L. The solution to the Helmholtz equation in Cartesian coordinates is written for both regions as a sum of incident and reflected waves with unknown amplitudes F and B. The vector potentials $\vec{A}_h$, $\vec{A}_e$ of TE and TM modes are then expressed as

$$\vec{A}_h = \sum_q \sqrt{Z_{hq}} T_{hq}(x,y)\left[F_{hq}e^{-jk_{zhq}} + B_{hq}e^{+jk_{zhq}}\right]\vec{u}_z \tag{3.22}$$

$$\vec{A}_e = \sum_p \sqrt{Y_{ep}} T_{ep}(x,y)\left[F_{ep}e^{-jk_{zep}} - B_{ep}e^{+jk_{zep}}\right]\vec{u}_z$$

where $Z_{hq} = \dfrac{\omega\mu}{k_{zhq}} = \dfrac{1}{Y_{hq}}$, $Y_{ep} = \dfrac{\omega\varepsilon}{k_{zep}} = \dfrac{1}{Z_{ep}}$ and $T_{hq}(x,y)$, $T_{ep}(x,y)$ are cross-sectional functions of the empty waveguide. The electric and magnetic fields of these TE and TM modes are

$$\vec{E}_h = \nabla\times(\vec{A}_h) = \sum_q \sqrt{Z_{hq}}(\nabla T_{hq}\times\vec{u}_{zq})\left[F_{hq}e^{-jk_{zhq}} + B_{hq}e^{+jk_{zhq}}\right]$$

$$\vec{H}_h = -\frac{1}{j\omega\mu}\nabla\times\nabla\times(\vec{A}_h) = -\sum_q \sqrt{Y_{hq}}(\nabla T_{hq})\left[F_{hq}e^{-jk_{zhq}} - B_{hq}e^{+jk_{zhq}}\right] \tag{3.23}$$

$$\vec{E}_e = \frac{1}{j\omega\varepsilon}\nabla\times\nabla\times(\vec{A}_e) = -\sum_p \sqrt{Z_{ep}}(\nabla T_{ep})\left[F_{ep}e^{-jk_{zep}} + B_{ep}e^{+jk_{zep}}\right]$$

$$\vec{H}_e = \nabla\times(\vec{A}_e) = \sum_p \sqrt{Y_{ep}}(\nabla T_{ep}\times\vec{u}_z)\left[F_{ep}e^{-jk_{zep}} - B_{ep}e^{+jk_{zep}}\right]$$

The transverse field components are sets of these individuals *TE/TM* modes. They are

$$\vec{E}_T = \vec{E}_{TE} + \vec{E}_{TM} = \nabla\times(\vec{A}_h) + \frac{1}{j\omega\varepsilon}\nabla\times\nabla\times(\vec{A}_e) \tag{3.24}$$

$$\vec{H}_T = \vec{H}_{TE} + \vec{H}_{TM} = -\frac{1}{j\omega\mu}\nabla\times\nabla\times(\vec{A}_h) + \nabla\times(\vec{A}_e)$$

Let *TE* and *TM* modes be arranged with increasing frequencies with indices q, p in waveguide I and r, s in waveguide II. At $z = 0$, the boundary conditions impose the continuity of the transverse $\vec{E}$ and $\vec{H}$ fields on the cross-section, and the transverse $\vec{E}$ field vanishes on the surface of the metal. That is

$$\begin{aligned}
&\vec{E}_T\big|_I = \vec{E}_T\big|_{II} && \text{on the cross section } S^{II}\\
&\vec{E}_T\big|_I = 0 && \text{on the cross section of the ridge } S^I - S^{II}\\
&\vec{H}_T\big|_I = \vec{H}_T\big|_{II} && \text{on the cross section } S^{II}
\end{aligned} \tag{3.25}$$

The vector expressions of this continuity feature

$$\begin{aligned}
&-\sum_q \sqrt{Z^I_{hq}}(\nabla T^I_{hq}\times\vec{u}_z)(F^I_{hq} + B^I_{hq}) - \sum_p \sqrt{Z^I_{ep}}(\nabla T^I_{ep})(F^I_{ep} + B^I_{ep})\\
&= \begin{cases} -\sum_i \sqrt{Z^{II}_{hi}}(\nabla T^{II}_{hi}\times\vec{u}_z)(F^{II}_{hi} + B^{II}_{hi}) - \sum_k \sqrt{Z^{II}_{ek}}(\nabla T^{II}_{ek})(F^{II}_{ek} + B^{II}_{ek}) & (x,y\in S^{II})\\ 0 & (x,y\in(S^I - S^{II})) \end{cases}
\end{aligned} \tag{3.26}$$

$$\begin{aligned}
&-\sum_q \sqrt{Y^I_{hq}}(\nabla T^I_{hq})(F^I_{hq} - B^I_{hq}) + \sum_p \sqrt{Y^I_{ep}}(\nabla T^I_{ep}\times\vec{u}_z)(F^I_{ep} - B^I_{ep})\\
&= -\sum_i \sqrt{Y^{II}_{hi}}(\nabla T^{II}_{hi})(F^{II}_{hi} - B^{II}_{hi}) + \sum_k \sqrt{Y^{II}_{ek}}(\nabla T^{II}_{ek}\times\vec{u}_z))(F^{II}_{ek} - B^{II}_{ek}) \quad (x,y\in S^{II})
\end{aligned} \tag{3.27}$$

We multiply (3.26) with $-(\nabla T_{hq}^{I} \times \vec{u}_z)$ and (∇T_{ep}^{I}), and integrate over the region S^I; we also multiply (3.27) by $-(\nabla T_{hi}^{II})$ and $(\nabla T_{ek}^{II} \times \vec{u}_z)$, and integrate over the area S^{II}. Upon the normalization of each individual mode in regions *I*, and *II* [30], [57]

$$P_{hi}^{I,II} = \sqrt{Z_{hi}^{\nu}}\sqrt{Y_{hi}^{\nu}}^{*}\left(k_{chi}^{I,II}\right)^2 \iint_{S^{II}} \left(T_{hi}^{I,II}(x,y)\right)^2 dxdy = 1 \text{ W}$$

$$\text{where } \sqrt{Z_{hi}^{I,II}}\sqrt{Y_{hi}^{I,II}}^{*} = \begin{cases} 1, & k_{zi}^2 > 0 \\ +\text{j}, & k_{zi}^2 < 0 \end{cases} \tag{3.28a}$$

$$P_{ei}^{I,II} = \sqrt{Z_{ei}^{I,II}}\sqrt{Y_{ei}^{I,II}}^{*}\left(k_{cei}^{I,II}\right)^2 \iint_{S^{II}} \left(T_{ei}^{I,II}(x,y)\right)^2 dxdy = 1 \text{ W}$$

$$\text{where } \sqrt{Z_{ei}^{I,II}}\sqrt{Y_{ei}^{I,II}}^{*} = \begin{cases} 1, & k_{zi}^2 > 0 \\ -\text{j}, & k_{zi}^2 < 0 \end{cases} \tag{3.28b}$$

The following relations are obtained ($\nu \in \{I, II\}$)

$$\iint_{S^{\nu}} (\nabla T_{hr}^{\nu} \times \vec{u}_z)(\nabla T_{hs}^{\nu} \times \vec{u}_z) ds = \iint_{S^{\nu}} (\nabla T_{hr}^{\nu})(\nabla T_{hs}^{\nu}) ds = \delta_{rs} \tag{3.29}$$

$$\iint_{S^{\nu}} (\nabla T_{er}^{\nu})(\nabla T_{es}^{\nu}) ds = \iint_{S^{\nu}} (\nabla T_{er}^{\nu} \times \vec{u}_z)(\nabla T_{es}^{\nu} \times \vec{u}_z) ds = \delta_{rs} \tag{3.30}$$

$$\iint_{S^{\nu}} (\nabla T_{hr}^{\nu} \times \vec{u}_z)(\nabla T_{es}^{\nu}) ds = \iint_{S^{\nu}} (\nabla T_{er}^{\nu} \times \vec{u}_z)(\nabla T_{hs}^{\nu}) ds \equiv 0 \tag{3.31}$$

The coupling integrals of these transverse electric and magnetic field components are for the $\bar{E}_T$ case

$$\iint_{S^{II}} (\nabla T_{hq}^{I} \times \vec{u}_z)(\nabla T_{hi}^{II} \times \vec{u}_z) ds = \iint_{S^{II}} (\nabla T_{hq}^{I})(\nabla T_{hi}^{II}) ds = (J_{hh})_{qi} \tag{3.32}$$

$$\begin{aligned} \iint_{S^{II}} (\nabla T_{hq}^{I} \times \vec{u}_z)(\nabla T_{ek}^{II}) ds &= -\iint_{S^{II}} (\vec{u}_z \times \nabla T_{hq}^{I})(\nabla T_{ek}^{II}) ds \\ &= -\iint_{S^{II}} (\nabla T_{ek}^{II}) \times (\vec{u}_z \times (\vec{u}_z \times (\nabla T_{hq}^{I}))) \vec{u}_z ds \\ &= \iint_{S^{II}} (\nabla T_{ek}^{II}) \times (\nabla T_{hq}^{I}) \vec{u}_z ds \\ &= \iint_{S^{II}} \left[\nabla \times (T_{ek}^{II} \nabla T_{hq}^{I}) - T_{ek}^{II} \nabla \times (\nabla T_{hq}^{I})\right] \vec{u}_z ds \\ &= -\int_{C} T_{ek}^{II} \frac{\partial T_{hq}^{I}}{\partial n} dl \equiv 0 \end{aligned} \tag{3.33}$$

$$(J_{he})_{qk} = 0 \tag{3.34}$$

$$\iint_{S^{II}} (\nabla T_{ep}^{I})(\nabla T_{hi}^{II} \times \vec{u}_z) ds = (J_{eh})_{pi} \tag{3.35}$$

$$\iint_{S^{II}} (\nabla T_{ep}^{I})(\nabla T_{ek}^{II}) ds = (J_{ee})_{pk} \tag{3.36}$$

and for the $\bar{H}_T$ case

$$\iint_{S^{II}} (-\nabla T_{hi}^{II})(-\nabla T_{hq}^{I}) ds = (J_{hh})_{iq} \tag{3.37}$$

$$\iint_{S^{II}} (\nabla T_{ek}^{II} \times \vec{u}_z)(-\nabla T_{hq}^{I}) ds = -\iint_{S^{II}} (-\nabla T_{hq}^{I} \times \vec{u}_z)(\nabla T_{ek}^{II}) ds \equiv 0 \tag{3.38}$$

$$\iint_{S^{II}} (-\nabla T_{hi}^{II})(\nabla T_{ep}^{I} \times \vec{u}_z) ds = -\iint_{S^{II}} (-\nabla T_{hi}^{II} \times \vec{u}_z)(\nabla T_{ep}^{I}) ds = (J_{eh})_{ip} \tag{3.39}$$

$$\iint_{S^{II}} (\nabla T_{ek}^{II} \times \vec{u}_z)(\nabla T_{ep}^{I} \times \vec{u}_z) ds = \iint_{S^{II}} (\nabla T_{ek}^{II})(\nabla T_{ep}^{I}) ds = (J_{ee})_{kp} \tag{3.40}$$

These expressions can be rewritten in Cartesian coordinates as

$$(J_{hh})_{qi} = \iint_{S^{II}} (\nabla T_{hq}^{I})(\nabla T_{hi}^{II}) ds = \iint_{S^{II}} \left(\frac{\partial T_{hq}^{I}}{\partial x}\frac{\partial T_{hi}^{II}}{\partial x} + \frac{\partial T_{hq}^{I}}{\partial y}\frac{\partial T_{hi}^{II}}{\partial y}\right) dxdy \tag{3.41}$$

$$(J_{eh})_{pi} = \iint_{S^{II}} (\nabla T_{ep}^{I})(\nabla T_{hi}^{II} \times \vec{u}_z) ds = \iint_{S^{II}} \left(\frac{\partial T_{ep}^{I}}{\partial x}\frac{\partial T_{hi}^{II}}{\partial y} - \frac{\partial T_{ep}^{I}}{\partial y}\frac{\partial T_{hi}^{II}}{\partial x}\right) dxdy \tag{3.42}$$

$$(J_{ee})_{pk} = \iint_{S^{II}} (\nabla T_{ep}^{I})(\nabla T_{ek}^{II}) ds = \iint_{S^{II}} \left(\frac{\partial T_{ep}^{I}}{\partial x}\frac{\partial T_{ek}^{II}}{\partial x} + \frac{\partial T_{ep}^{I}}{\partial y}\frac{\partial T_{ek}^{II}}{\partial y}\right) dxdy \tag{3.43}$$

$$(J_{he})_{qk} \equiv 0 \tag{3.44}$$

The formulation of the scattering matrix of the system can be derived from (3.26), (3.27) using coupling integrals (3.41)-(3.44)

$$Diag\left\{\sqrt{Z_{hq}^{\mathrm{I}}}\right\}(F_h^{\mathrm{I}} + B_h^{\mathrm{I}}) = J_{hh} Diag\left\{\sqrt{Z_{hi}^{\mathrm{II}}}\right\}(F_h^{\mathrm{II}} + B_h^{\mathrm{II}})$$

$$Diag\left\{\sqrt{Z_{ep}^{\mathrm{I}}}\right\}(F_e^{\mathrm{I}} + B_e^{\mathrm{I}}) = J_{eh} Diag\left\{\sqrt{Z_{hi}^{\mathrm{II}}}\right\}(F_h^{\mathrm{II}} + B_h^{\mathrm{II}}) + J_{ee} Diag\left\{\sqrt{Z_{ek}^{\mathrm{II}}}\right\}(F_e^{\mathrm{II}} + B_e^{\mathrm{II}})$$

$$J_{hh}^{T} Diag\left\{\sqrt{Y_{hq}^{\mathrm{I}}}\right\}(F_h^{\mathrm{I}} - B_h^{\mathrm{I}}) + J_{eh}^{T} Diag\left\{\sqrt{Y_{ep}^{\mathrm{I}}}\right\}(F_e^{\mathrm{I}} - B_e^{\mathrm{I}}) = Diag\left\{\sqrt{Y_{hi}^{\mathrm{II}}}\right\}(F_h^{\mathrm{II}} - B_h^{\mathrm{II}})$$

$$J_{ee}^{T} Diag\left\{\sqrt{Y_{hp}^{\mathrm{I}}}\right\}(F_e^{\mathrm{I}} - B_e^{\mathrm{I}}) = Diag\left\{\sqrt{Y_{ek}^{\mathrm{II}}}\right\}(F_e^{\mathrm{II}} - B_e^{\mathrm{II}}) \tag{3.45}$$

Combining *TE* and *TM* modes, we get

$$Diag\left\{\sqrt{Z^I}\right\}(F^I + B^I) = \begin{pmatrix} J_{hh} & 0 \\ J_{eh} & J_{ee} \end{pmatrix} Diag\left\{\sqrt{Z^{II}}\right\}(F^{II} + B^{II}) \tag{3.46}$$

$$\begin{pmatrix} J_{hh} & 0 \\ J_{eh} & J_{ee} \end{pmatrix}^T Diag\left\{\sqrt{Y^I}\right\}(F^I - B^I) = Diag\left\{\sqrt{Y^{II}}\right\}(F^{II} - B^{II}) \tag{3.47}$$

Upon defining matrix [*M*] as

$$M = \begin{bmatrix} Diag\left\{Y_h^{\mathrm{I}}\right\} J_{hh} Diag\left\{Z_h^{\mathrm{II}}\right\} & 0 \\ Diag\left\{Y_e^{\mathrm{I}}\right\} J_{eh} Diag\left\{Z_h^{\mathrm{II}}\right\} & Diag\left\{Y_e^{\mathrm{I}}\right\} J_{ee} Diag\left\{Z_e^{\mathrm{II}}\right\} \end{bmatrix} \tag{3.48}$$

(3.46), (3.47) are expressed as

$$F^I + B^I = M(F^{II} + B^{II}) \tag{3.48}$$

$$M^T(F^I - B^I) = F^{II} - B^{II} \tag{3.49}$$

The scattering matrix is defined as (Fig. 3.5)

$$\begin{bmatrix} B^I \\ F^{II} \end{bmatrix} = \begin{bmatrix} S_{11} & S_{21} \\ S_{12} & S_{22} \end{bmatrix} \cdot \begin{bmatrix} F^I \\ B^{II} \end{bmatrix} \tag{3.50}$$

From (3.48),

$$B^I = M(F^{II} + B^{II}) - F^I$$

Which is substituted into (3.49)

$$M^T(F^I - M(F^{II} + B^{II}) + F^I) = F^{II} - B^{II}$$

$$\left[E - M^T M\right] B^{II} + 2M^T F^I = \left[E + M^T M\right] F^{II} \tag{3.51}$$

Combining with (3.50), we find

$$\left[S_{21}\right] = 2\left[U + M^T M\right]^{-1} M^T \tag{3.52}$$

$$\left[S_{22}\right] = \left[U + M^T M\right]^{-1}\left[U - M^T M\right] \tag{3.53}$$

The other two submatrices are obtained from (3.51)-(3.53)

$$F^{II} = S_{21}F^I + S_{22}B^{II}$$

$$B^I = M(F^{II} + B^{II}) - F^I = M\left[S_{21}F^I + S_{22}B^{II} + B^{II}\right] - F^I$$

And using (3.50) again, we get

$$\left[S_{11}\right] = MS_{21} - U \tag{3.54}$$

$$[S_{12}] = M[S_{22} + U] \tag{3.55}$$

where U is the unit matrix.

The next procedure is to apply the generalized scattering matrix techniques to cascade or combine the modal scattering matrices of two or more discontinuities. This method incorporates all higher-order mode interactions between two discontinuities. The following Fig. 3.6, Fig. 3.7, and Fig. 3.8 describe the application of the method in cascading two-port discontinuities, cascading a discontinuity with a homogeneous waveguide, and combining a discontinuity with its inverse separated by a finite length of waveguide.

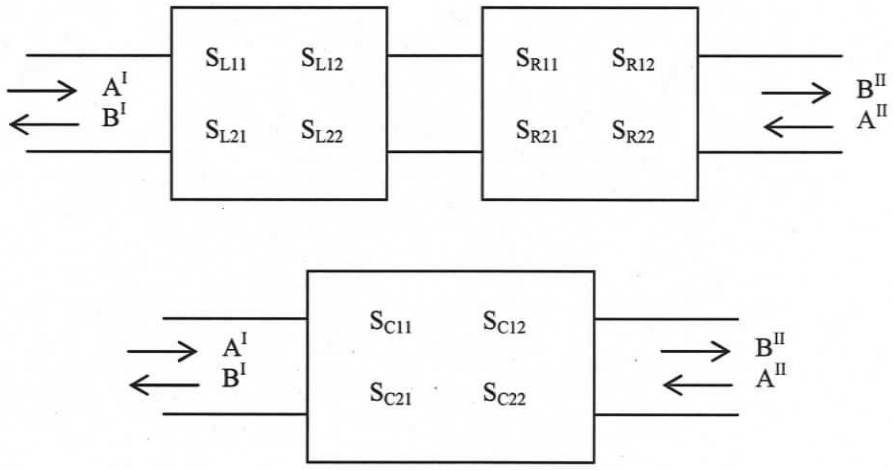

Fig. 3.6 Cascading two-port scattering matrices.

The overall scattering matrices are

$$\begin{aligned} S_{C11} &= S_{L11} + S_{L12} S_{R11} W S_{L21} \\ S_{C12} &= S_{L12} \left(I + S_{R11} W S_{L22} \right) S_{R12} \\ S_{C21} &= S_{R21} W S_{L21} \\ S_{C22} &= S_{R22} + S_{R21} W S_{L22} S_{R12} \end{aligned} \tag{3.56}$$

where $W = \left(I - S_{L22} S_{R11} \right)^{-1}$ and S_L and S_R are generalized scattering matrices as shown in Fig. 3.6.

For the case of a discontinuity followed by a homogeneous waveguide,

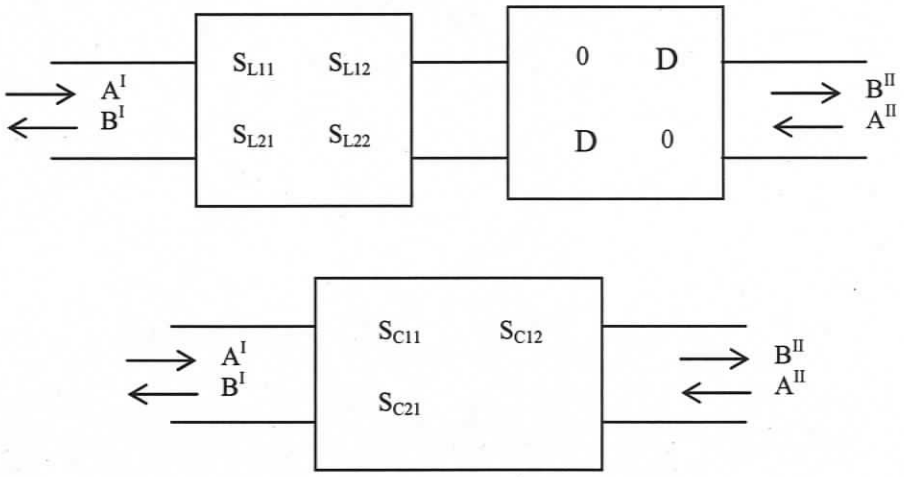

Fig. 3.7 Scattering matrix of a discontinuity followed by a homogeneous waveguide.

the complete scattering matrices are

$$\begin{aligned} S_{C11} &= S_{L11} \\ S_{C12} &= S_{L12}D \\ S_{C21} &= DS_{L21} \\ S_{C22} &= DS_{L22}D \end{aligned} \tag{3.57}$$

where $D = diag(e^{-jk_{zi}l})$ is the diagonal matrix containing the phase relations of the propagating and evanescent modes between the discontinuities at finite length L, and the propagation constants k_{zi} at a frequency f are obtained from

$$k_{zi} = \begin{cases} k_0\sqrt{1-\left(\dfrac{f_{ci}}{f}\right)^2} & \text{when } f > f_{ci} \\ -jk_0\sqrt{\left(\dfrac{f_{ci}}{f}\right)^2 - 1} & \text{when } f < f_{ci} \end{cases} \tag{3.58}$$

k_0 and f_{ci} are free-space wave number and cutoff frequency for the mode, respectively.

The combination of a two-port discontinuity with its inverse separated by a finite length of waveguide is shown in Fig. 3.8.

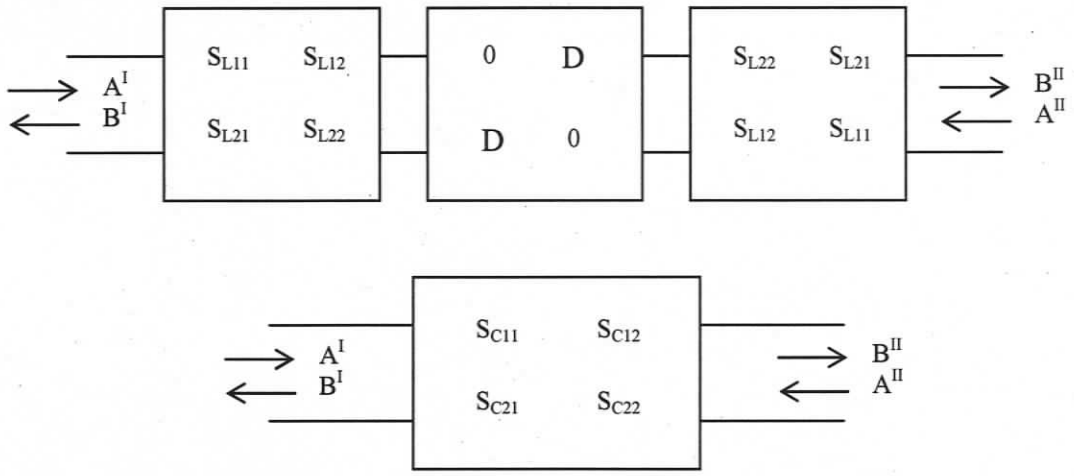

Fig. 3.8 Scattering matrix of a discontinuity and its inverse separated by a homogeneous waveguide.

The generalized scattering matrix of the combined structure is

$$
\begin{aligned}
S_{C11} &= S_{L22} + S_{L12} D \left[I - S_{L22} D S_{L22} D \right]^{-1} S_{L22} D S_{L21} \\
S_{C12} &= S_{L12} D \left[I - S_{L22} D S_{L22} D \right]^{-1} S_{L21} \\
S_{C21} &= S_{C12} \\
S_{C22} &= S_{C11}
\end{aligned}
\tag{3.59}
$$

where D is same as in (3.57) and (3.58).

After these fundamental formulations have been built up based on the eigenvalue mode spectrum approach and mode matching technique, the theoretical treatment of the ridged waveguide is applied to the structure in Fig. 3.4.

The cross-section eigenfunctions in both regions I and II (cf. Fig. 3.5) are

$$T_{hq}^{\mathrm{I}} = \frac{2}{\sqrt{ab\left[(2m-1)\frac{\pi}{a}\right]^2 + (\frac{n\pi}{b})^2}} \cos\left((2m-1)\frac{\pi}{a}x\right) \frac{\cos\left(\frac{n\pi}{b}y\right)}{\sqrt{1+\delta_{0n}}} \tag{3.60}$$

$$T_{ep}^{\mathrm{I}} = \frac{2}{\sqrt{ab\left[(2m-1)\frac{\pi}{a}\right]^2 + (\frac{n\pi}{b})^2}} \sin\left((2m-1)\frac{\pi}{a}x\right) \sin\left(\frac{n\pi}{b}y\right) \tag{3.61}$$

$$T_{hj}^{\mathrm{II}} = \sum_i c_{ij}^h h_{zi} = \sum_i c_{ij}^h \frac{\cos\left(\frac{l\pi}{a}x\right)}{\sqrt{1+\delta_{0l}}} \frac{\cos\left(\frac{k\pi}{b}y\right)}{\sqrt{1+\delta_{0k}}} \tag{3.62}$$

$$T_{ej}^{\mathrm{II}} = \sum_j c_{ij}^e e_{zj} = \sum_j c_{ij}^e \Omega(\frac{x-e}{w}, \frac{y-c}{t}) \sin\left(\frac{l\pi}{a}x\right) \sin\left(\frac{k\pi}{b}y\right) \tag{3.63}$$

To evaluate the coupling integrals, (3.60)-(3.63) are substituted into (3.41)-(3.43)

$$(J_{hh})_{q.r} = \iint_{S^{II}} (\frac{\partial T_{hq}^I}{\partial x} \frac{\partial T_{hr}^{II}}{\partial x} + \frac{\partial T_{hq}^I}{\partial y} \frac{\partial T_{hr}^{II}}{\partial y}) dxdy \tag{3.64}$$

$$(J_{eh})_{p.r} = \iint_{S^{II}} (\frac{\partial T_{ep}^I}{\partial x} \frac{\partial T_{hr}^{II}}{\partial y} - \frac{\partial T_{ep}^I}{\partial y} \frac{\partial T_{hr}^{II}}{\partial x}) dxdy \tag{3.65}$$

$$(J_{ee})_{p.s} = \iint_{S^{II}} (\frac{\partial T_{ep}^I}{\partial x} \frac{\partial T_{es}^{II}}{\partial x} + \frac{\partial T_{ep}^I}{\partial y} \frac{\partial T_{es}^{II}}{\partial y}) dxdy \tag{3.66}$$

$$(J_{he})_{q.s} = 0 \tag{3.67}$$

By comparing (3.64)-(3.67) with (3.15a), (3.15b), (3.19), (3.21b), it is clear that the coupling matrix elements $(J_{hh})_{q.r}$ and $(J_{ee})_{p.s}$ are already calculated during the derivation of the mode spectrum in the previous section. The eigenvector $[C_{ij}]$ is directly obtained from the standard eigenvalue matrix equation. Only $(J_{eh})_{p.r}$ must be calculated. It is obvious that all coupling integrals are frequency independent and integration is evaluated only once. Hence, the entire procedure is rigorous and yet computationally efficient.

Applying the proposed algorithm, the results of S parameters for the structure of Fig. 3.4 is shown in Fig. 3.9. Good agreement is achieved with results from the commercial

software package μWave Wizard. With the symmetry of a vertical magnetic wall, the CPU time for computing this structure is 34 seconds over 500 frequency points using this method, while it takes 123 seconds by the commercial software μWave Wizard on a 2.13 GHz Pentium notebook with 1.25 GB of RAM.

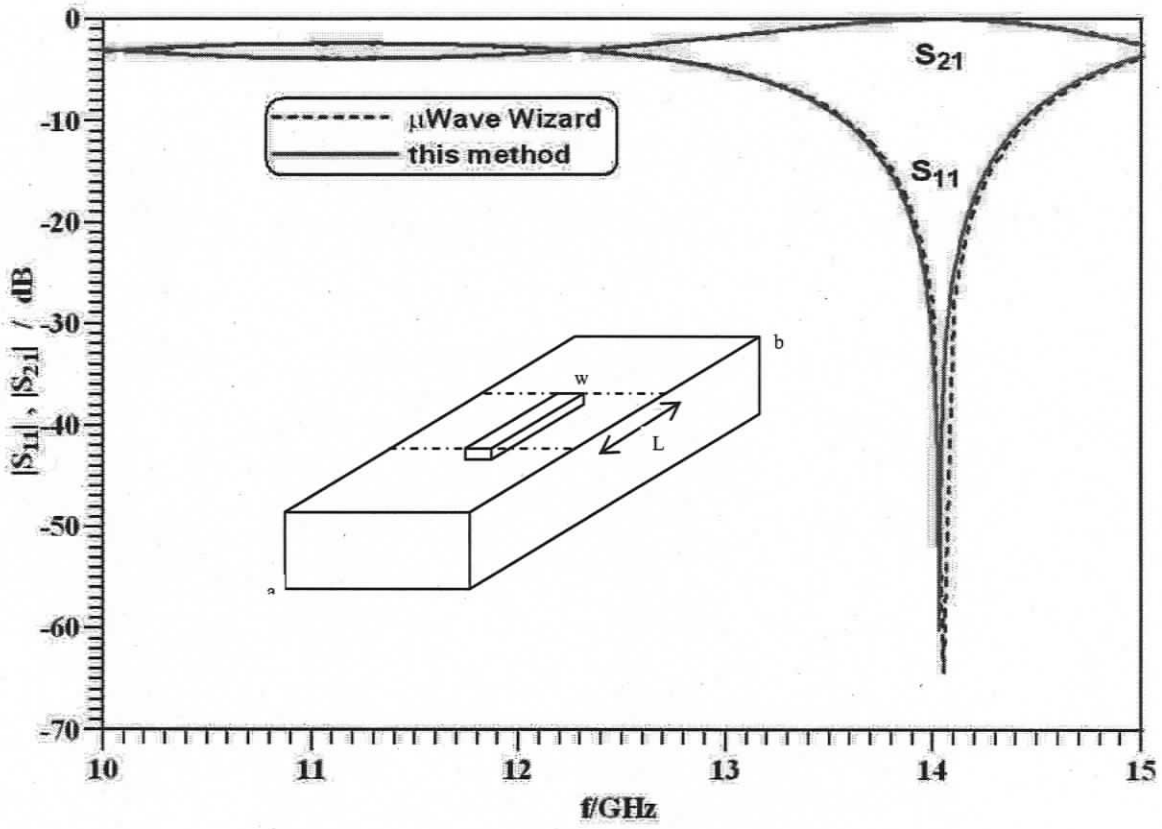

Fig. 3.9 Comparison of *S*-parameters from present approach with μWave Wizard.

3.4 Conclusion

A rigorous analysis of a single ridged rectangular waveguide has been performed in this Chapter. A classical eigenvalue spectrum approach is obtained and provides the complete characteristics of ridged cross-section waveguides. A mode-matching technique is then applied to the discontinuity from an empty rectangular waveguide to a single ridged waveguide including the interaction of fundamental and higher-order modes. The combination of the eigenvalue mode spectrum approach and the mode-matching technique has been established as a new numerical method based entirely on model

analysis. This method has the advantage of flexibility when dealing with the position of the ridge, and can be easily implemented in existing routings based on modal matching approaches. A simple model of standard-to-ridge-to-standard rectangular waveguide discontinuities has been set up to validate the algorithm. Accurate agreement is demonstrated by comparing our results with those of the μMwave Wizard and HFSS simulations.

Chapter 4 MULTI-RIDGED RECTANGULAR WAVEGUIDES

4.1 Introduction

In this chapter, the fundamental formulations presented in the previous chapters are expanded to include the theoretical and numerical analysis of nonstandard multi-ridged waveguide structures. The chapter proposes a general formulation for determining the propagation characteristics and generalized scattering matrix for such nonstandard multi-ridged waveguides. The keys to the development of accurate computer-aided component design are the precise calculations of the generalized scattering matrices for the discontinuities within the components and the ability to freely handle different structures without delay.

Within this chapter, a complete analysis for rectangular waveguides with multiple ridges provides full theoretical development of this eigenvalue mode-spectrum approach. Upon completion of the analytical treatment, two-dimensional analyses demonstrate the convergence of the proposed theory. The subsequent sections present rigorous designs for filters, transformers and other waveguide structures including validations by measurements and independent numerical codes.

4.2 Complete Analysis of Multi-Ridged Rectangular Waveguides

A rectangular waveguide with asymmetric multiple ridges is analyzed as a general approach to verify the developed algorithm. The basic formulation follows that of previous chapters straightforwardly. Fig. 4.1 depicts the cross section of an irregular ridged waveguide.

Within the Cartesian coordinates system, a general formulation of the mode spectrum is obtained from the eigenvalue approach of (3.2).

$$\nabla_T^2 \begin{Bmatrix} H_z \\ E_z \end{Bmatrix} + k_c^2 \begin{Bmatrix} H_z \\ E_z \end{Bmatrix} = 0 \tag{4.1}$$

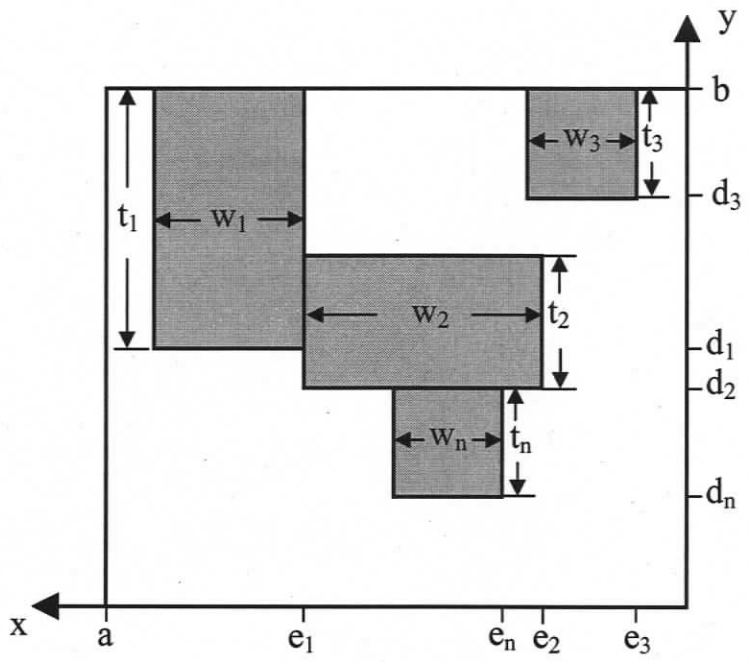

Fig. 4.1 Cross section of multiple ridges in rectangular waveguide.

By using the mode composition of the surrounding regular waveguide, the longitudinal field components are expressed as a complete set of rectangular waveguide functions which must satisfy the boundary conditions.

$$\begin{Bmatrix} H_Z \\ E_Z \end{Bmatrix} = \sum_{i=1}^{P} c_i \begin{Bmatrix} h_{zi} \\ e_{zi} \end{Bmatrix} \tag{4.2}$$

A generalized eigenvalue equation can be obtained by minimizing the system energy function and forcing it to zero [48]-[51].

$$[K][c] = k_c^2 [M][c] \tag{4.3}$$

The diagonal matrix k_c holds the eigenvalues of (4.3), which correspond to the cutoff frequencies of the structure. The eigenvector matrix $[c]$ holds the coefficients of the expansion functions. The entries of matrices K and M represent the inner products of the waveguide modes of the housing with the expansions in (4.2).

$$[K]_{ij} = \int_S \nabla_T \begin{Bmatrix} h_{zi} \\ e_{zi} \end{Bmatrix} \nabla_T \begin{Bmatrix} h_{zj} \\ e_{zj} \end{Bmatrix} ds \tag{4.4}$$

$$[M]_{ij} = \int_S \begin{Bmatrix} h_{zi} \\ e_{zi} \end{Bmatrix} \begin{Bmatrix} h_{zj} \\ e_{zj} \end{Bmatrix} ds \tag{4.5}$$

Here S represents the cross section of the multi-ridged waveguide. The surface integral over S can be performed such that

$$\int_S f(s)ds = \int_{\text{housing}} f(s)ds - \sum_{i=1}^{N} \int_{\text{ridge(i)}} f(s)ds \tag{4.6}$$

The first part of the right side is the integral over the rectangular waveguide housing, and the second one is the integral over the ridges. Substituting the direct integral over the cross section by the difference in (4.6) greatly enhances the flexibility of the method to handle multiple ridges with arbitrary positions in the waveguide housing. Note that the ridges are always rectangular; therefore, integration over the surface of the ridges, e.g. in Fig. 4.1, is easier, even if their positions change, than that over the more complex cross section of the actual multi-ridged waveguides. After the eigenvalues are solved, the cutoff wavenumbers can be back-substituted into the matrix equation. Both the eigenvectors and field components are easily calculated and finally determined by the power normalization for each corresponding eigenmode i.

$$P_i = \int_S (\vec{E}_i \times \vec{H}_i^*)\vec{u}_z ds = (k_{ci})^2 \int_S T_i^2 ds = 1 \text{ W} \tag{4.7}$$

To develop a complete mode spectrum solution for the multi-ridge waveguide structure, a proper choice of the basis functions is an important procedure in the eigenvalue approach. In this work, the eigenfunctions of the empty waveguide housing, or slight modifications thereof, are chosen as basis functions.

Following Fig. 4.1, the waveguide housing with dimensions of $a \times b$ contains N ridges. These individual ridges must either connect to the enclosure, or they must be linked to each other with at least one of them touching the housing. This assumption holds for most practical applications. The dimensions of ridges are defined as $w_n \times t_n$, and their locations within the housing are e_n, d_n.

4.2.1 TE Modes of Multi-Ridged Waveguide

In order to determine the TE modes of multi-ridged waveguides, the expansion functions, h_z, are chosen to be identical to the modes of the housing. This guarantees that the boundary conditions over the cross section of the multi-ridged waveguide are satisfied.

$$h_{zi}(x,y)=\frac{\cos(k_{xm}x)}{\sqrt{1+\delta_{0m}}}\frac{\cos(k_{yn}y)}{\sqrt{1+\delta_{on}}}$$
$$h_{zj}(x,y)=\frac{\cos(k_{xl}x)}{\sqrt{1+\delta_{0l}}}\frac{\cos(k_{yk}y)}{\sqrt{1+\delta_{0k}}} \tag{4.8}$$

In (4.8) $k_{xm}=\frac{m\pi}{a}, k_{yn}=\frac{n\pi}{b}$ and $k_{xl}=\frac{l\pi}{a}, k_{yk}=\frac{k\pi}{b}$. δ_{ij} is the Kronecker delta function, and $i\rightarrow(m,n)$, $j\rightarrow(l,k)$ are integers ordered with respect to increasing cutoff frequencies. Obviously, index n is used twice but is easily distinguished as representing either the separation constant k_{yn} in (4.8) or an individual ridge in Fig 4.1. Using (4.4) in Cartesian coordinates and (4.6), we get

$$\begin{aligned}[K_h]_{i,j}&=\int_S \nabla_T h_{zi}\nabla_T h_{zj}ds=\iint_S\left(\frac{\partial h_{zi}}{\partial x}\frac{\partial h_{zj}}{\partial x}+\frac{\partial h_{zi}}{\partial y}\frac{\partial h_{zj}}{\partial y}\right)dxdy\\&=[k_{xi}^2+k_{yi}^2]\frac{ab}{4}-k_{xi}k_{xj}\sum_{n=1}^{N}\left\{\int_{e_n}^{e_n+w_n}\sin(k_{xi}x)\sin(k_{xj}x)dx\int_{d_n}^{d_n+t_n}\frac{\cos(k_{yi}y)}{\sqrt{1+\delta_{0k_{yi}}}}\frac{\cos(k_{yj}y)}{\sqrt{1+\delta_{0k_{yj}}}}dy\right\}\\&\quad-k_{yi}k_{yj}\sum_{n=1}^{N}\left\{\int_{e_n}^{e_n+w_n}\frac{\cos(k_{xi}x)}{\sqrt{1+\delta_{0k_{xi}}}}\frac{\cos(k_{xj}x)}{\sqrt{1+\delta_{0k_{xj}}}}dx\int_{d_n}^{d_n+t_n}\sin(k_{yi}y)\sin(k_{yj}y)dy\right\}\end{aligned} \tag{4.9}$$

The entries of matrix M are obtained with (4.5) and (4.6)

$$\begin{aligned}[M_h]_{i,j}&=\int_S h_{zi}h_{zj}ds=\iint_S h_{zi}h_{zj}dxdy\\&=\frac{ab}{4}-\sum_{n=1}^{N}\int_{e_n}^{e_n+w_n}\frac{\cos(k_{xi}x)}{\sqrt{1+\delta_{0k_{xi}}}}\frac{\cos(k_{xj}x)}{\sqrt{1+\delta_{0k_{xj}}}}dx\int_{d_n}^{d_n+t_n}\frac{\cos(k_{yi}y)}{\sqrt{1+\delta_{0k_{yi}}}}\frac{\cos(k_{yj}y)}{\sqrt{1+\delta_{0k_{yj}}}}dy\end{aligned} \tag{4.10}$$

4.2.2 TM Modes of Multi-Ridged Waveguide

The longitudinal field components, e_z, of the TM modes in a rectangular waveguide can be written as

$$e_{zi}(x,y)=\sin(k_{xm}x)\sin(k_{yn}y)$$

$$e_{zj}(x,y) = \sin(k_{xl}x)\sin(k_{yk}y) \tag{4.11}$$

where k_{xm}, k_{yn}, k_{xl}, k_{yk}, m, n, l, k, i, j hold the same meaning as those in the TE case. However, the boundary condition that $e_z|_S = 0$ on the contour and surfaces of the ridges is not satisfied by these expansion functions. Therefore, the empty waveguide's TM mode basis functions must be modified so that they can fulfill the boundary conditions. We define a special constraint function that forces the expansion function (4.11) to satisfy the boundary conditions. Let this constraint function $\Omega(x,y)$ be defined as

$$\Omega\left(\frac{x-x_0}{\Delta x}, \frac{y-y_0}{\Delta y}\right) = \begin{cases} 0, & x_0 \le x \le x_0 + \Delta x \text{ and } y_0 \le y \le y_0 + \Delta y \\ 1, & \text{elsewhere} \end{cases} \tag{4.12}$$

After rewriting the field component expressions, e_{zi}, e_{zj} become

$$\begin{aligned} e_{zi}(x,y) &= \sin(k_{xm}x)\sin(k_{yn}y)\prod_{n=1}^{N}\Omega\left(\frac{x-e_n}{w_n}, \frac{y-d_n}{t_n}\right) \\ e_{zj}(x,y) &= \sin(k_{xl}x)\sin(k_{yk}y)\prod_{n=1}^{N}\Omega\left(\frac{x-e_n}{w_n}, \frac{y-d_n}{t_n}\right) \end{aligned} \tag{4.13}$$

For the matrix equation $[K][c] = k_c^2[M][c]$, the elements of M do not contain derivatives. Therefore, they are straightforwardly obtained as

$$\begin{aligned} [M_e]_{i,j} &= \iint_S e_{zi}e_{zj}\,dxdy \\ &= \frac{ab}{4} - \sum_{n=1}^{N}\left\{\int_{e_n}^{e_n+w_n}\sin(k_{xi}x)\sin(k_{xj}x)dx \int_{d_n}^{d_n+t_n}\sin(k_{yi}y)\sin(k_{yj}y)dy\right\} \end{aligned} \tag{4.14}$$

The entries of K need some mathematical manipulation since derivatives involve not only sine and cosine functions but also the constraint functions. The derivatives of $e_z(x,y)$ in (4.13) lead to delta functions in (4.4) for which the sifting theorem is applied

$$\int_{-\infty}^{\infty}\delta(x-x_0)f(x)dx = f(x_0) \tag{4.15}$$

Thus

$$
\begin{aligned}
\left[K_{e\delta}\right]_{i,j} &= \int_S \nabla_T e_{zi} \nabla_T e_{zj} ds \\
&= \iint_S \left(\frac{\partial e_{zi}}{\partial x}\frac{\partial e_{zj}}{\partial x} + \frac{\partial e_{zi}}{\partial y}\frac{\partial e_{zj}}{\partial y} \right) dxdy \\
&= \left[k_{xi}^2 + k_{yi}^2\right]\frac{ab}{4} + \left[K_{e\delta}\right]_{i,j} \\
&\quad - k_{xi}k_{xj}\sum_{n=1}^{N}\int_{e_n}^{e_n+w_n}\cos(k_{xi}x)\cos(k_{xj}x)dx\int_{t_n}^{d_n+t_n}\sin(k_{yi}y)\sin(k_{yj}y)dy \\
&\quad - k_{yi}k_{yj}\sum_{i=1}^{N}\int_{e_n}^{e_n+w_n}\sin(k_{xi}x)\sin(k_{xj}x)dx\int_{t_n}^{d_n+t_n}\cos(k_{yi}y)\cos(k_{yj}y)dy
\end{aligned}
\tag{4.16}
$$

The additional matrix $\left[K_{e\delta}\right]$ is related to applying the sifting theorem (4.15) in (4.4). It contains combinations of line integrals on the surface of the ridges in one direction multiplied by the terms from (4.15) in the respective other directions. These entries are

$$
\begin{aligned}
\left[K_{e\delta}\right]_{i,j} &= \sum_{n=1}^{N}\Big\{\sin(k_{xi}e_n)\sin(k_{xj}e_n) + \sin(k_{xi}(e_n+w_n))\sin(k_{xj}(e_n+w_n)) \\
&\quad + k_{xi}\left(-\cos(k_{xi}e_n)\sin(k_{xj}e_n) + \cos(k_{xi}(e_n+w_n))\sin(k_{xj}(e_n+w_n))\right) \\
&\quad + k_{xj}\left(-\sin(k_{xi}e_n)\cos(k_{xj}e_n) + \sin(k_{xi}(e_n+w_n))\cos(k_{xj}(e_n+w_n))\right)\Big\} \\
&\quad \bullet \int_{d_n}^{d_n+t_n}\sin(k_{yi}y)\sin(k_{yj}y)dy \\
&\quad + \sum_{n=1}^{N}\Big\{\sin(k_{yi}d_n)\sin(k_{yj}d_n) + \sin(k_{yi}(d_n+t_n))\sin(k_{yj}(d_n+t_n)) \\
&\quad + k_{yi}\left(-\cos(k_{yi}d_n)\sin(k_{yj}d_n) + \cos(k_{yi}(d_n+t_n))\sin(k_{yj}(d_n+t_n))\right) \\
&\quad + k_{yj}\left(-\sin(k_{yi}d_n)\cos(k_{yj}d_n) + \sin(k_{yi}(d_n+t_n))\cos(k_{yj}(d_n+t_n))\right)\Big\} \\
&\quad \bullet \int_{e_n}^{e_n+w_n}\sin(k_{xi}y)\sin(k_{xj}y)dx
\end{aligned}
\tag{4.17}
$$

Based on the above formulations, the systematic eigenvalue equation (4.3) can be solved completely for both TE and TM modes. The cutoff frequencies are first obtained to validate the proposed approach, and then to be tested for convergence. The eigenvectors c_i are generated from standard symmetric eigenvector matrix routines and normalized according to (4.7).

$$
P_i = k_{ci}^2 \sum_{p=1}^{P} M_{ip} c_{ip}^2 \tag{4.18}
$$

This completes the eigenvalue mode spectrum approach. The main advantage compared with standard modal techniques is that the number of ridges and their locations within the housing are arbitrary. This method also provides flexibility and easy implementation in existing routines based on mode-matching approaches in three-dimensional analysis.

Since MMT routines are based on mode coupling between the modes of the empty waveguide and those of the ridged waveguide, a frequency-independent coupling matrix of the form

$$J = \begin{bmatrix} J_{hh} & 0 \\ J_{eh} & J_{ee} \end{bmatrix} \tag{4.19}$$

must be set up (cf. Chapter 3). It is one of the advantages of using empty waveguide modes as expansion functions that submatrices J_{hh} and J_{ee} are directly obtained from (4.4) and eigenvector c.

$$\left(J_{hh}\right)_{q,i} = A_q \sum_{p=1}^{P_h} \left(K_h\right)_{ip} \left(c_h\right)_{ip} \tag{4.20}$$

$$\left(J_{ee}\right)_{q,j} = D_q \sum_{p=1}^{P_e} \left(K_e\right)_{jp} \left(c_e\right)_{jp} \tag{4.21}$$

Note that the number of expansion terms P used in (4.20) and (4.21) are different for TE(P_n) and TM(P_e) modes with eigenvector matrices c_h and c_e, respectively. A_q and D_q are the well-known power normalization terms of the empty waveguide housing. The K_e matrix in (4.21) also differs from that in (4.16) since matrix $K_{e\delta}$ is zero. This is due to the fact that the sum of the housing's TM modes forces the transverse electric field to vanish on the face of the ridges. The only matrix, which must be calculated, is the coupling submatrix J_{eh}. It relates the housing's TM modes (index e) to the multi-ridged waveguide's TE modes (index h) and is given by

$$(J_{eh})_{q,j} = \iint_{S^{II}} (\nabla T_{eq}^{I})(\nabla T_{hj}^{II}) ds = \iint_{S^{II}} (\frac{\partial T_{eq}^{I}}{\partial x}\frac{\partial T_{hj}^{II}}{\partial y} - \frac{\partial T_{eq}^{I}}{\partial y}\frac{\partial T_{hj}^{II}}{\partial x}) dxdy$$

$$= D_q \left\{ k_{x,eq} \sum_{p=1}^{P_h} k_{y,hp} (c_h)_{ip} \sum_{n=1}^{N} \int_{e_n}^{e_n+w_n} \cos(k_{x,eq}x) \frac{\cos(k_{x,hj}x)}{\sqrt{1+\delta_{0,k_{x,hj}}}} dx \int_{d_n}^{d_n+t_n} \sin(k_{y,eq}y) s\sin(k_{y,hj}y) dy \right.$$

$$\left. - k_{y,eq} \sum_{p=1}^{P_h} k_{x,hp} (c_h)_{ip} \sum_{n=1}^{N} \int_{e_n}^{e_n+w_n} \sin(k_{x,eq}x) s\sin(k_{x,hj}x) dx \int_{d_n}^{d_n+t_n} \cos(k_{y,eq}y) \frac{\cos(k_{y,hj}y)}{\sqrt{1+\delta_{0,k_{y,hj}}}} dy \right\} \quad (4.22)$$

From here on, standard MMT procedures are applied to obtain the overall modal scattering matrices of waveguide components involving multiple ridges. The complete formulations are as presented in Chapter 3.

4.3 Convergence Analysis of Multi-Ridged Waveguides

The most important property of a series expansion is its convergence. Therefore, the two-dimensional eigenvalue mode-spectrum approach is applied to two examples for which fundamental mode references are available in the literature. The first example is a rectangular waveguide with four symmetrically placed ridges, Fig. 4.2a; the second structure contains two L-shaped septa shown in Fig. 4.2b.

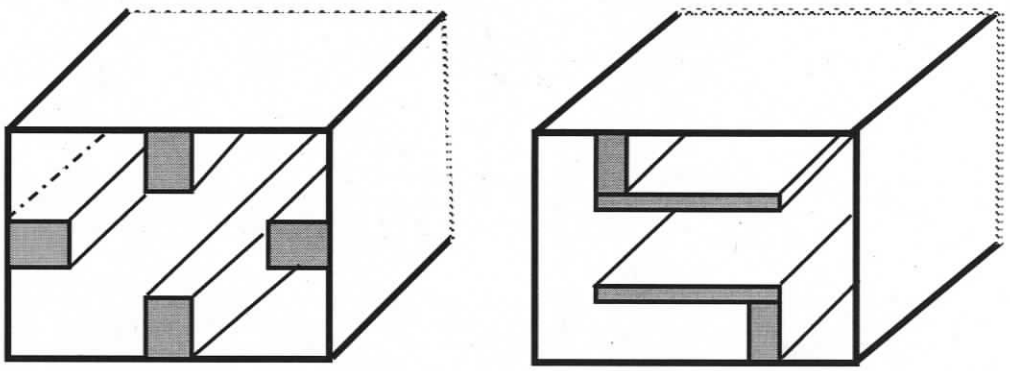

(a) (b)

Fig. 4.2 Rectangular waveguides loaded with (a) quadruple ridges and (b) double L-shaped septa.

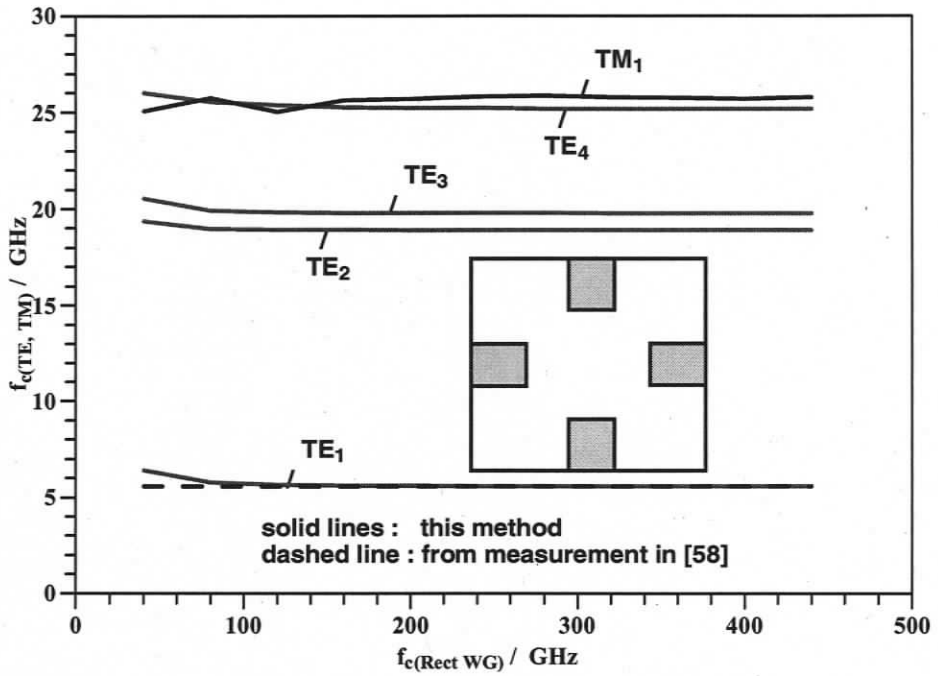

Fig. 4.3 Convergence analysis of quadruple-ridged rectangular waveguide in symmetric configuration and comparison with fundamental-mode solution (dashed line) in [58].

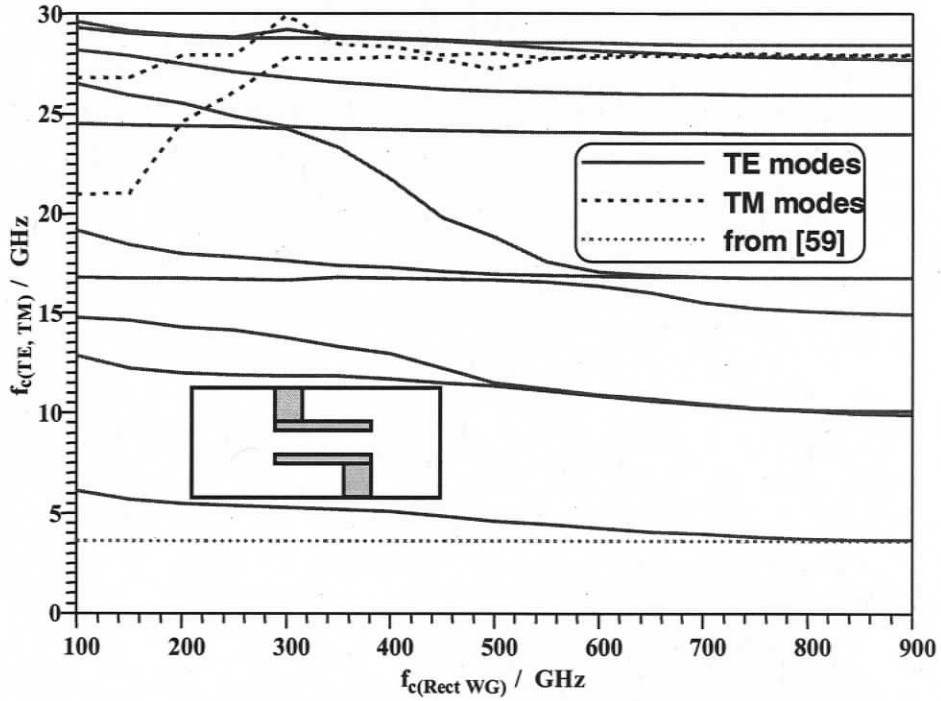

Fig. 4.4 Convergence analysis of quadruple-ridged rectangular waveguide in asymmetric configuration and comparison with fundamental-mode solution (dotted line) in [59].

Fig. 4.3 and Fig. 4.4 show the convergence analyses for quadruple-ridged and double-L shaped waveguides and comparisons with fundamental-mode measurements of [58] and fundamental-mode calculations of [59], respectively. The cutoff frequencies of the multi-ridged waveguides are displayed as a function of the highest cutoff frequency in the housing up to which all terms (m, n) in (4.8) and (l, k) in (4.13) are considered. Good convergence behavior is observed for all modes in both figures. Obviously, the two-plane symmetric structure in Fig. 4.3 requires fewer expansion terms since the symmetry also affects the number of symmetric terms in the expansion. The asymmetric cross section in Fig. 4.4 requires all asymmetric expansion terms and, therefore, their numbers are much higher. Of specific interest for later three-dimensional analysis is the fact that modes with almost identical cutoff frequencies, e.g. the 2nd, 3rd and 5th, 6th TE modes in Fig. 4.4, are accurately computed. Such cases have always caused problems in mode-search algorithms which require a system determinant to vanish, e.g. [30], [44].

Besides numerous advantages presented in the previous sections, one serious disadvantage of this method must be addressed. With increasing cross-sectional area occupied by the ridges within the housing's cross section and with an increasing number of expansion terms in (4.2), the symmetric matrices in (4.4) and (4.5) become ill-conditioned. As a result, matrix M is no longer positive definite, which can be immediately detected by an appropriate eigenvalue/vector-solving code. In such cases, an adaptive process must be used to find a reasonable compromise between accuracy and computational efficiency. For all practical applications and certainly for those presented in the next section, eigenmode solutions converge sufficiently well before this effect comes into play.

4.4 Components in Ridged Rectangular Waveguide Technology

This section presents computer-aided designs and analyses for waveguide discontinuities, cascaded ridged components, waveguide transformers, waveguide filters, and waveguide twist structures. All results are verified by measurements and/or other computational results. It is demonstrated that the proposed algorithm presents a viable option for multi-ridged rectangular waveguide component design.

4.4.1 Ridged Waveguide with Single and Cascaded Discontinuities

Using the eigenvalue mode-spectrum approach in conjunction with MMT as a computational "engine", the analysis of a variety of waveguide discontinuities is developed through the 'building block' approach; that is, the analyses of discontinuities are facilitated and then cascaded for eventual component designs by the generalized S-matrix method. The key to accurate design is the precise calculation of the generalized scattering matrices for all discontinuities within a component.

To validate the proposed approach, a double ridged waveguide structure is selected as an example for a two-port discontinuity (Fig. 4.5a). The dimensions of the empty waveguide are a=15.85 mm and b=7.625 mm; the ridge thickness is t =0.9 mm, and the gap between ridges is g=3.1 mm. The fundamental-mode scattering parameters are computed with this method and compared to all-MMT data as shown in Fig. 4.5b. Very good agreement is obtained.

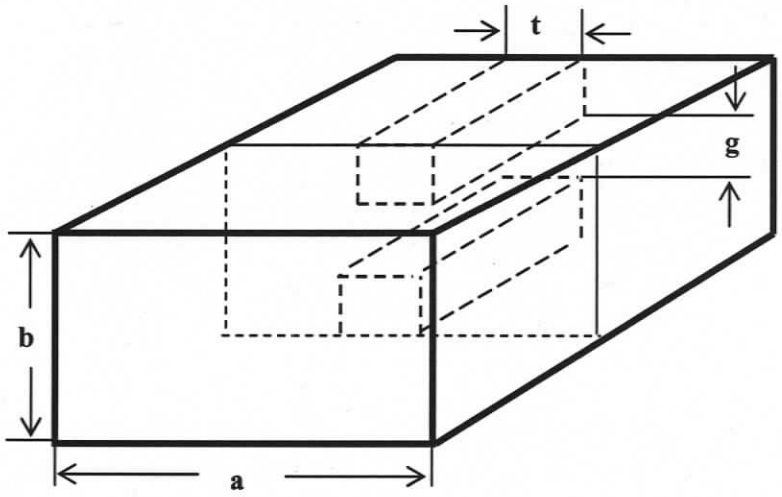

(a)

Fig. 4.5 Discontinuity rectangular waveguide to double-ridged waveguide; (a) three dimensional view, (b) S parameters.

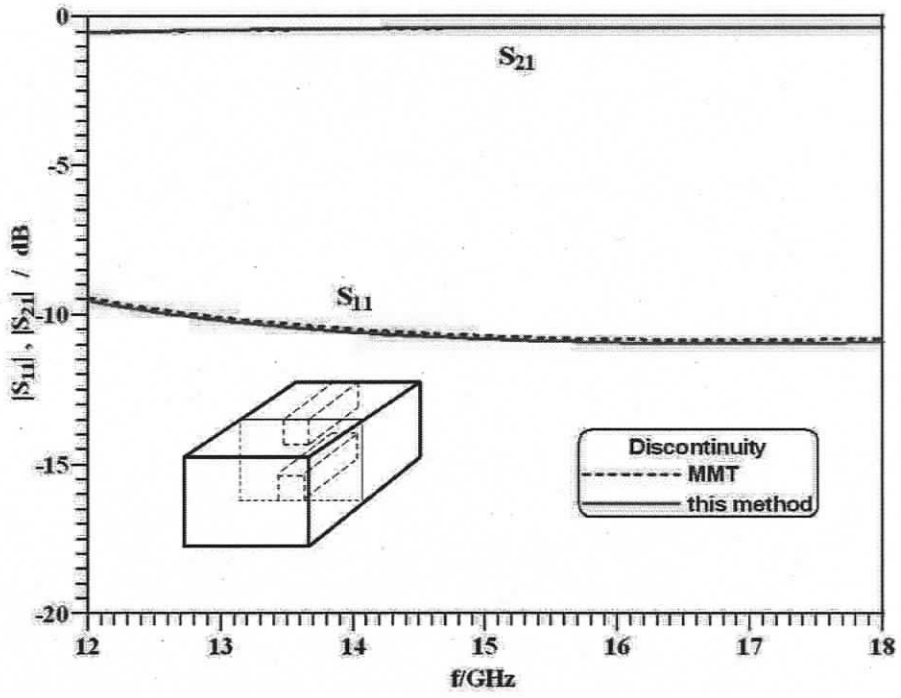

(b)

Fig. 4.5 Continued.

The second example is the core building block involving rectangular-to-ridged waveguide and ridged-to-rectangular waveguide discontinuities. The two scattering matrices of the discontinuities are combined using the generalized S-matrix method presented in Chapter 3. The structure in Fig. 4.6a contains 20 mm long empty waveguides on both sides, and a ridged waveguide of 2.6 mm length. All other parameters are identical to those of Fig. 4.5. The complete S-parameters generated with the mode-spectrum analysis exhibit results consistent with those from an all-MMT approach as shown in Fig. 4.6b. This accuracy together with the advantage of flexible ridge placement demonstrates the effectiveness of the proposed approach.

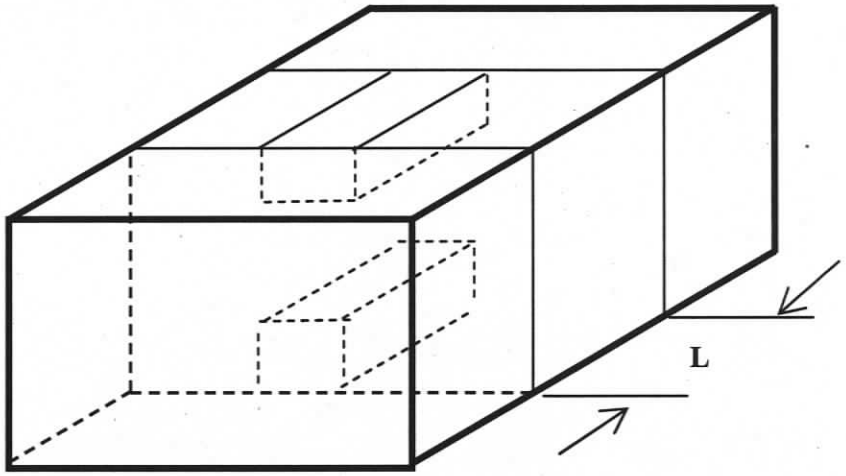

(a)

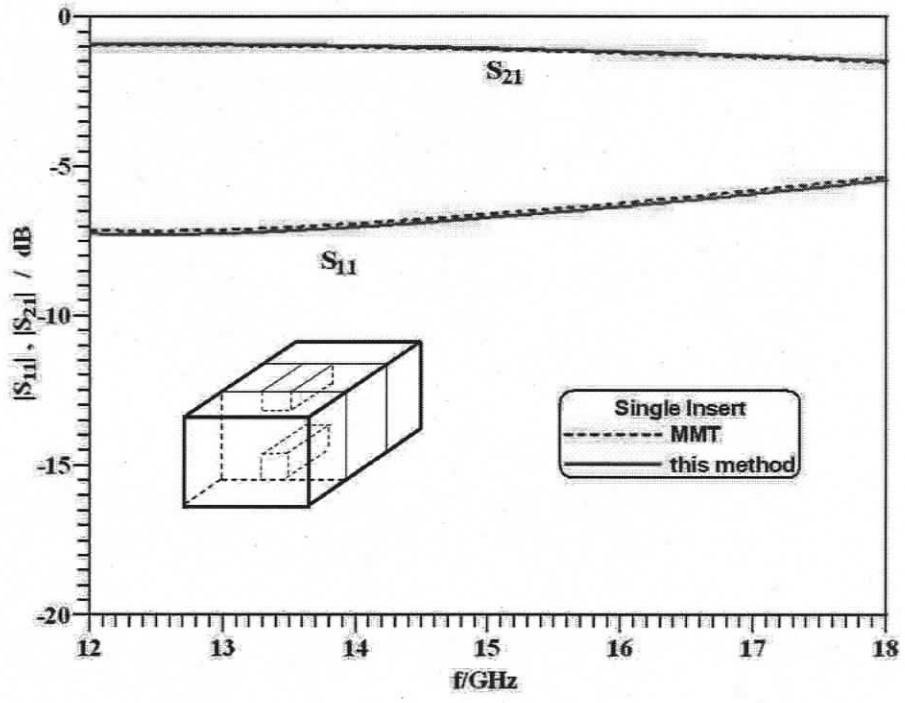

(b)

Fig. 4.6 Double-ridged section in rectangular waveguide; (a) three-dimensional view, (b) S parameters.

Cascaded ridged waveguide discontinuities can now be analyzed using above procedures. Such a configuration is shown in Fig. 4.7a with reciprocal waveguide length l_1 =20 mm, l_2 =2.6 mm, l_3 =10.25 mm, l_4 =8.95 mm, l_5 =10.5 mm. The empty and ridged waveguide dimensions are chosen as previously. The structure is decomposed into building block scattering matrices, which are repeatedly cascaded with those of the intermediate homogeneous waveguide sections. Fig. 4.7b shows the performance of the structure in the Ku-band frequency range of 12 GHz to 18 GHz. The calculated results are compared with those of the commercial tool μWave Wizard, MMT, and measured results. As can be seen from Fig. 4.7b, a very good accuracy has been achieved.

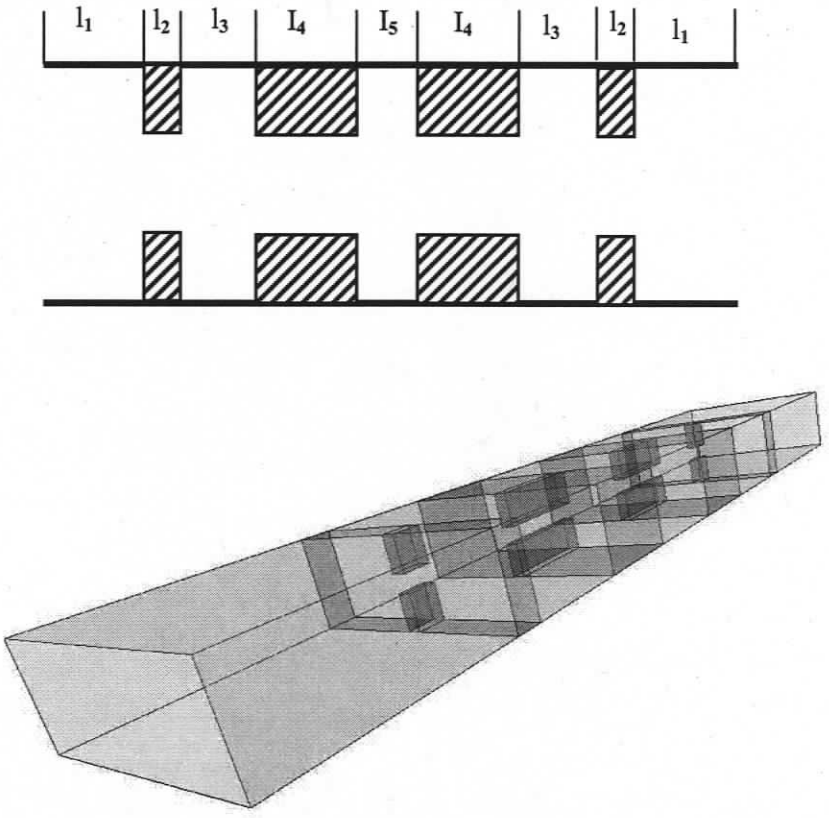

(a)

Fig. 4.7 Cascaded doubled-ridged waveguide discontinuities according to [30]; (a) top and three-dimensional view, (b) S parameter comparison.

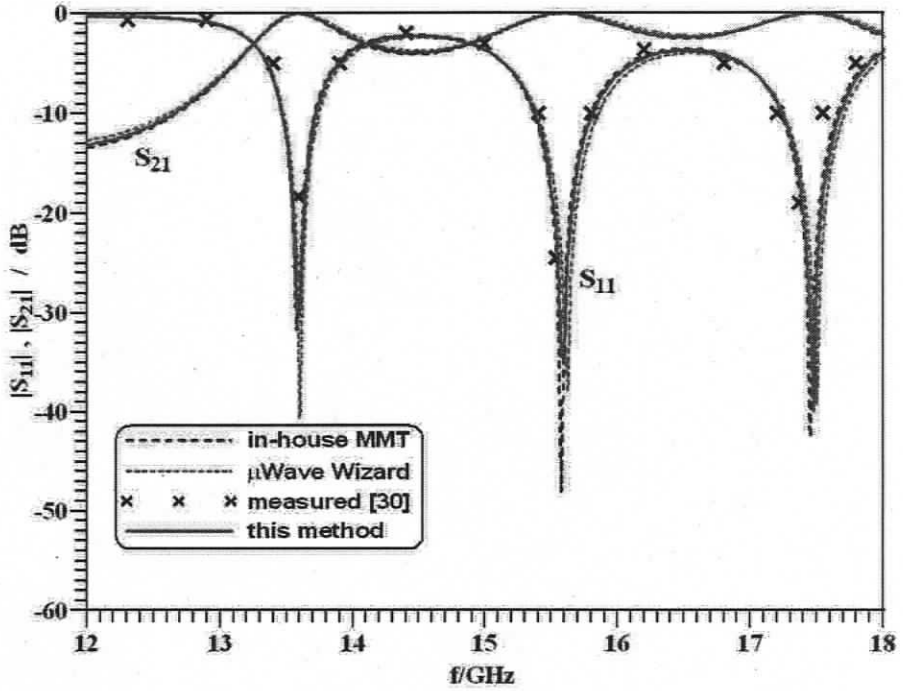

Fig. 4.7 Continued.

4.4.2 Stepped Ridged Waveguide Transformer

One application of ridged waveguides is the ridged waveguide transformer. This is due to its large bandwidth, low characteristic impedance, and compact design [57]. To verify the proposed approach in a real application, a back-to-back connected double-ridged waveguide transformer is presented in Fig. 4.8a. The input reflection coefficient in dB of the back-to-back waveguide transformer is shown in Fig. 4.8b. The computed results of the eigenvalue mode-spectrum approach (solid line) are in very good agreement with those of the MMT (dashed line) and measurements (crosses) presented in [57]. Note that the analysis of this component requires the computation of six different double-ridged waveguide mode spectra. Differences between the three results in Fig. 4.8b are small and well below -25 dB; therefore, they are acceptable in almost all practical applications.

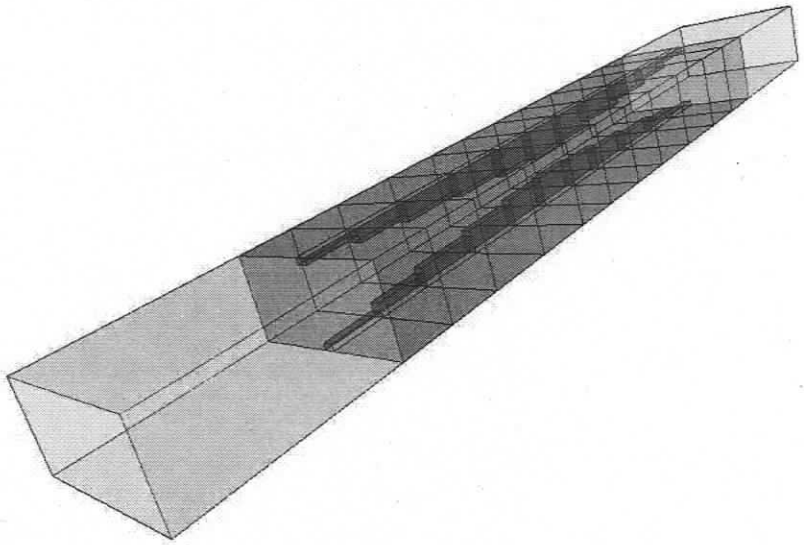

Fig. 4.8a Stepped back-to-back connected ridge waveguide transformer.

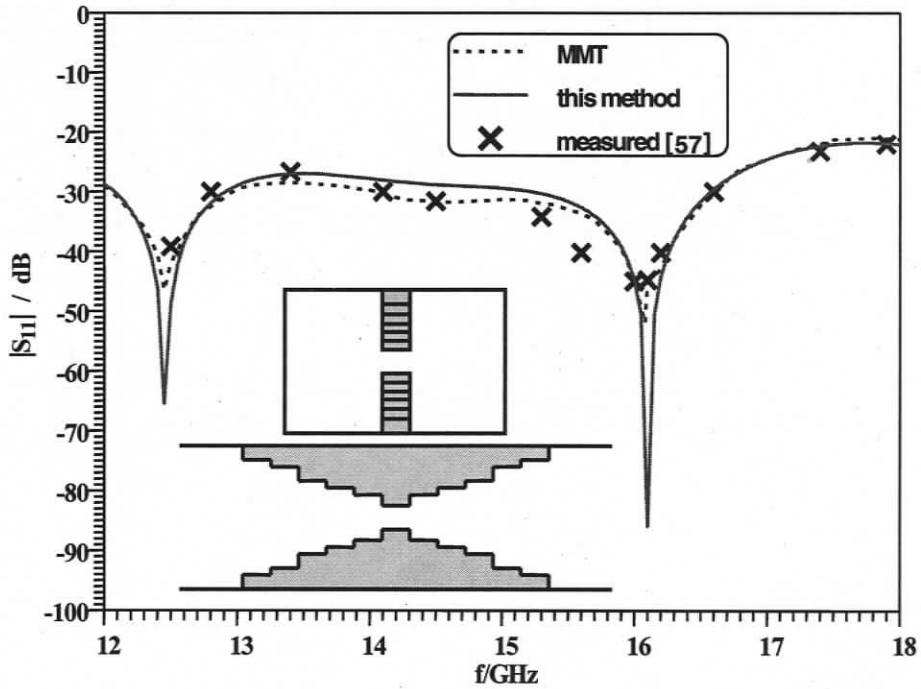

Fig. 4.8b Stepped back-to-back connected ridge waveguide transformer: S_{11} performance.

4.4.3 Standard Waveguide Filters

The following two filter components would normally not be designed using this technique since all eigenvalues and functions involved are analytically known. However, they are selected here to demonstrate that even in cases where the ridges are placed such that smaller regular waveguides are obtained, the eigenvalue formulation performs accurately. Fig. 4.9a and Fig. 4.9b show the structure and performance of an inductive iris filter where two ridges are placed such that they cover each approximately one quarter of the cross section of the rectangular waveguide. The eigenvalue formulation correctly computes the eigenvalues and eigenvectors of the apertures formed by the irises as demonstrated by excellent agreement with results obtained with the Coupled-Integral-Equation Technique (CIET).

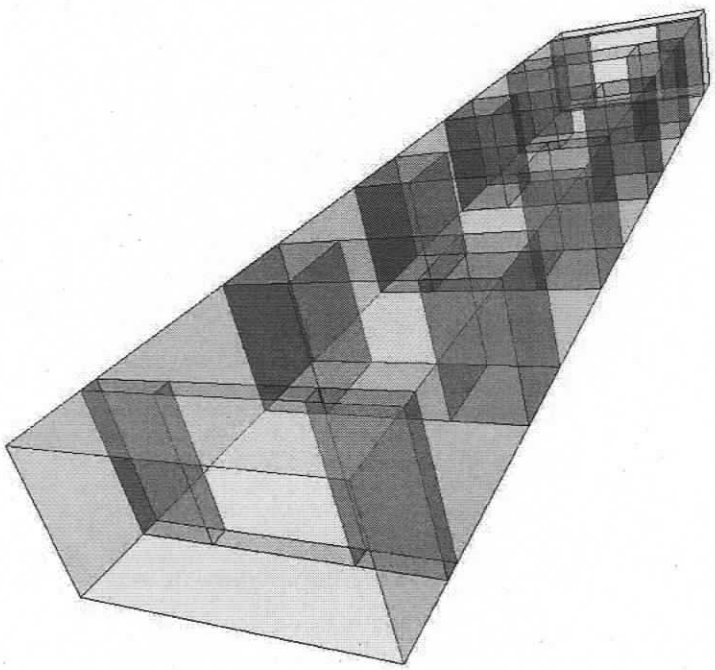

Fig. 4.9a Four-resonator inductive-iris filter.

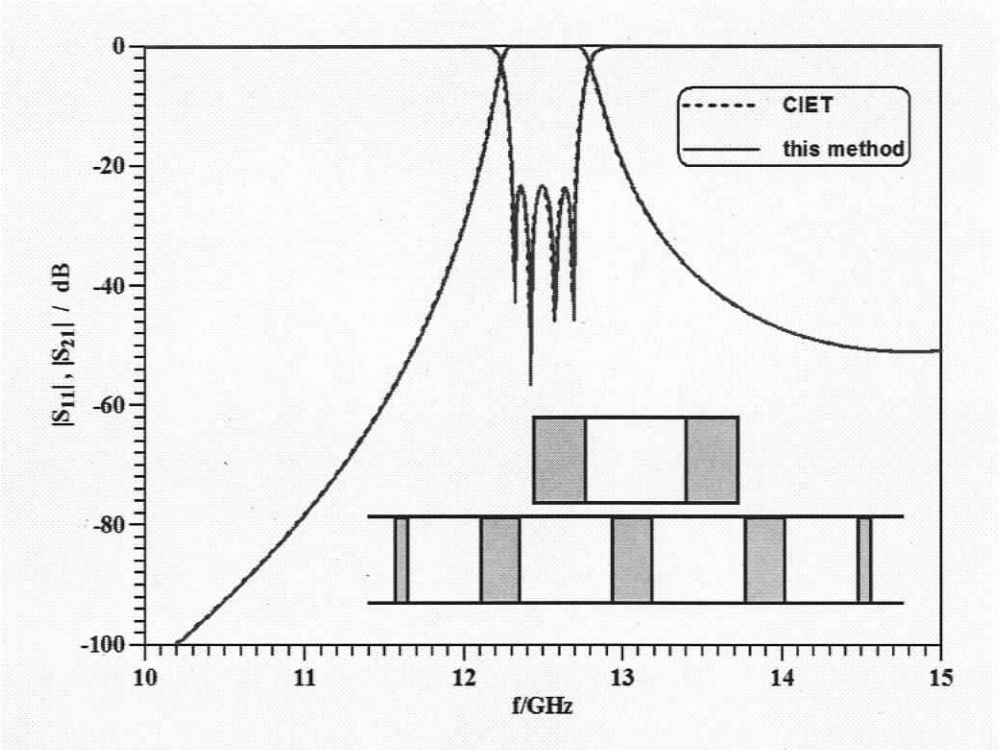

Fig. 4.9b Four-resonator inductive-iris filter: performance comparison.

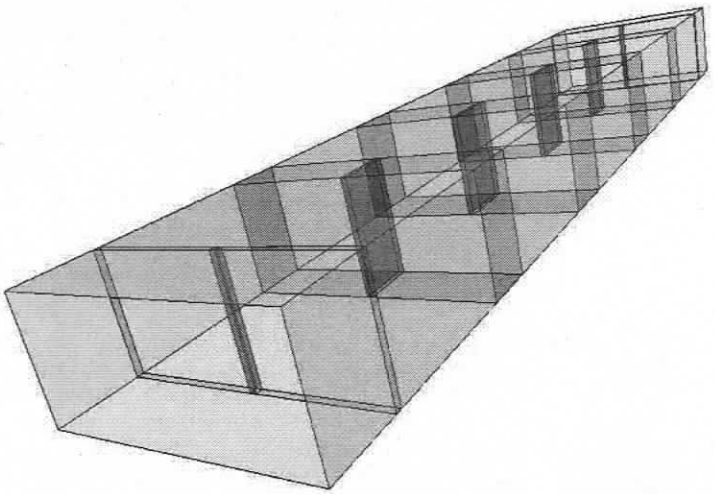

Fig. 4.10a Five-resonator metal-insert filter.

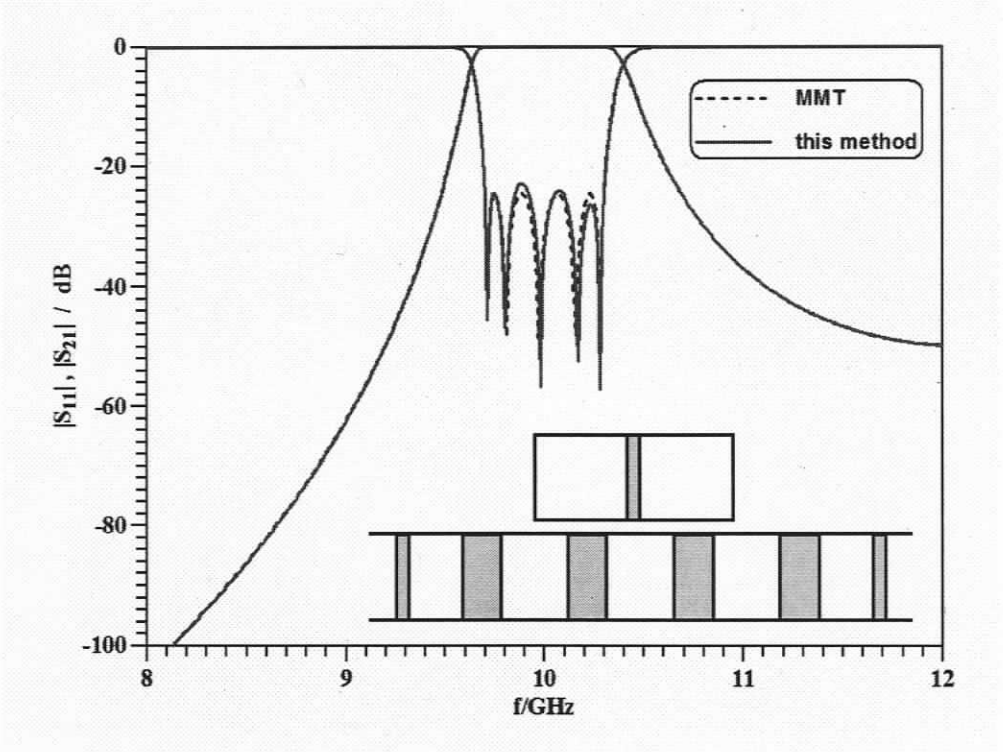

Fig. 4.10b Five-resonator metal-insert filter: performance comparison.

An interesting case is that of the metal-insert filter presented in Fig. 4.10a. During the algorithm development, only one single ridge is used to satisfy the cross section while others are set to zero without any additional change to the code. Furthermore, the eigenvalues appear in pairs – as expected – with each pair representing those of both the left and the right apertures. The excellent agreement with MMT results in Fig. 4.10b verifies the applicability of this technique to 'standard' waveguide problems.

4.4.4 Below-Cutoff Waveguide Filters

In the lower Gigahertz frequency range, waveguide filter components are usually bulky and encounter serious shortcoming in operational bandwidth. The introduction of ridged discontinuities into a rectangular waveguide results in a significant lowering of the dominant-mode cutoff frequency and, therefore, a ridged waveguide has great potential to overcome these disadvantages, and it can be used to produce evanescent-mode waveguide filters. These filters are well known for their wide stopbands and their compact size compared to conventional coupled resonator filters.

Fig. 4.11a presents a six-resonator below-cutoff T-septum waveguide filter for the lower Gigahertz range. Note that the input and output ports are in ridged waveguide (T-septum) technology and, therefore, the empty waveguide sections are used as coupling sections operating below cutoff. Fig. 4.11b shows the performance of the below-cutoff T-septum waveguide filter as proposed in [45] over a wide frequency range. Excellent agreement is obtained with the results of an approach that combines the Coupled Integration-Equation Technique (CIET) with the MMT. Especially the passband peaks at 7.6 GHz and 7.8 GHz are accurately reproduced which attests to an accurate calculation of the mode spectrum of the T-septum waveguide sections. For a close-up comparison of the excellent S-parameters agreements around 2.15 GHz, Fig. 4.11c also denotes consistence with an all-MMT approach. In order to demonstrate agreement with respect to phase calculations, the group-delay response is shown in Fig. 4.11d and also shows excellent agreement with the combined MMT-CIET approach.

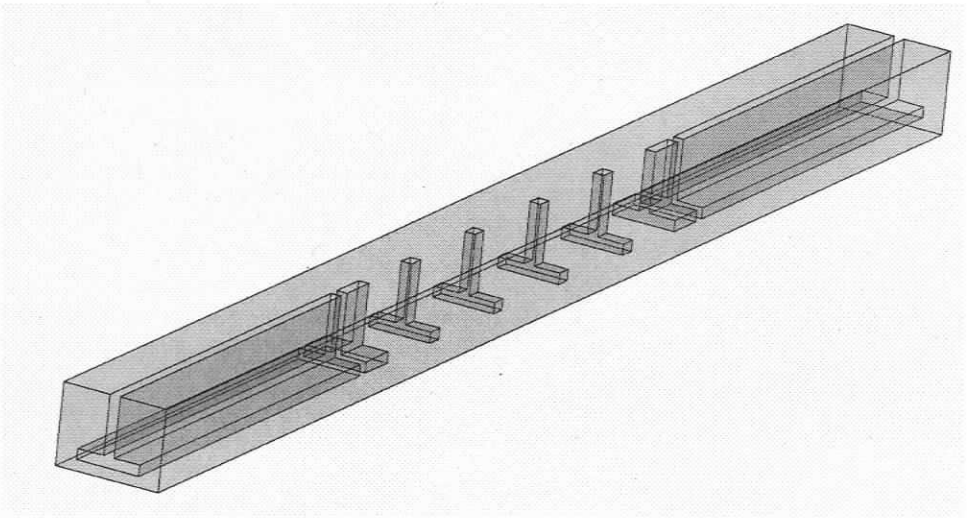

Fig. 4.11a Six-resonator below-cutoff T-septum waveguide filter.

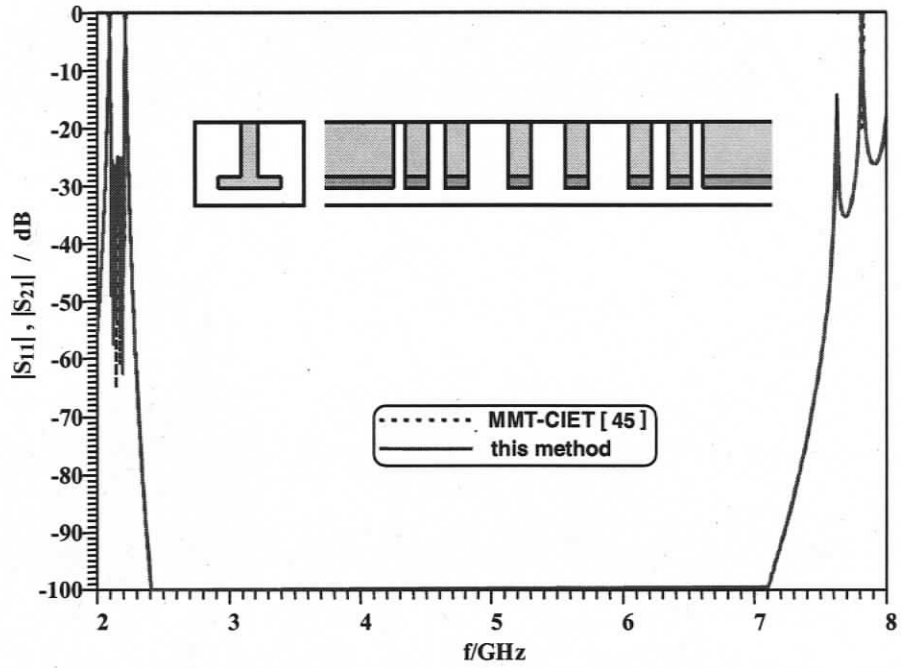

Fig. 4.11b Six-resonator below-cutoff T-septum waveguide filter: S-parameters over a wide frequency range.

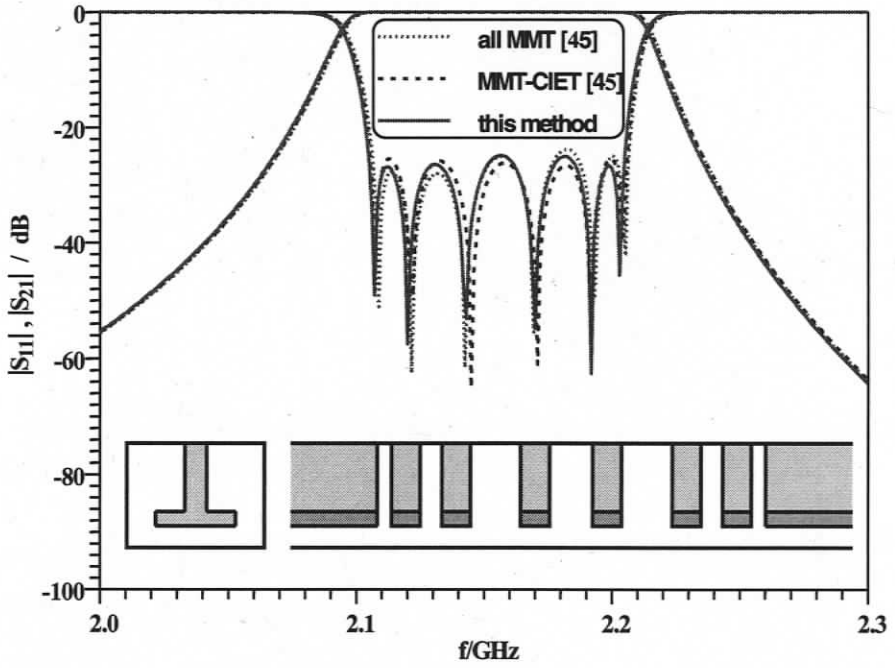

Fig. 4.11c Six-resonator below-cutoff T-septum waveguide filter: S-parameters in the passband.

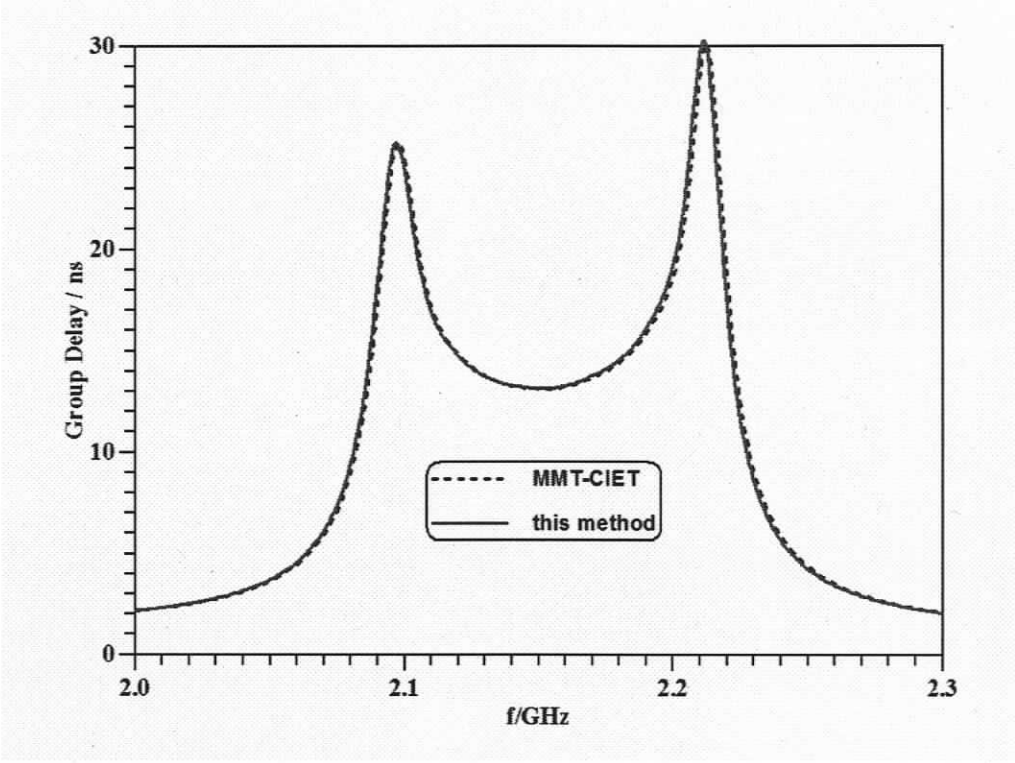

Fig. 4.11d Six-resonator below-cutoff T-septum waveguide filter: group-delay.

The following two examples involve below-cutoff ridge waveguide filters with slightly different shapes. They have in common that they would have to be separately analyzed and coded with an all-MMT approach as pointed out in Chapter 3. Fig. 4.12 shows the performance of a below-cutoff filter with pedestals. The cutoff frequency of the pedestalled ridge cross section is close to 3.5 GHz. A six-resonator filter with wide stopband characteristics is obtained after optimization of individual section lengths.

The structure used in Fig. 4.13 is very similar, but instead of the pedestal, this ridge is converted into a smaller ridge section which can serve – if more of such smaller sections are incorporated in the cross section – as a way of modeling rounded ridges. The performance of such a below-cutoff ridge waveguide filter is similar to that of Fig. 4.12, except for the reduced return loss at the lower midband frequency.

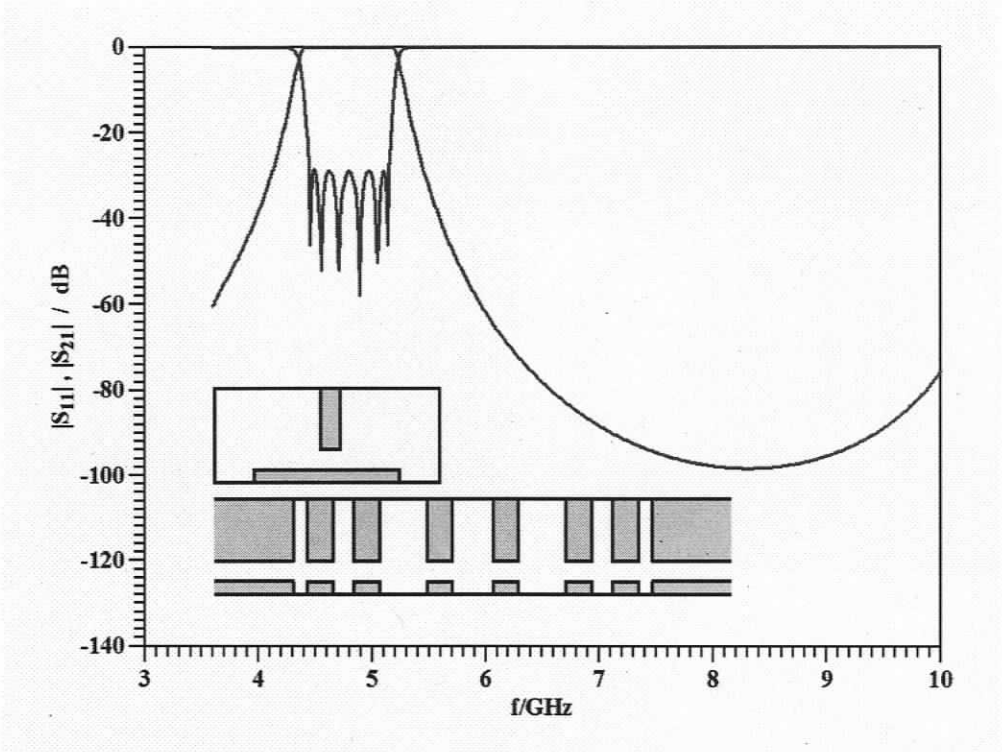

Fig. 4.12 Performance of a six-resonator below-cutoff ridge waveguide filter with pedestals.

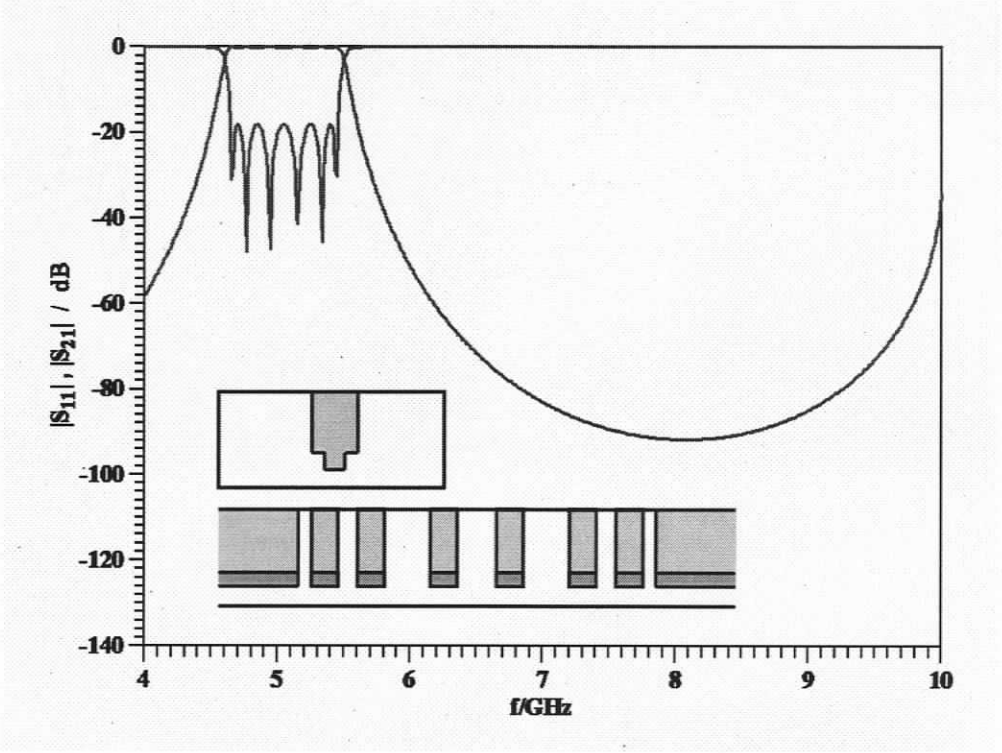

Fig. 4.13 Performance of a six-resonator below-cutoff ridge waveguide filter with two different ridges in the cross section.

4.4.5 Rectangular Waveguide Twist

90-degree waveguide twists are frequently used in waveguide feed networks. They can be designed as a continuously twisted rectangular waveguide involving a few discontinuities operating as polarization rotator over a given frequency range. The 90-degree waveguide twist component shown in Fig. 4.14(a) is designed for operation between 12 and 13 GHz. It must be analyzed/optimized by a full set of modes as its cross section is asymmetric. The excellent agreement of our results (solid lines) with those of the μWave Wizard (dashed lines) and Ansoft HFSS (dotted lines) demonstrates that our eigenvalue technique correctly computes waveguide components involving different polarizations. Note that the twist can also be viewed as a filter, where the two lowest modes in the ridged guide provide the two resonances at 12.1 GHz and 12.8 GHz. The attenuation pole at 14 GHz is produced by bypass coupling from the input to the second resonance, which is identical to that from the first resonance to the output. Note that the operation of this twist is similar to that presented in [60]. However, it is easier to fabricate due to the involvement of only rectangular ridges.

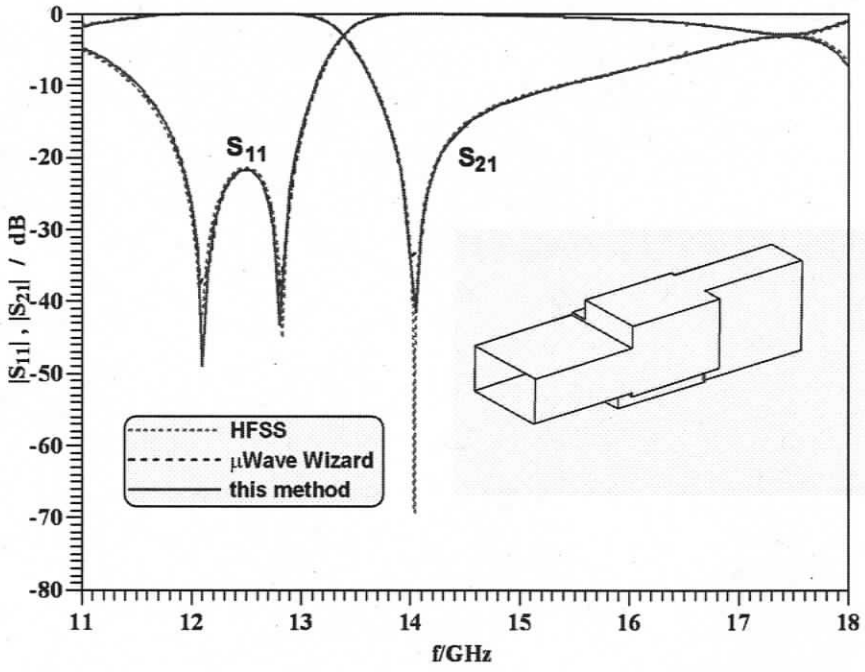

(a)

Fig. 4.14 (a) Performance of a 90-degree rectangular waveguide twist: this method (solid lines), μWave Wizard (dashed lines), Ansoft HFSS (dotted lines); (b) CPU-time comparison.

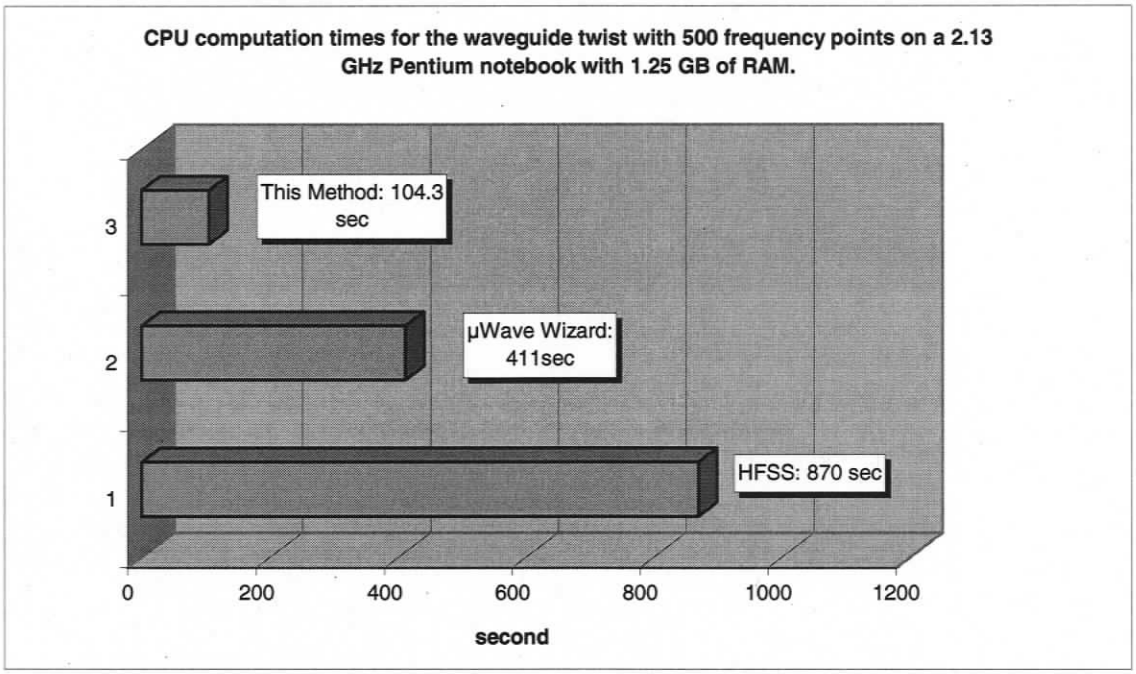

(b)

Fig. 4.14 Continued.

It is worth noting that the simulation of such an asymmetric structure using commercial software becomes time consuming because of discontinuities encountered on all coordinate planes. Using the method proposed in this thesis, the computation of the waveguide twist with 500 frequency points requires 104.3 seconds of CPU time on a 2.13 GHz Pentium notebook with 1.25 GB of RAM (cf. Fig 4.14b). The commercial package µWave Wizard takes 411 seconds for the total calculations from 11 GHz to 18 GHz with 500 frequency points. HFSS simulation results require 14 minutes and 30 seconds of CPU time, and reach 21 minutes and 7 seconds in real time running on the same machine. (Note that both commercial packages use a finite-element solver for the mode-spectrum analysis. The additional time used by HFSS, compared to the µWave Wizard, is due to a finite-element approach also in propagation direction, whereas the µWave Wizard uses the MMT.) This example demonstrates that the mode-spectrum analysis presented in this thesis outperforms commercially available full-wave software when dealing with complex ridged waveguide configurations.

4.4.5 Optimization of Waveguide Filter Structures

Accurate design of complex waveguide devices and components can often be achieved through sophisticated optimization methods. It is generally accepted that a method based on the gradient of the cost function is the most common tool for optimization of microwave structures as long as a good initial design is available. In this thesis, initial designs for regular waveguide filters, e.g. Fig. 4.9 and Fig. 4.10, are obtained from standard filter theory including impedance inverters [6], [61]. Below-cutoff filter dimensions can be obtained similarly when considering the effective wavelength caused by a resonator and adjacent below cutoff sections [62]. Following the initial design, the parameters of a waveguide structure between input and output ports are then optimized using a gradient based method [63]. The error function to be minimized for filter design is

$$\text{error function} = \sum_{i\_pass} \frac{\text{RL\_goal}(f_{i\_pass})}{\text{RL}(f_{i\_pass})} + \sum_{i\_stop} \frac{\text{IL\_goal}(f_{i\_stop})}{\text{IL}(f_{i\_stop})} \tag{4.23}$$

where $RL\_goal(f_{i\_pass})$, $IL\_goal(f_{i\_stop})$ are the desired return loss and insertion loss, and $RL(f_{i\_pass})$, $IL(f_{istop})$ the actual return loss and insertion loss at frequencies f_{i_pass} and f_{i_stop}, respectively.

Another option for future implementation might use a combination of the code developed in this work with commercially available circuit simulations and/or optimizers, e.g., Advanced Design System (ADS).

4.5 Conclusion

The major objective of this chapter has been to expand the eigenvalue mode-spectrum approach to a general, accurate numerical tool for the design of multiple ridged rectangular waveguide components. Individual discontinuities, cascaded ridges as well as waveguide components, such as transformers, filters, and a twist, are analyzed and designed. Excellent agreement with measurements and results obtained with other techniques verifies the eigenvalue mode-spectrum procedure presented in this thesis.

Chapter 5 MULTI-RIDGED CIRCULAR WAVEGUIDES

5.1 Introduction

A natural progression from multi-ridged cross sections in rectangular waveguides is to expand the theoretical and numerical analysis to include ridged circular waveguides. This chapter proposes a complete formulation for determining the mode spectrum and the generalized scattering matrix for multi-ridged circular waveguide structures with applications to polarizers, below-cutoff filters and polarization rotating components.

Circular waveguides are commonly used in antenna feed systems, most often as a building block of primary feeds, polarizers, rotary joints, and others. A cross section involving multiple ridges in a circular waveguide, as shown in Fig. 5.1, can provide more efficient control of propagation characteristics compared with standard circular waveguides. Their distinctive features include lower cutoff frequencies of the fundamental mode, compact size and easily controllable polarization. For the accurate analysis and design of such components, the knowledge of the eigenmode spectrum is of utmost importance, as it determines such critical quantities as resonator lengths, inter-cavity direct or cross-coupling, phase relationships, etc. The modal scattering parameters of the discontinuity from the circular to multi-ridged circular waveguide are then evaluated based on these eigenvalue solutions.

This chapter discusses the eigenvalue analysis in ridged circular waveguide using a theory similar to that proposed for multi-ridged rectangular waveguides in Chapter 4. The arbitrarily placed ridges are assumed to be shaped conically in order to fit the cylindrical coordinate system. It is worth mentioning here that rectangular cross section ridges can be approximated with pie-shaped ridges. This has been efficiently demonstrated in [44].

The chapter is divided into two main parts. The first part examines the technique to determine the entire eigenmode spectrum and the coupling matrices for the three-dimensional modal analysis. The second part deals with the evaluation of the proposed

algorithms and its demonstration for examples such as circular polarizers, below-cutoff filters and polarization rotating components.

5.2 Complete Analysis of Multi-Ridged Circular Waveguides

The circular waveguide with asymmetric multiple ridges in Fig. 5.1 is solved in the cylindrical coordinates system. Following the general approach presented in Chapter 4, the eigenvalue mode spectrum can be evaluated by respecting the boundary conditions of the multi-ridged cross section.

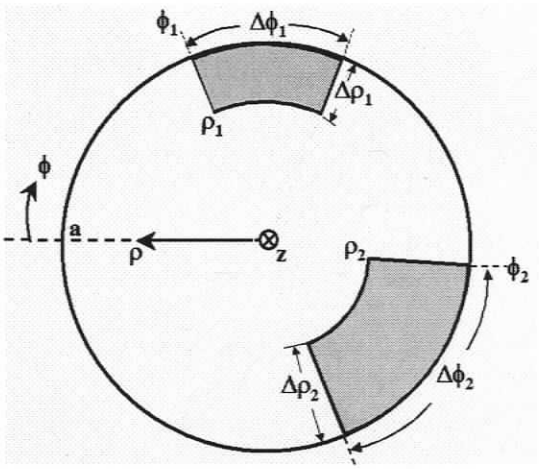

Fig. 5.1 Cross section of multiple ridges in circular waveguide.

Although the field components involve Bessel functions in radial direction of a circular waveguide, the angular dependence is given by sines and cosines, and therefore the set of basis functions for both TE and TM modes can be written as

$$h_{zp(m,n)} = J_m\left(k_{chmn}\rho\right)\begin{Bmatrix}\cos(m\phi)\\ \sin(m\phi)\end{Bmatrix} \tag{5.1}$$

$$e_{zp(l,k)} = J_l\left(k_{celk}\rho\right)\begin{Bmatrix}\sin(l\phi)\\ \cos(l\phi)\end{Bmatrix}\prod_{n=1}^{N}\Omega\left(\frac{\rho-\rho_n}{\Delta\rho_n},\frac{\phi-\phi_n}{\Delta\phi_n}\right) \tag{5.2}$$

where J denotes Bessel functions of the first kind, $k_{ch,e}$ are the well-known cutoff wavenumbers in the empty housing, and function Ω is the constraint function in the circular ridged case, which is equivalent to (4.12). The introduced constraint function enforces the TM-mode boundary conditions over the cross sections of the ridges.

5.2.1 TE and TM Modes of Multi-Ridged Circular Waveguides

The proposed algorithm first follows the classical eigenvalue method to calculate the K and M matrices used in Sections 4.4 and 4.5. For TE modes

$$\left(K_h\right)_{i,j} = \frac{1}{A_i^2} - k_{chi}k_{chj}\sum_{n=1}^{N}\left\{\int_{\rho_n}^{\rho_n+\Delta\rho_n} J_m'\left(k_{chi}\rho\right)J_l'\left(k_{chj}\rho\right)\rho d\rho \int_{\phi_n}^{\phi_n+\Delta\phi_n}\begin{Bmatrix}\cos(m\phi)\\ \sin(m\phi)\end{Bmatrix}\begin{Bmatrix}\cos(l\phi)\\ \sin(l\phi)\end{Bmatrix}d\phi\right\}$$
$$-ml\sum_{n=1}^{N}\left\{\int_{\rho_n}^{\rho_n+\Delta\rho_n} J_m\left(k_{chi}\rho\right)J_l\left(k_{chj}\rho\right)\frac{d\rho}{\rho} \int_{\phi_n}^{\phi_n+\Delta\phi_n}\begin{Bmatrix}\sin(m\phi)\\ \cos(m\phi)\end{Bmatrix}\begin{Bmatrix}\sin(l\phi)\\ \cos(l\phi)\end{Bmatrix}d\phi\right\} \tag{5.3}$$

$$\left(M_h\right)_{i,j} = \frac{1}{\left(A_i k_{chi}\right)^2} - \sum_{n=1}^{N}\left\{\int_{\rho_n}^{\rho_n+\Delta\rho_n} J_m\left(k_{chi}\rho\right)J_l\left(k_{chj}\rho\right)\rho d\rho \int_{\phi_n}^{\phi_n+\Delta\phi_n}\begin{Bmatrix}\cos(m\phi)\\ \sin(m\phi)\end{Bmatrix}\begin{Bmatrix}\cos(l\phi)\\ \sin(l\phi)\end{Bmatrix}d\phi\right\} \tag{5.4}$$

In (5.3) and (5.4) , indices m, l are the respective orders of Bessel functions appearing in orders i, j of increasing wavenumbers of the circular housing, and A_i is the normalization coefficient of TE modes

$$A_{(i\to m,n)} = \sqrt{\frac{2}{\pi(1+\delta_{om})}}\frac{1}{\sqrt{x_{mn}'^2 - m^2}J_m\left(x_{mn}'\right)} \tag{5.5}$$

with x'_{mn} being the nth zero of the derivative of J_m, and the prime denotes the derivative with respect to the argument.

For TM modes,

$$\left(K_e\right)_{i,j} = \frac{1}{D_i^2} - \left(K_{e\delta}\right)_{i,j}$$
$$-k_{cei}k_{cej}\sum_{n=1}^{N}\left\{\int_{\rho_n}^{\rho_n+\Delta\rho_n} J_m'\left(k_{cei}\rho\right)J_l'\left(k_{cej}\rho\right)\rho d\rho \int_{\phi_n}^{\phi_n+\Delta\phi_n}\begin{Bmatrix}\sin(m\phi)\\ \cos(m\phi)\end{Bmatrix}\begin{Bmatrix}\sin(l\phi)\\ \cos(l\phi)\end{Bmatrix}d\phi\right\}$$
$$-ml\sum_{n=1}^{N}\left\{\int_{\rho_n}^{\rho_n+\Delta\rho_n} J_m\left(k_{cei}\rho\right)J_l\left(k_{cej}\rho\right)\frac{d\rho}{\rho} \int_{\phi_n}^{\phi_n+\Delta\phi_n}\begin{Bmatrix}\cos(m\phi)\\ -\sin(m\phi)\end{Bmatrix}\begin{Bmatrix}\cos(l\phi)\\ -\sin(l\phi)\end{Bmatrix}d\phi\right\} \tag{5.6}$$

$$(M_e)_{i,j} = \frac{1}{(D_i k_{cei})^2} - \sum_{n=1}^{N} \left\{ \int_{\rho_n}^{\rho_n+\Delta\rho_n} J_m(k_{cei}\rho) J_l(k_{cej}\rho) \rho d\rho \int_{\phi_n}^{\phi_n+\Delta\phi_n} \begin{Bmatrix} \sin(m\phi) \\ \cos(m\phi) \end{Bmatrix} \begin{Bmatrix} \sin(l\phi) \\ \cos(l\phi) \end{Bmatrix} d\phi \right\} \tag{5.7}$$

$$D_{(i\to m,n)} = \sqrt{\frac{2}{\pi(1+\delta_{om})}} \frac{1}{x_{mn} J_m(x_{mn})} \tag{5.8}$$

D_i is the normalization coefficient for TM modes, and x_{mn} is the nth zero of J_m. Matrix $K_{e\delta}$ contains the results from the integration of the derivatives of the constraint function similar to (4.17). Its elements are given by

$$\begin{aligned}
(K_{e\delta})_{i,j} = \sum_{n=1}^{N} \Big\{ & \rho_n \left(J_m(k_{cei}\rho_n) J_l(k_{cej}\rho_n) - k_{cej} J_m(k_{cei}\rho_n) J_l'(k_{cej}\rho_n) - k_{cei} J_m'(k_{cei}\rho_n) J_l(k_{cej}\rho_n) \right) \\
& + (\rho_n + \Delta\rho_n) J_m(k_{cei}(\rho_n + \Delta\rho_n)) J_l(k_{cej}(\rho_n + \Delta\rho_n)) \\
& - (\rho_n + \Delta\rho_n) k_{cej} J_m(k_{cei}(\rho_n + \Delta\rho_n)) J_l'(k_{cej}(\rho_n + \Delta\rho_n)) \\
& - (\rho_n + \Delta\rho_n) k_{cei} J_m'(k_{cei}(\rho_n + \Delta\rho_n)) J_l(k_{cej}(\rho_n + \Delta\rho_n)) \Big\} \int_{\phi_n}^{\phi_n+\Delta\phi_n} \begin{Bmatrix} \sin(m\phi_n) \\ \cos(m\phi_n) \end{Bmatrix} \begin{Bmatrix} \sin(l\phi_n) \\ \cos(l\phi_n) \end{Bmatrix} d\phi \\
& + \sum_{n=1}^{N} \left\{ \begin{Bmatrix} \sin(m\phi_n) \\ \cos(m\phi_n) \end{Bmatrix} \begin{Bmatrix} \sin(l\phi_n) \\ \cos(l\phi_n) \end{Bmatrix} - l \begin{Bmatrix} \sin(m\phi_n) \\ \cos(m\phi_n) \end{Bmatrix} \begin{Bmatrix} \cos(l\phi_n) \\ -\sin(l\phi_n) \end{Bmatrix} - m \begin{Bmatrix} \cos(m\phi_n) \\ -\sin(m\phi_n) \end{Bmatrix} \begin{Bmatrix} \sin(l\phi_n) \\ \cos(l\phi_n) \end{Bmatrix} \right. \\
& + \begin{Bmatrix} \sin(m(\phi_n + \Delta\phi_n)) \\ \cos(m(\phi_n + \Delta\phi_n)) \end{Bmatrix} \begin{Bmatrix} \sin(l(\phi_n + \Delta\phi_n)) \\ \cos(l(\phi_n + \Delta\phi_n)) \end{Bmatrix} + l \begin{Bmatrix} \sin(m(\phi_n + \Delta\phi_n)) \\ \cos(m(\phi_n + \Delta\phi_n)) \end{Bmatrix} \begin{Bmatrix} \cos(l(\phi_n + \Delta\phi_n)) \\ -\sin(l(\phi_n + \Delta\phi_n)) \end{Bmatrix} \\
& \left. + m \begin{Bmatrix} \cos(m(\phi_n + \Delta\phi_n)) \\ -\sin(m(\phi_n + \Delta\phi_n)) \end{Bmatrix} \begin{Bmatrix} \sin(l(\phi_n + \Delta\phi_n)) \\ \cos(l(\phi_n + \Delta\phi_n)) \end{Bmatrix} \right\} \int_{\rho_n}^{\rho_n+\Delta\rho_n} J_m(k_{cei}\rho) J_l(k_{cej}\rho) \frac{d\rho}{\rho}
\end{aligned} \tag{5.9}$$

The eigenvalues and eigenvectors are then generated by proper numerical routines, e.g. [64]. While some of the integrals can be solved analytically, most of them have to be evaluated numerically [65]. This completes the mode spectrum analysis of two-dimensional multi-ridged circular waveguides.

5.2.2 Convergence Analysis

Similar to Section 4.3 for rectangular multi-ridged waveguides, Fig. 5.3 shows the TE and TM mode cutoff frequencies versus the highest cutoff frequency of the basis

functions. Solutions for both vertical and horizontal polarizations of a double-ridged circular waveguide (Fig. 5.2) are shown in Fig. 5.3a and Fig. 5.3b, respectively. Convergence is demonstrated, and the converged cutoff frequencies are found in agreement with results obtained from a 2D-MMT code (not shown here). Note that similar to the rectangular ridged cross sections of Fig. 4.3 and Fig. 4.4, convergence for the TM modes is slower due to the use of the very simple constraint function.

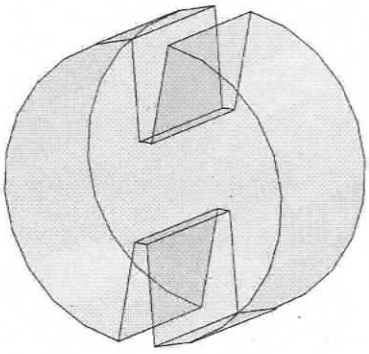

Fig. 5.2 Double-ridged circular waveguide.

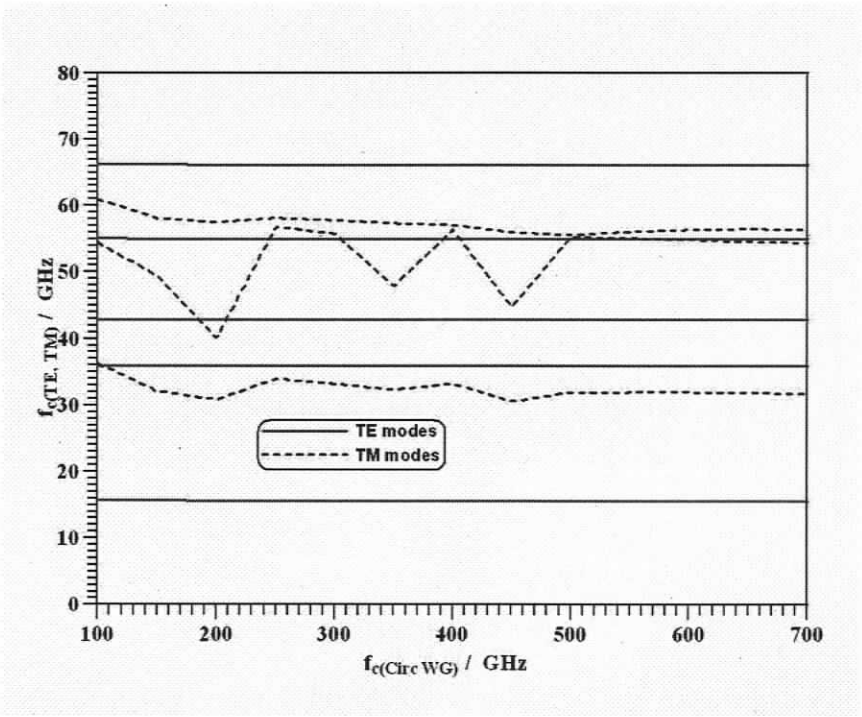

Fig. 5.3a Convergence analysis of double-ridged circular waveguide in vertical polarizations.

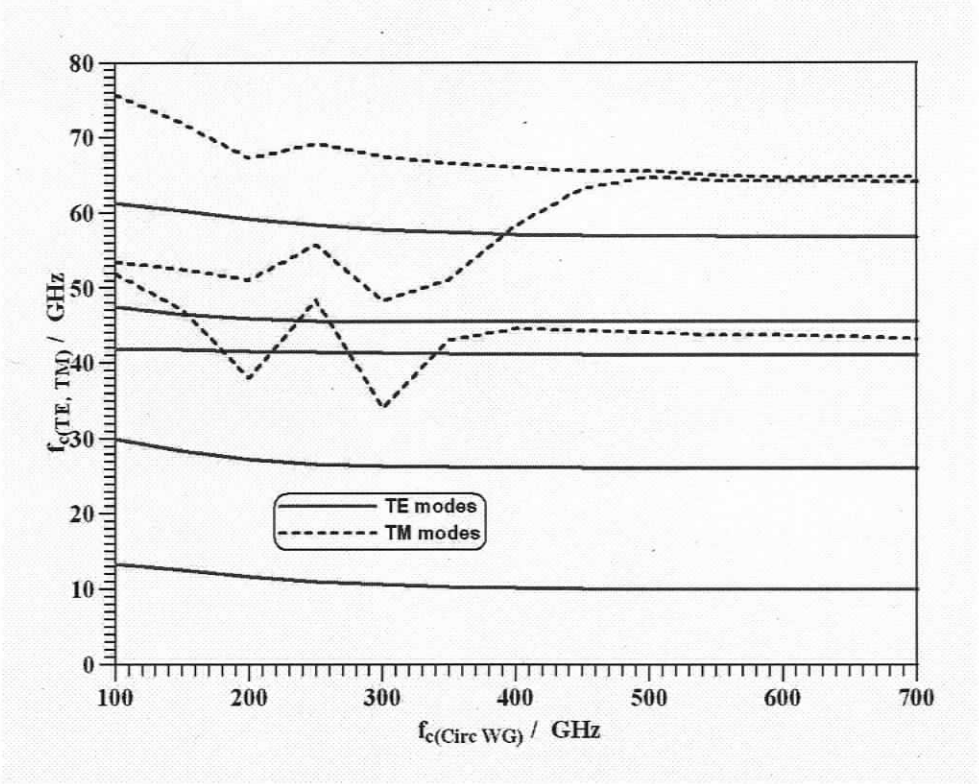

Fig. 5.3b Convergence analysis of double-ridged circular waveguides in horizontal polarizations.

5.2.3 Circular-to-Multi-Ridged Circular Waveguide Discontinuity

The eigenvalue analysis of multi-ridged circular waveguides was discussed in the previous subsections. However, this is only the first step in the design of circular ridged waveguides components. For a rigorous analysis involving generalized scattering matrices, it is essential to evaluate the S-parameters of every discontinuity based on the interaction of the fundamental and higher order modes. Therefore, MMT routines combined with the eigenvalue mode-spectrum analysis are again employed to construct the coupling matrix J in form of

$$J = \begin{bmatrix} J_{hh} & 0 \\ J_{eh} & J_{ee} \end{bmatrix} \tag{5.10}$$

Note that what was stated for rectangular multi-ridge waveguides regarding matrices J_{ee}, K_e and $K_{e\delta}$, applies in the same way to the circular multi-ridge case. Finally, the coupling matrix J_{hh}, J_{ee} and J_{eh} are computed from

$$\left(J_{hh}\right)_{q,i} = A_q \sum_{p=1}^{P_h} \left(K_h\right)_{ip} \left(c_h\right)_{ip} \tag{5.11}$$

$$\left(J_{ee}\right)_{q,j} = D_q \sum_{p=1}^{P_e} \left(K_e\right)_{jp} \left(c_e\right)_{jp} \tag{5.12}$$

$$\begin{aligned}\left(J_{eh}\right)_{q,i} = D_q \{ & k_{ceq} \sum_{p=1}^{P_h} l\left(c_h\right)_{ip} \sum_{n=1}^{N} \int_{\rho_n}^{\rho_n+\Delta\rho_n} J_m'\left(k_{ceq}\rho\right) J_l\left(k_{chj}\rho\right) d\rho \int_{\phi_n}^{\phi_n+\Delta\phi_n} \begin{Bmatrix} \sin(m\phi) \\ \cos(m\phi) \end{Bmatrix} \begin{Bmatrix} -\sin(l\phi) \\ \cos(l\phi) \end{Bmatrix} d\phi \\ & - m \sum_{p=1}^{P_h} k_{chp} \left(c_h\right)_{ip} \sum_{n=1}^{N} \int_{\rho_n}^{\rho_n+\Delta\rho_n} J_m\left(k_{ceq}\rho\right) J_l'\left(k_{chj}\rho\right) d\rho \int_{\phi_n}^{\phi_n+\Delta\phi_n} \begin{Bmatrix} \cos(m\phi) \\ -\sin(m\phi) \end{Bmatrix} \begin{Bmatrix} \cos(l\phi) \\ \sin(l\phi) \end{Bmatrix} d\phi\end{aligned} \tag{5.13}$$

Of course, matrices J_{hh}, K_h and J_{ee}, K_e are pre-calculated during the mode-spectrum analysis. The additional computation only involves the matrix J_{eh} of the circular-to-ridged-circular discontinuity. It is obvious that all the coupling integrals are frequency independent and, hence, the numerical integration is not repeatedly evaluated at every frequency point. This procedure is thus rigorous and yet computationally efficient.

Since the proposed algorithms are for arbitrarily located ridges in circular waveguides, the individual sine and cosine functions in (5.1) - (5.13) are valid only for their respective cross-sectional symmetries. For asymmetric circular multi-ridged cross sections such as depicted in Fig. 5.1, all four possible combinations must be considered. Hence the coupling matrices J_{hh} , J_{ee} and J_{eh} can be expanded in terms of sub-matrices as shown below.

$$J = \begin{bmatrix} J_{hh} & 0 \\ J_{eh} & J_{ee} \end{bmatrix} = \begin{bmatrix} \begin{pmatrix} J_{hh}^{cc} & J_{hh}^{cs} \\ J_{hh}^{sc} & J_{hh}^{ss} \end{pmatrix} & 0 \\ \begin{pmatrix} J_{eh}^{cc} & J_{eh}^{cs} \\ J_{eh}^{sc} & J_{eh}^{ss} \end{pmatrix} & \begin{pmatrix} J_{ee}^{cc} & J_{ee}^{cs} \\ J_{ee}^{sc} & J_{ee}^{ss} \end{pmatrix} \end{bmatrix} \tag{5.14}$$

The superscripts "*ss*", "*sc*", "*cs*", "*cc*" indicate the coupling from sine to sine, sine to cosine, cosine to cosine and cosine to sine polarizations of the empty circular waveguide to the multi-ridged circular waveguide, respectively.

The complete analysis and design procedures are finalized by using the generalized S-matrix method presented in Chapter 3. The overall performances of ridged circular

waveguide components are numerically determined and compared with data obtained from independent full-wave modeling tools.

5.3 Ridged Circular Waveguides Components

The advantage of the circular ridged waveguide mode-spectrum analysis is demonstrated for individual components. This section presents computer-aided designs for cascaded waveguide components, waveguide polarizers, below-cutoff waveguide filters, and a waveguide polarization rotator. By comparison with the data from independent full-wave computations, the proposed algorithm for multi-ridged circular waveguide components is verified.

5.3.1 Double Ridged Circular Waveguide Section

To validate the proposed approach, a single ridged circular waveguide structure is selected as an example of a two-port discontinuity. The radius of the empty circular waveguide is a =6.0mm, the radial ridge dimension is 4.0mm, with 15 degree width as shown in Fig. 5.4.

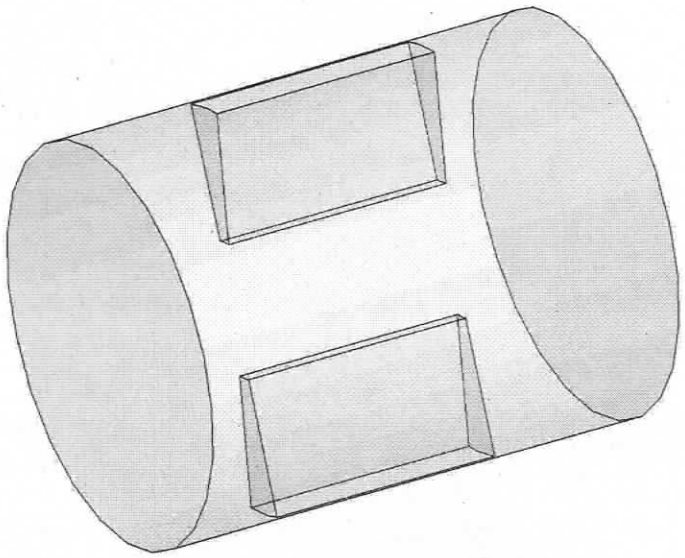

Fig. 5.4 Double-ridged section in circular waveguide.

Fig. 5.5 shows the performance of the double-ridged waveguide between two standard circular waveguides. The reflection coefficients for vertical (VP) and horizontal (HP) polarizations are plotted along with the phase difference between the two polarizations. This can be achieved by either separately using the two (cosine and sine) polarizations given in Section 5.2, or by using only one of the two and performing two separate calculations, with the positions of the ridges rotated by 90 degrees in the second run. The excellent agreement of our results (solid lines) in magnitude and phase with those obtained with the MMT (e.g. [44]) validates the eigenvalue analysis for multi-ridged circular waveguides

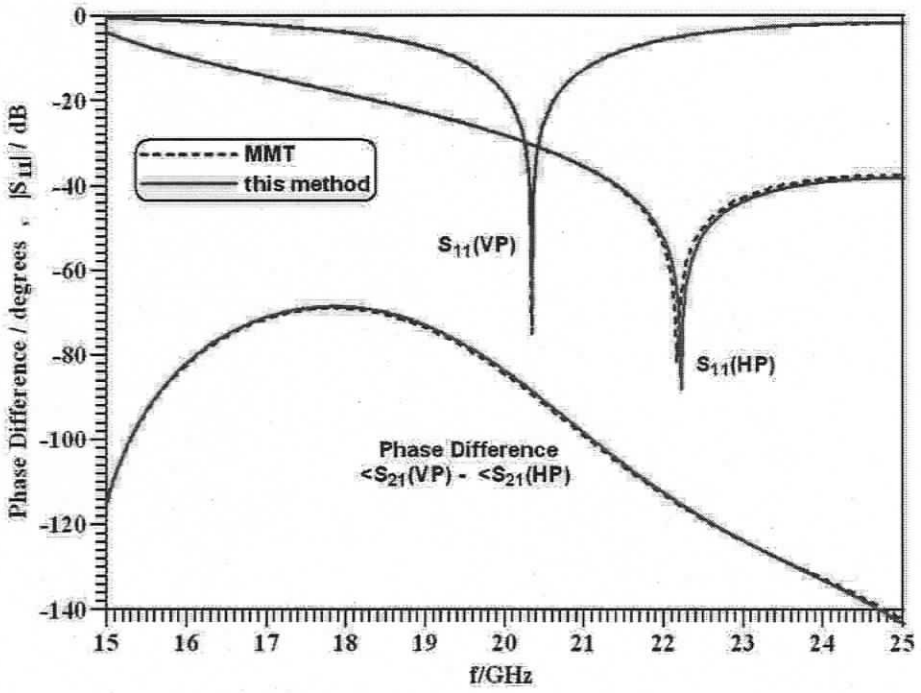

Fig. 5.5 Double-ridged section in circular waveguide: this method (solid lines), MMT (dashed lines).

5.3.2 Circular Ridged Waveguide Polarizer

A direct application of the building block structure in Fig. 5.4 is a circular ridged waveguide polarizer [44] as shown in Fig 5.6a. The incoming TE_{11} mode excites the polarizer at an angle of 45 degrees. The two associated polarizations (vertical and horizontal) possess the same field strengths at input but progress differently through the

ridged structure. Whereas the vertical polarization experiences capacitive behavior, that of the horizontal component is inductive. The ridged and empty waveguide sections are optimized to yield almost identical field strengths of the two polarizations at output with a phase difference of 90 degrees. Whether the outgoing wave is clockwise or counter-clockwise circularly polarized depends on the angle of incidence, which is either -45 or +45 degrees from the vertical, respectively. This polarizer structure has input/output ports with radius of 6.0 mm. Its 11 ridged sections contain double ridges with 12 degrees thickness and 1.5 mm height. The component is designed for operation between 19 GHz and 22 GHz with the following specifications: 30 dB return loss and isolation, 0.75 dB axial ratio. Excellent agreement of those parameters with results from the MMT is demonstrated in Fig. 5.6b and validates the eigenvalue technique presented here.

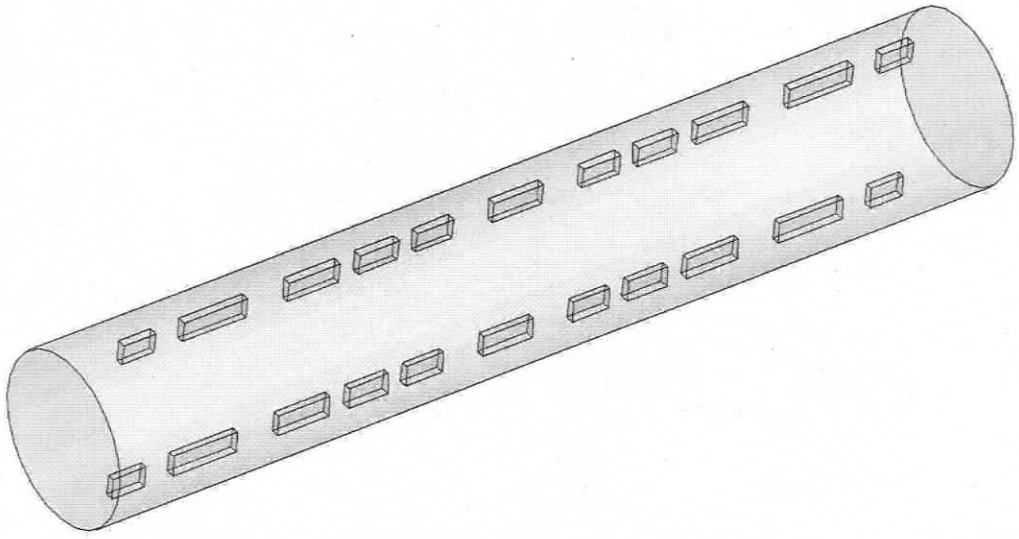

(a)

Fig. 5.6 A circular ridged waveguide polarizer with 11 ridged sections: (a) three-dimensional view of the component; (b) performance, this method (solid lines), MMT(dashed lines).

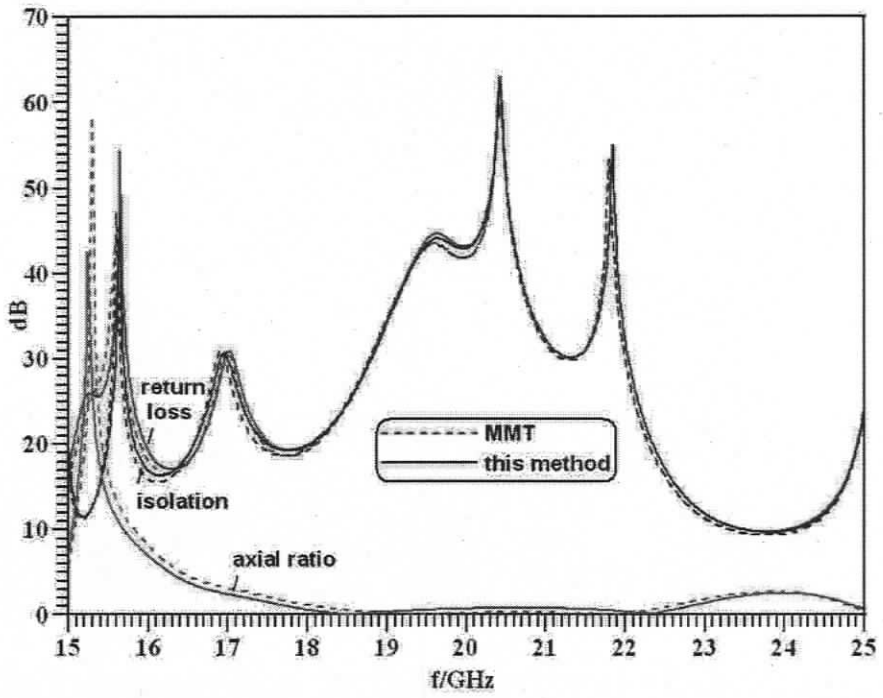

(b)

Fig. 5.6 cont'd.

5.3.3 Circular Waveguide Iris Filter

Similar to Section 4.xx for rectangular waveguides, the circular waveguide iris filter shown in Fig. 5.7a is used to demonstrate that the eigenvalue analysis correctly predicts the mode spectra of regular circular waveguides. The filter performance depicted in Fig. 5.7b was obtained by employing a single ridge of angular width of 360 degrees for the irises while all other possible ridges are set to zero. Excellent agreement is observed with results obtained from a CIET code and the μWave Wizard. As is well known, circular waveguide iris filters can be used as dual-polarization filters, due to their rotational symmetry, but they exhibit a rather poor stopband behavior towards higher frequencies.

For reference and comparison with the evanescent-mode filters presented in the following subsection, note that the radius of the empty circular waveguide is 6.5 mm and that the fundamental TE_{11} mode starts propagating at 13.5 GHz.

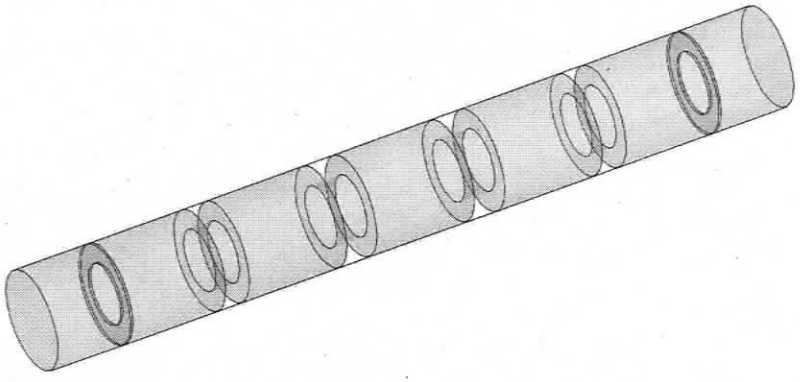

(a)

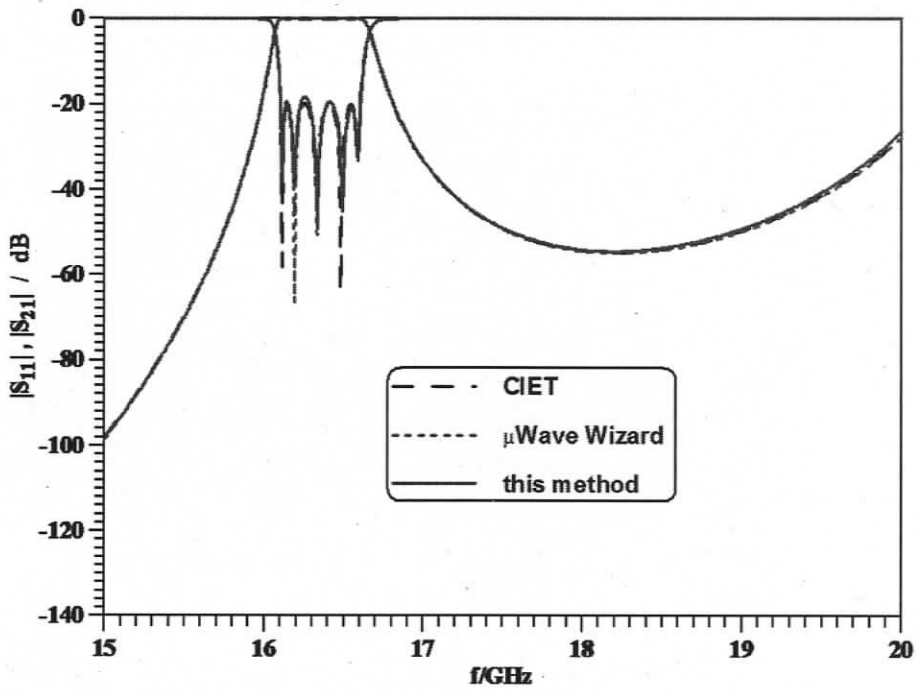

(b)

Fig. 5.7 Five-pole circular waveguide iris filter: (a) three-dimensional view; (b) performance, this method (solid lines), CIET (dashed lines), μWave Wizard (dashed lines).

5.3.4 Circular Ridged Waveguide Evanescent-Mode Filters

The lowering of the fundamental mode cutoff frequency in circular ridged waveguides can be used to fabricate filters with circular below-cutoff sections. Such filters have many attractive features like wide stopband characteristic, small component size and high skirt selectivity.

Evanescent-mode filters, sometimes also referred to as below-cutoff filters, are usually implemented by an abrupt transition from a larger to a smaller waveguide. The smaller waveguide is operated below cutoff but contains ridges which act as resonators by lowering the cutoff frequency of the smaller waveguide to approximately that of the larger waveguide. Another approach consists in utilizing the waveguide with ridges not only as resonators but also as input and output ports, thus assuming that a system be realized in a reduced-size, metal-ridged waveguide technology altogether. Such an approach has been used in Section 4.4.4 and is used here for the development of new circular waveguide evanescent-mode filters.

An evanescent-mode filter design in circular waveguide involves rigorous characterization of the discontinuities between individual sections. A ridged circular waveguide analysis based solely on the mode matching technique is presented in [44]. As will be shown, the eigenvalue mode-spectrum analysis allows for more general cross sections in circular ridged waveguide below-cutoff filters.

Fig. 5.8a presents a four-pole circular ridge waveguide filter, where the empty circular waveguide sections are used as coupling elements between the ridged waveguide resonators and input/output ports. The filter is designed for 500 MHz bandwidth, centered at 9.5 GHz and 20 dB return loss. For comparison with the circular waveguide iris filter of Fig. 5.7, the radius of the empty waveguide is maintained as 6.5 mm, but the filter is now operated at 9.5 GHz, which is below its fundamental-mode cutoff frequency of 13.5 GHz.

Very good agreement is observed in Fig. 5.8b between the MMT (dashed lines) and the method presented in this thesis (solid lines). Note that the cross section of the ridged circular waveguide is double-plane symmetric. This is the reason for it to be analyzable by the MMT. Moreover, it eliminates the excitation of asymmetric resonances and, therefore, the next passband occurs beyond 16 GHz. The cutoff frequency of the double-ridged input/output ports is 7.58 GHz.

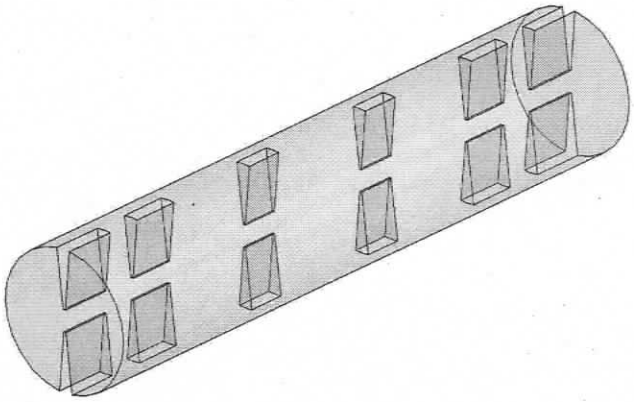

(a)

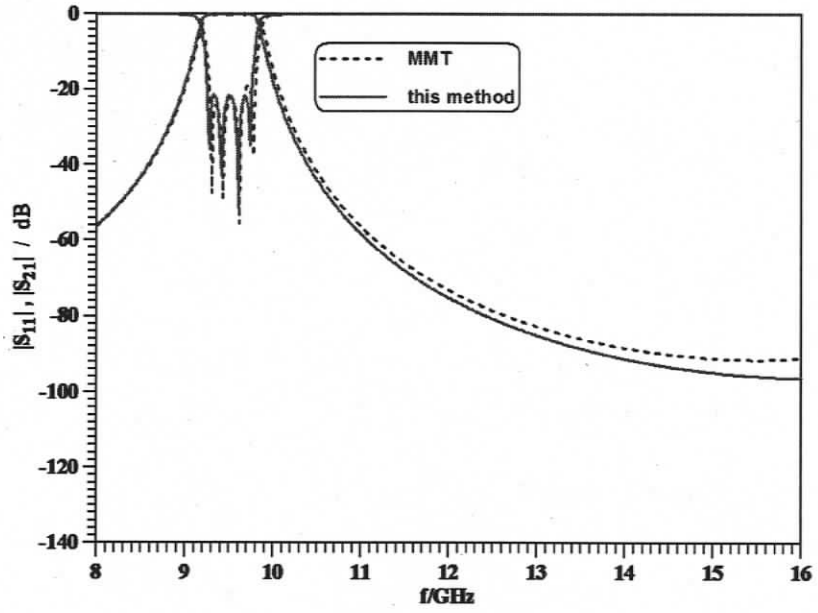

(b)

Fig. 5.8 Four-pole circular waveguide double-ridge evanescent-mode filter (a), performance and comparison with results obtained from the MMT (b).

A filter with the same specifications as that in Fig. 5.8, but with three ridges instead of two, is shown in Fig. 5.9a. The performance in Fig. 5.9b is very similar to that in Fig. 5.8b as far as the passband is concerned. The behavior towards higher frequencies is different, though. This is due to the fact that the cross section is reduced to single-plane symmetry which is responsible for the second passband peak appearing at around 15 GHz in Fig. 5.9b. In comparison with the double-ridge filter, the cutoff frequency of the triple-ridged ports is 7.86 GHz.

The concept is continued with the quadruple-ridge filter in Fig. 5.10a. Note that two-plane symmetry in the cross section is restored and, therefore, the passband peak around 15 GHz, which is caused by asymmetric modes in Fig. 5.9b, disappears in the performance of the quadruple-ridge filter in Fig. 5.10b. The cutoff frequency of the input/out put ports is 7.76 GHz.

In order to reduce the center frequency of the filter, the distance between ridges, currently at 2 mm or 0.15 times the dimension of the housing, must be further reduced. However, this is not advisable from a practical point of view since the field concentration around the tips of the ridges would increase tremendously, thus resulting in increased losses.

A possible alternative is found by reshaping the ridges. Fig. 5.11a shows a circular T-septum below-cutoff filter designed for a midband frequency of 8.76 GHz. The cutoff frequency of the input/output ports is 7.52 GHz. Although the cross section is only single-plane symmetric, which is associated with the inevitable excitation of asymmetric modes, the midband frequency of the filter (cf. Fig. 5.11b) is reduced compared to that of the triple-ridge filter in Fig. 5.9b and, thus, the second passband peak is pushed upwards in frequency to appear at 15.8 GHz in Fig. 5.11b. Similar behavior is observed in [45] for the rectangular-waveguide evanescent-mode filters.

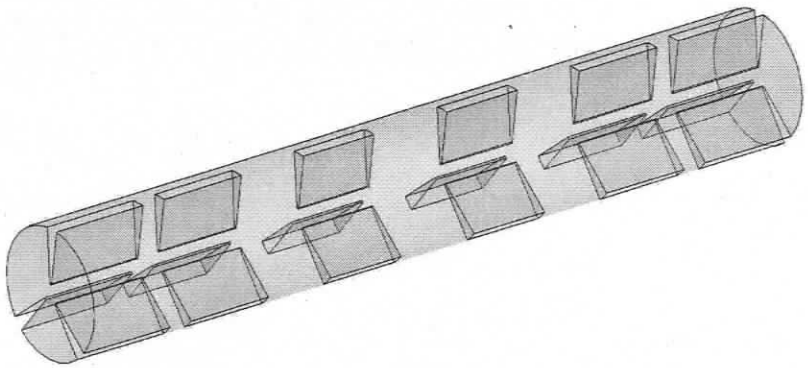

(a)

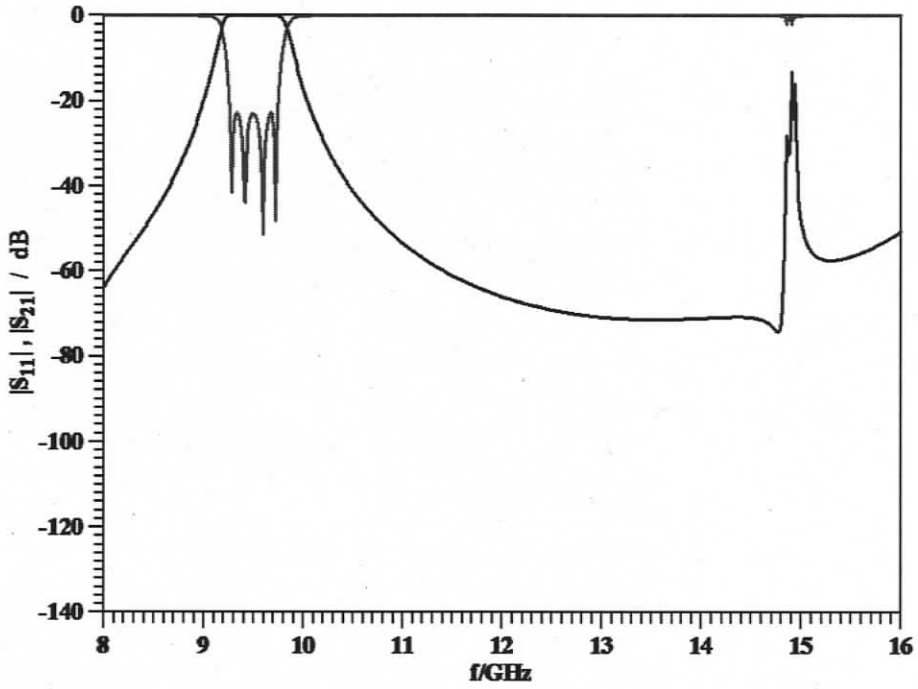

(b)

Fig. 5.9 Four-pole circular waveguide triple-ridge evanescent-mode filter (a) and performance (b).

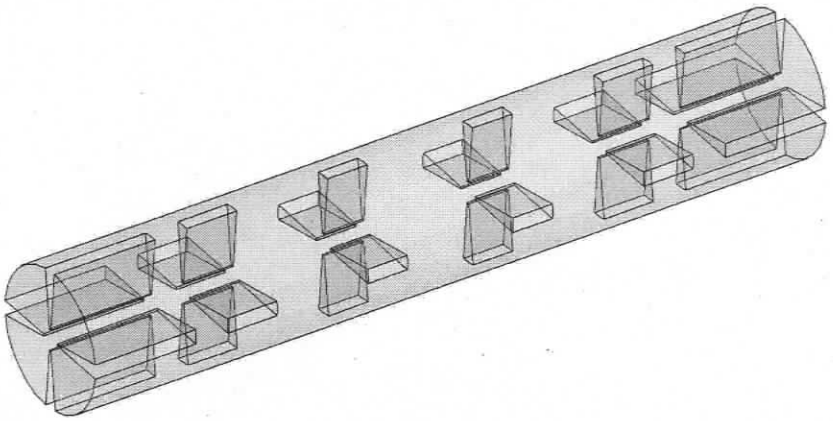

(a)

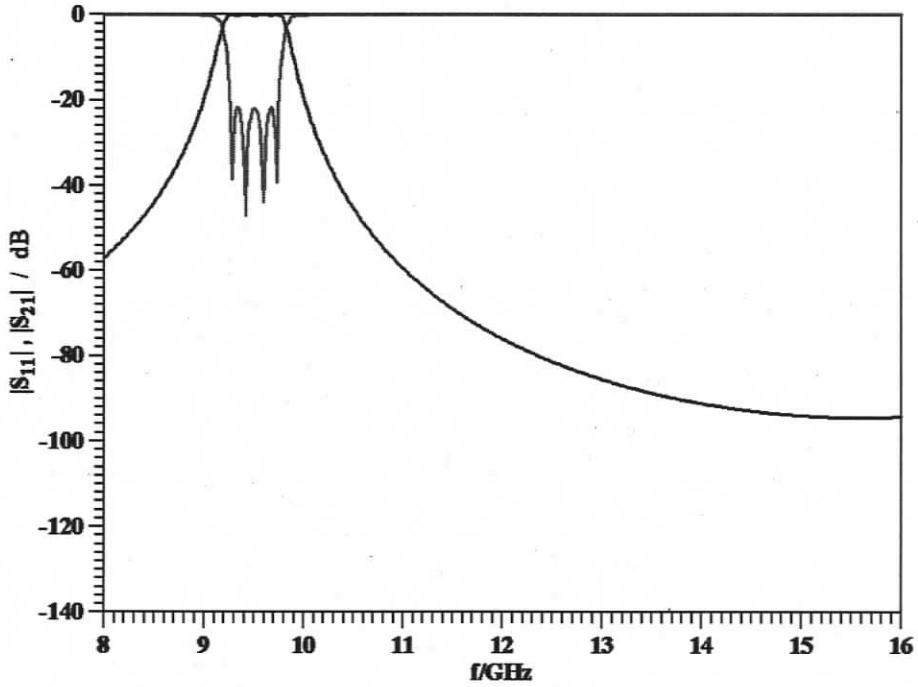

(b)

Fig. 5.10 Four-pole circular waveguide quadruple-ridge evanescent-mode filter (a) and performance (b).

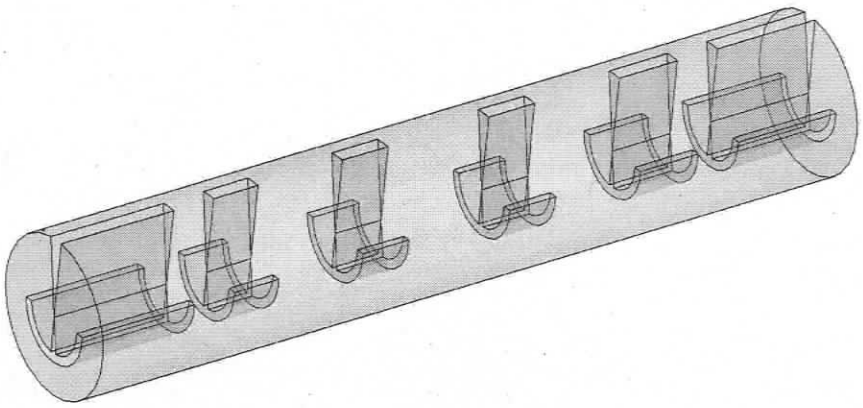

(a)

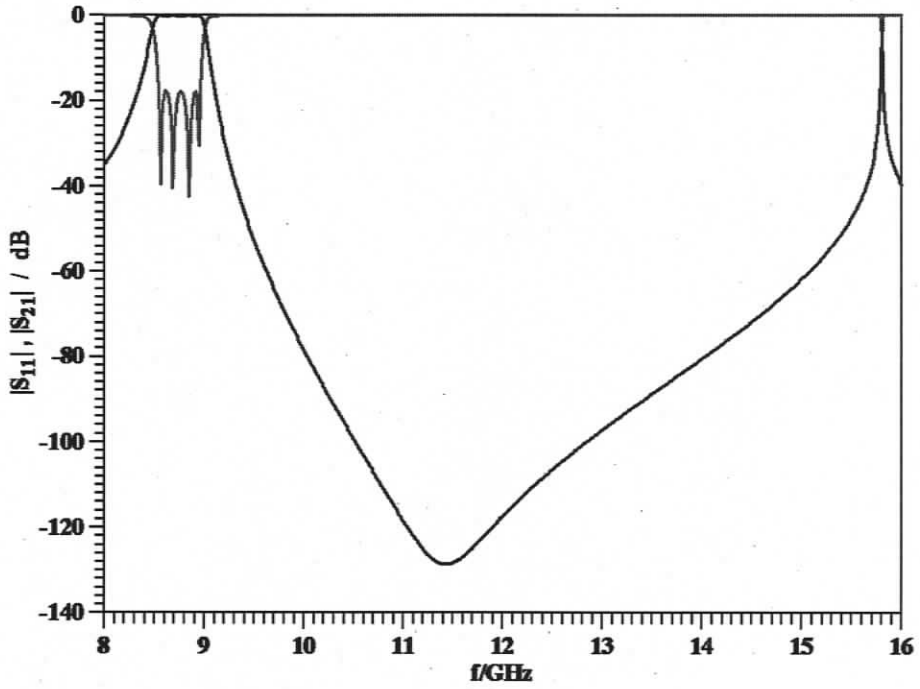

(b)

Fig. 5.11 Four-pole circular waveguide T-septum evanescent-mode filter (a) and performance (b).

A further reduction in cutoff frequency is only possible by increasing the angle of the bar of the circular T-septum. This leads to the development of the key-shaped ridged structure as shown in the Fig. 5.12a. Its cutoff frequency is 6.83 GHz, and the filter is designed for 440 MHz bandwidth at 8.5 GHz and 25 dB return loss. The housing dimensions are maintained at a radius of 6.5 mm. Since the midband frequency is further reduced compared to that of Fig. 11, the second passband peak is moved further upward in frequency and appears now beyond 16 GHz. Moreover, the frequency of minimum transmission is moved from 11.5 GHz in Fig. 11b to 15 GHz in Fig. 5.12b. It is interesting to note that the mode spectrum obtained for the key-shaped cross section includes the well-known solutions for the smaller circular waveguide. Thus the formulation in circular coordinates provides also solutions for standard circular waveguides which appear as part of the arbitrary placement of the ridges in circular waveguide.

Finally, an evanescent-mode filter, which maintains two-plane symmetry and avoids a too close placement of the tips of the ridges, in the double T-septum filter shown in Fig. 5.13a. The midband frequency is at 7. 125 GHz and the cutoff frequency of the input/output ports is 5.99 GHz. The performance as displayed in Fig. 5.13b shows excellent stopband performance with a second passband beyond 18 GHz. The angular width of the T-septum bars is 90 degrees, and the minimum distance between the ridges is 1.41 mm. Hence, compared to the double-ridge filter of Fig. 5.8, the distance between the ridges is not only increased, but the maximum field concentration for the same power transfer is divided between two locations of proximity of the ridges. Whereas this is an improvement over the filter in Fig. 5.8, it is expected, based on measurements conducted in [67], that the passband insertion losses will amount to 2 - 3 dB. (It is noted that the theoretical treatment in this work does not include losses nor the possibility of evaluating current distributions due to high field concentrations of sharp edges.)

In comparing the cross sections of this section with those that have been treated with an all-MMT approach, we find that the solutions of structures such as displayed in Fig. 5.9 to Fig. 5.13 have never been attempted with an entirely MMT-based approach. Hence the

eigenvalue mode-spectrum technique provides opportunities for the design of new circuits and components.

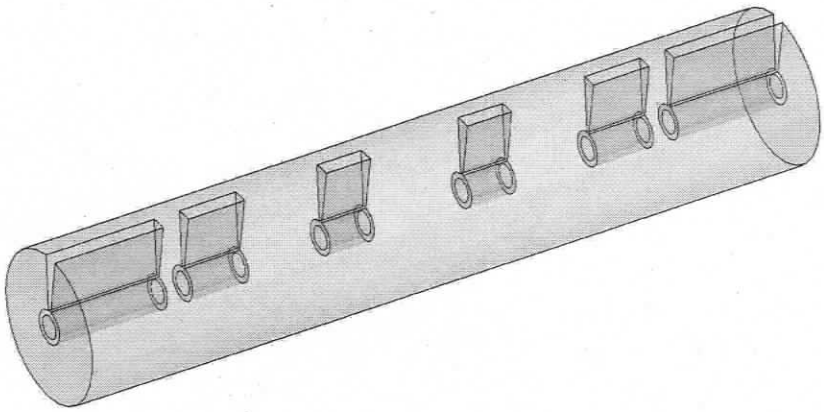

(a)

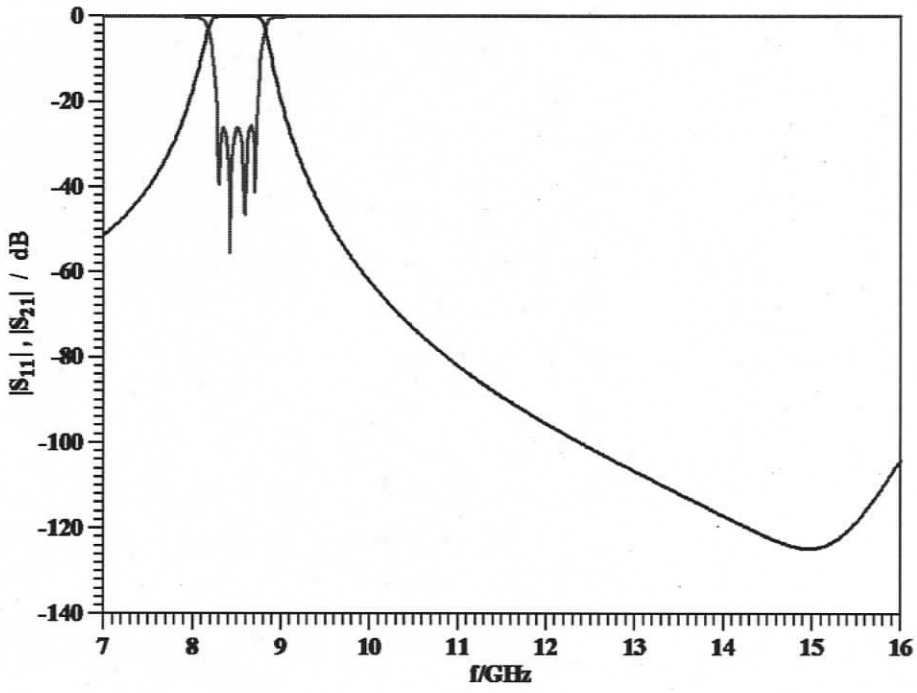

(b)

Fig. 5.12 Four-pole circular waveguide key-shaped evanescent-mode filter (a) and performance (b).

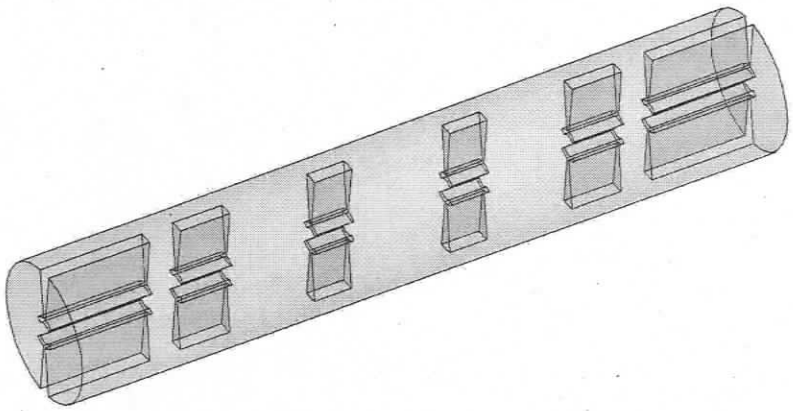

(a)

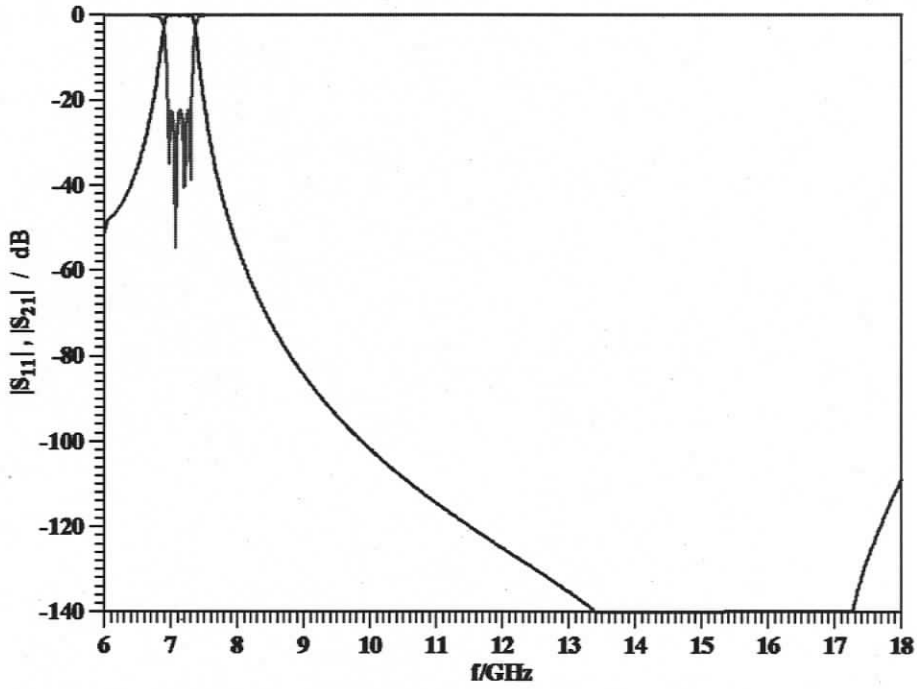

(b)

Fig. 5.13 Four-pole circular waveguide double T-septum evanescent-mode filter (a) and performance (b).

5.3.4 Polarization Rotator

A polarization rotator represents a key element in the realization of polarization dependent microwave components and systems. A circular polarization rotator rotates a linearly polarized incident wave as it propagates through the component. The basic concept of operation is similar to that of [66] where a linearly polarized wave is captured between two ridges while the shape of the waveguide housing changes. For the polarization rotator, we maintain the circular waveguide housing but once the wave has been captured between two ridges, the ridges are stepwise rotated to change the direction of the wave's linear polarization. Fig. 14a shows a three-dimensional view of the polarization rotator. Note that the first two sections at the input and output serve the purpose of transforming the TE_{11} mode of the empty circular waveguide to the TE_1 mode between the ridges.

The design is similar to the fine optimization of waveguide filters (cf. section 4.4.6). However, since modes with different polarization are involved, we refrain from enforcing a stopband but focus rather on an acceptable performance over a specific bandwidth.

The following cost function is used in the optimization

$$\text{error function} = \sum_i \frac{\text{RL\_goal}(f_i)}{\text{RL}_{(\text{VP}\rightarrow\text{VP})}(f_i)} + \sum_i \frac{\text{RL\_goal}(f_i)}{\text{RL}_{(\text{VP}\rightarrow HP)}(f_i)} + \sum_i \frac{\text{IL\_goal}(f_i)}{\text{IL}_{(\text{VP}\rightarrow\text{VP})}(f_i)} + 3\sum_i \frac{\text{IL\_goal}(f_i)}{\text{IL}_{(\text{VP}\rightarrow HP)}(f_i)} \tag{5.15}$$

where $RL\_goal(f_i)$, $IL\_goal(f_i)$ are the desired return loss and insertion loss, and $RL_{(VP\rightarrow VP)}(f_i)$, $RL_{(VP\rightarrow HP)}(f_i)$, $IL_{(VP\rightarrow VP)}(f_i)$, the actual return loss and insertion loss at frequencies f_i , respectively. Note that the fourth item in (5.15) denotes the conversion from vertical (VP) to horizontal polarization (HP).

Fig. 14b shows the results of such an optimization for a frequency range of 17.5 GHz to 20 GHz. The rotation angles between individual sections are assumed constant and all initial section lengths are set to a quarterwavelength at midband frequency. For the given

frequency range, the component suppresses all unwanted polarizations by 15 dB and lets pass only the rotated incoming polarization.

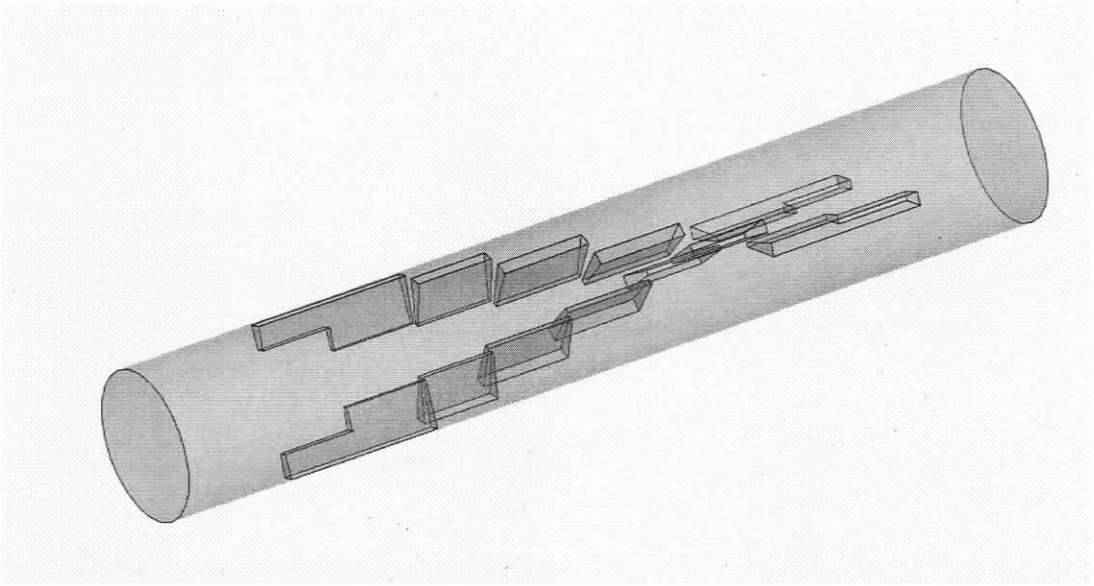

(a)

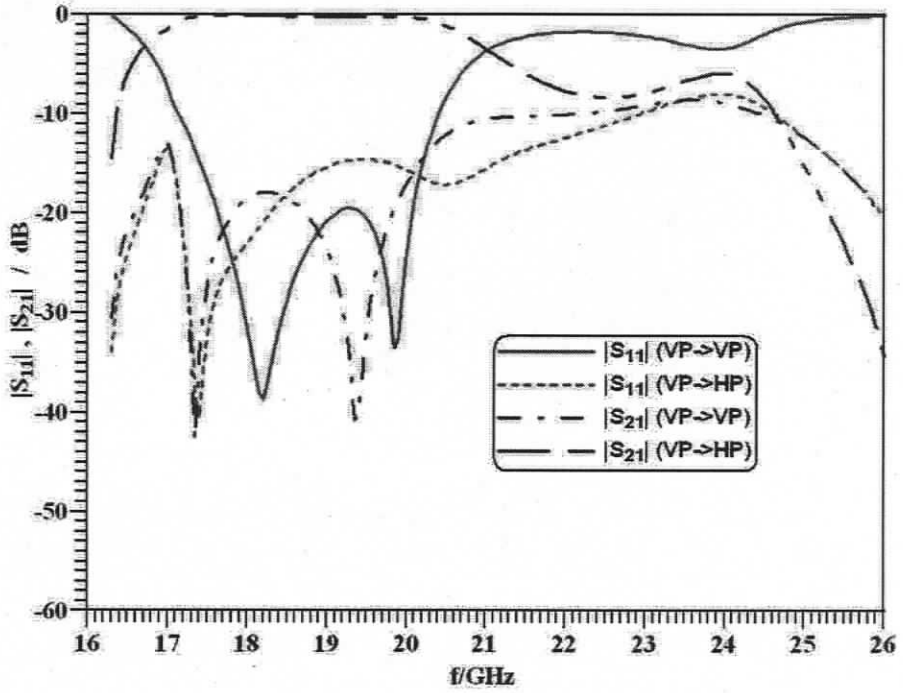

(b)

Fig. 5.14 Eight-section circular waveguide polarization rotator (a) and performance (b).

5.4 Conclusion

The mathematical approach described for multi-ridged rectangular waveguides was extended to multi-ridged circular waveguides in this Chapter. The double-ridged circular waveguide was first introduced and served as the core building block of circular waveguide components. An eigenvalue mode-spectrum analysis involving Bessel functions was then formulated. A convergence analysis shows good agreement with results obtained by MMT techniques. The complete analysis and design procedures were finalized using the generalized S-matrix method. To demonstrate the validity of the approach, a circular ridged waveguide polarizer and below-cutoff circular ridge waveguide filters have been designed. Excellent agreement of the S-parameters with results from the MMT was presented. Moreover, a number of new types of circular waveguide components, such as below-cutoff circular single and double T-septum waveguide filters, below-cutoff triple- and quadruple-ridge filters, below-cutoff circular key-shaped ridged waveguide filters, and a polarization rotator, were presented to show the algorithm's applicability and versatility.

Chapter 6 CONCLUSIONS AND RECOMMENDATIONS

6.1 Conclusion

The major objective of this research has been to provide a contribution to the development of accurate computer-aided analysis and design of microwave components constructed in nonstandard waveguide technology for microwave and satellite communication systems. The eigenvalue mode-spectrum analysis in conjunction with the mode-matching technique accomplishes the goal of extending accurate numerical design, due to its flexibility and applicability of the formulations resulting from such an approach, to a wide range of other waveguide technologies. Significant throughout the work and central to its methodology is to predict a full-wave mode-spectrum of the structure in one step, and then construct a generalized scattering matrix of discontinuities, which eventually leads to complete component designs. Here, the emphasis has been on the mathematical description of the cross section and discontinuity in question rather than on the components as a whole. The basic framework for the eigenvalue approach has been established and was later extended to irregular waveguide components.

The most commonly used numerical techniques in microwave systems were presented as well as a survey of techniques for nonstandard waveguide analysis. From the methods available to rigorously solve electromagnetic field problems with respect to advantages and disadvantages, the mode matching technique has been found to be best suited for the design of waveguide components in the frequency domain.

The standard mode-matching technique was presented as a critical numerical method for the cross-section analysis. However, this technique has less flexibility to deal with arbitrary discontinuities in waveguide's cross sections. A classical eigenvalue approach was therefore employed to handle irregular waveguide cross sections. The theoretical treatment of the single ridged waveguide forms a powerful tool for the computer-aided design of irregular waveguide structures. With the introduction of the new concept of a constraint function applied to TM modes, the proposed eigenvalue mode-spectrum

analysis demonstrates the ability of handling arbitrary cross-section structures in regular waveguides; of simplifying the numerical calculations of power factors and coupling matrices; and of cooperating with existing mode-matching routines in three-dimensional analysis. Close agreement between our theoretical data and HFSS simulated results was obtained for the propagation characteristics of the single ridged cross-section waveguide, as well as a simple empty-ridged-empty waveguide structure. Having calculated these characteristics and coupling matrices, this eigenvalue mode-spectrum approach together with the mode-matching technique was then applied to multiple-ridged rectangular and circular waveguide structures.

The proposed fundamental formulations were expanded to include the theoretical and numerical analysis of nonstandard multi-ridged waveguide structures. Upon the validation of convergence of the multiple-ridged waveguide solutions, the design of waveguide filters, waveguide transformers, below-cutoff waveguide filters, and a 90-degree waveguide twist component were presented. Through the incorporation of higher-order mode interactions, the proposed model provides design data that are in close agreement with experimental results or other numerical simulations.

The eigenvalue mode-spectrum analysis involving Bessel functions in the cylindrical coordinate system has been discussed for multiple ridged circular waveguides. The circular-to-multi-ridged circular waveguide discontinuity serves as a basic building block element in circular waveguide technology, and a set of complete formulations were developed to determine the full-wave scattering matrices. Having characterized discontinuities in ridged circular waveguides, the analysis was applied to the design of certain useful components. Based on the proposed numerical analysis methodology, a circular ridged waveguide polarizer and below-cutoff circular ridged waveguide filters have been designed. The performance of these components is compared with other numerical field solvers, and the results are in very close agreement. Subsequent to this approach, a polarization rotator was introduced as another design application.

The results presented in this thesis show a significant step forward in the direction of rigorous computer-aided design of components both in rectangular and circular waveguide technology. The foundation has been set, and future work could benefit from the theoretical approach proposed in the thesis.

6.2 Recommendations

The eigenvalue mode-spectrum analysis combined with the mode-matching technique presents rigorous and complete solutions for components in irregular waveguide technology. It is obvious that the developed mathematical formulations are to facilitate the computer-aided design process. Hence, the numerical algorithms can be extended to cover a wide range of related waveguide component design problems.

The first objective for future work is to apply the numerical method to integrated waveguide diplexers and multiplexers. This can be accomplished by solving the building block discontinuities of waveguide junctions, main waveguide filters and branch waveguide filters. The scattering matrix of the overall component is calculated by the combination of the individual sub-scattering matrices of these basic discontinuities within the components. The eigenvalue mode-spectrum analysis serves as a fundamental tool to predict the propagation characteristics while the mode-matching technique generates the scattering matrices. In this context, a more efficient and more accurate calculation of the gradient during optimization is recommended. This can be accomplished by using adjoint networks [74].

A second recommendation is the expansion of the theoretical and numerical analysis from nonstandard cross sections in the two-port waveguide junction to multi-port junctions with nonstandard regions. Multi-port junctions with a discontinuity-distorted resonator region, such as in waveguide bends, power dividers, and orthomode transducers, find important applications in many microwave circuits for modern communication systems. Various investigations and approaches [67]-[69] have been performed with less accuracy or limited flexibility to handle complex structures. In general, to establish the formulation for determining the generalized scattering matrix, a

rigorous field theory treatment of the discontinuities within the resonator region and the complete mode-matching conditions at the multi-junction waveguide apertures must be set up. The eigenvalue mode-spectrum analysis is capable of predicting the characteristic features of the discontinuities. Since the discontinuities within the resonator regions are rigorously taken into account and their influences are transformed to the apertures of the junction, the generalized scattering matrix can be calculated by the mode-matching technique.

Another area for further research might be to explore new waveguide technologies, such as elliptic waveguides for improved filter stopband characteristics, coaxial ridged circular waveguides (including TEM-mode propagation) as alternative application in the lower gigahertz frequency, and a plus shaped guide as an alternative to the rectangular iris. In short, a wide range of irregular waveguide component designs is possible as an extension to the approaches discussed in this work.

Bibliography

[1] G. Mar, "Finite difference method for the solution of electromagnetic waveguide discontinuity problem," *IEEE Trans. Microwave Theory Tech.*, Vol. 22, pp. 54-57, Jan. 1974.

[2] H.E. Green, "The numerical solution of some important transmission-line problems," *IEEE Trans. Microwave Theory Tech.*, Vol. 13, pp. 676-692, Sep. 1965.

[3] P. Silvester, *Finite Elements for Electrical Engineers*, Combridge University Press, New York, 1983.

[4] R.F. Harrington, *Field Computation by Moment Methods*, R.E. Krieger, Mrieger, Malabar, Fl., 1987.

[5] T.S. Chu, T. Itoh, and Y.-C. Shih, "Comparative study of mode-matching formulations for microstrip discontinuity problems," *IEEE Trans. Microwave Theory Tech.*, Vol. 33, pp. 1018-1023, Oct. 1985.

[6] J. Uher, J. Bornemann, and U. Rosenberg, *Waveguide Components for Antenna Feed Systems: Theory and CAD*, Artech House, Norwood, 1993.

[7] R. Mittra and J. Pace, "A new technique for solving a class of boundary value problem," Antenna Laboratory, University of Illinois, Urbana, Rep. 72, 1963

[8] A.S. Omar and K. Schünemann, "Analysis of waveguides with metal inserts," *IEEE Trans. Microwave Theory Tech.*, Vol. 37, pp. 1924-1932, Dec. 1989.

[9] S.-L. Lin, L.-W. Li, T.-S. Yeo, and M.-S. Leong, "Analysis of metallic waveguides of a large class of cross sections using polynomial approximation," *IEEE Trans. Microwave Theory Tech.,* Vol. 46, pp. 1136-1139 June. 2001.

[10] B.E. Spielman and R.F. Harrington, "Waveguide of arbitrary shaped regular waveguides by the method of auxiliary sources," *Radio Eng. Elec. Phys.*, Vol. 27, pp. 56-60, June 1982.

[11] G. Conciauro, M. Bressan, and C. Zuffada, "Waveguide modes via an intergral equation leading to a linear matrix eigenvalue problem," *IEEE Trans. Microwave Theory Tech.*, Vol. 32, pp. 1495-1504, Nov. 1984.

[12] G.D. Smith, *Numerical Solution of Partical Differential Equations: Finite Difference Methods* (Third Edition), Oxford University Press, Oxford, 1985.

[13] J.C. Strikwerda, *Finite Difference Schemes and Partical Differential Equations*, Wadsworth & Brooks, Belmont, CA, 1989.

[14] K.S. Yee, "Numerical solution of initial boundary value problems inVolving Maxwell's equation in isotropic media," *IEEE Trans. Antennas Propat,* Vol. 14, pp. 302-307, 1966.

[15] A. Taflove and S. Hagness, Computational Electrodynamics: The Finite-Difference Time-Domain Method, 3rd ed., Artech House, Norwood, 2005.

[16] P. Silvester and A.J. Davies, *The Finite Elements Method: A First Approach*, Oxford University Press, Oxford, 1980.

[17] P. P. M. So, Eswarappa, and W.J.R. Hoefer, "A two-dimensional transmission line matrix microwave field simulator using new concepts and procedures," *IEEE Trans. Microwave Theory Tech.*, Vol. 37, pp. 1877-1884, Dec. 1989.

[18] P. B. Johns, "A symmetrical condensed node for the TLM method," *IEEE Trans. Microwave Theory Tech.*, Vol. 35, pp. 370-377, Apr. 1987.

[19] T. Itoh and R. Mittra, "Spectral-domain approach for calculating the dispersion characteristics of microstrip lines," *IEEE Trans. Microwave Theory Tech.*, Vol. 21, pp. 496-499, July 1973.

[20] D.S. Jones, *The Theory of Electromagnetism*, Pergamon, New York, 1964.

[21] R. Sorrentino, *Numerical Methods of Passive Microwave and Millimeter-Wave Structures*, IEEE Press, New York, 1989, ch. 8.

[22] A. Wexler, "Solution of waveguide discontinuities by modal analysis," *IEEE Trans. Microwave Theory Tech.*, Vol. 15, pp. 508-517, Sep. 1967.

[23] S.B. Cohn, "Properties of ridge wave guide", *Proc. IRE*, Vol. 35, pp. 783-788, Aug. 1947.

[24] S. Hopfer, "The design of ridged waveguides," *IRE Trans. Microwave Theory Tech*, Vol. 3, pp. 20-29, Oct.1955.

[25] M.J. Beaubien and A. Wexler, "An accurate finite-difference method for higher order waveguide modes," *IEEE Trans. Microwave Theory Tech.*, Vol. 16, pp. 1007-1017, Dec. 1968.

[26] J.P. Montgomery, "On the complete eigenvalue solution of ridged waveguide," *IEEE Trans. Microwave Theory Tech.*, Vol. 19, pp. 547-555, June 1971.

[27] Y.H. Cho and H.J. Eom, "Analysis of a ridge waveguide using overlapping T-blocks", IEEE Trans. Microwave Theory Tech., Vol. 50, pp. 2368-2373, Oct. 2002.

[28] N. Boukli-Hacene, J. Sombrin, and A. Papiernik, "Approximation by Geigenbauer polynomials in the study of a rectangular ridged waveguide. Application to the analysis of a waveguide septum polarizer", Int. J. Numer. Model., Vol. 16, pp. 299–318, July/Aug. 2003.

[29] M. Swaminathan, E. Arvas, T.K. Sakar, and A.R. Djordjevic, "Computation of cutoff wave numbers of TE and TM modes in waveguides of arbitrary cross sections using a surface integral formulation," *IEEE Trans. Microwave Theory Tech.*, Vol. 38, pp. 154-159, Feb. 1990.

[30] J. Bornemann and F. Arndt, "Transverse resonance, standing wave, and resonator formulations of the ridge waveguide eigenvalue problem and its application to the design of E-plane finned waveguide filters," *IEEE Trans. Microwave Theory Tech.*, Vol. 38, pp. 1104-1113, Aug. 1990.

[31] W. Sun and C.A. Balanis, "MFIE analysis and design of ridged waveguides," *IEEE Trans. Microwave Theory Tech.*, Vol. 41, pp. 1965-1971, Nov. 1993.

[32] R. Beyer and F. Arndt, "Efficient modal analysis of waveguide filters including the orthogonal mode coupling elements by an MM/FE method," *IEEE Microwave Guided Wave Lett.,* Vol. 5, pp. 9-11, Jan. 1995.

[33] M. Balagangadhar, T.K. Sarkar, J. Rejeb, and R.R. Boix, "Solution of the general Helmholtz equation in homogeneously filled waveguides using a static Green's function," *IEEE Trans. Microwave Theory Tech.*, Vol. 46, pp. 302-307, Sep. 1997.

[34] W. Schroeder and I. Wolff, "A reliable and efficient numerical method for indirect eigenvalue problems arising in waveguide and resonator analysis," *Int. J. Numer. Model.*, Vol. 12 pp. 197-208, May-June 1999.

[35] J. Bornemann, "Comparison between different formulations of the transverse resonance field-matching techniques for the three-dimensional analysis of metal-finned waveguide resonators," *Int. J. Numer. Model.* Vol. 4, pp. 63-73, 1991.

[36] V. Crino, C. Tomassoni, and M. Mongiardo, "Line-integral formulation of the hybrid MM/FEM technique", *IEEE MTT-S Int. Microwave Symp. Dig.*, pp. 2033 - 2036, Seattle, USA, June 2002.

[37] Y. Zhan and W. Joines, "Some properties of T-septum waveguides," *IEEE Trans. Microwave Theory Tech.*, Vol. 35, pp. 769-775, Aug. 1987.

[38] B.E. Pauplis and D.C. Power, "On the bandwidth of T-septum waveguide," *IEEE Trans. Microwave Theory Tech.*, Vol. 31, pp. 919-922, Aug. 1989.

[39] S. Amari and J. Bornemann, "A pole-free modal field-matching technique for eigenvalue problems in electromagnetics," *IEEE Trans. Microwave Theory Tech.*, Vol. 45, pp. 1649-1653, Sep. 1997.

[40] S. Amari and J. Bornemann, "Application of a pole-free modal field-matching technique to ridged rectangular waveguide," *Microwave Opt. Technol. Lett.,* Vol. 14, pp. 337-340, Apr. 1997.

[41] W. Schroeder and I. Wolff, "The origin of spurious modes in numerical solutions of electromagnetic field eigenvalue problems," *IEEE Trans. Microwave Theory Tech.*, Vol. 42, pp. 644-653, Apr. 1994.

[42] V.A. Labay and J. Bornemann, "Matrix singular value decomposition for pole-free solutions of homogeneous matrix equations as applied to numerical modeling methods," *IEEE Microwave Guided Wave Lett.,* Vol. 2, pp. 49-51, Feb. 1992.

[43] S. Amari and J. Bornemann, "A technique to locate minima in singular-value decomposition for eigenvalue problems in electromagnetics," *Microwave Opt. Technol. Lett.,* Vol. 14, pp. 318-321, Apr. 1997.

[44] J. Bornemann, S. Amari, J. Uher, and R. Vahldieck, "Analysis and design of circular ridged waveguide components," *IEEE Trans. Microwave Theory Tech.*, Vol. 47, pp. 330-335, Mar. 1999.

[45] V.A. Labay, J. Bornemann, S. Amari, and J. Damaschke, "Direct-coupled waveguide filters for the lower gigahertz frequency range," *Int. J. RF Microwave CAE,* Vol. 12, pp. 217-225, Mar. 2002.

[46] V.A. Labay and J. Bornemann, "Broadband rectangular-to-ridge-to-T-septum waveguide transformers," *Microwave Opt. Technol. Lett.,* Vol. 43, pp. 183-185, Nov. 2004.

[47] A.S. Omar and K.F. Schünemann, "Applications of the generalized spectral-domain technique to the analysis of rectangular waveguides with rectangular and circular metal inserts," *IEEE Trans. Microwave Theory Tech.*, Vol. 39, pp. 944-952, June 1999.

[48] S.-L. Lin, L.-W. Li, T.-S. Yeo, and M.-S. Leong, "Cutoff wavenumbers in truncated waveguides", *IEEE Microwave Wireless Comp. Lett.,* Vol 11, pp. 214-216, May 2001.

[49] S.-L. Lin, L.-W. Li, T.-S. Yeo, and M.-S. Leong, "Analysis of metallic waveguides of a large class of cross sections using polynomial approximation and superquadratic functions", *IEEE Trans. Microwave Theory Tech.,* Vol. 49, pp. 1136-1139, June 2001.

[50] S.-L. Lin, L.-W. Li, T.S. Yeo, and M.S. Leong, "Novel modified mode matching analysis of concentric waveguide junctions", *IEE Proc.-Microw. Antennas Propag.,* Vol. 148, pp. 369-374, Dec. 2001.

[51] L.-W. Li, S.-L. Lin, T.-S. Yeo and M.-S. Leong, "Modal analysis of waveguides and efficient CAD of waveguide junctions using a unified method", *Proc. Asia-Pacific Microwave Conf.,* pp. 433-436, Taipei, Taiwan, Dec. 2001.

[52] M. Mongiardo and R. Sqrrentino, "Efficient and versatile analysis of microwave structures by combined mode matching and finite difference methods," *IEEE Microwave Guide Wave Lett.*, Vol. 3, pp. 241-243, Aug. 1993.

[53] V.A. Labay and J. Bornemann, "Singular value decomposition improves accuracy and reliability of T-septum waveguide field-matching analysis", *Int. J. Microwave Millimeter-Wave CAE*, Vol. 2, pp. 82-89, Apr. 1992.

[54] R.A. Horn and C.A. Johnson, *Matrix Analysis*. Cambridge University Press, New York, 1985.

[55] D. Guha and P. K. Saha, "Some Characteristics of ridge-trough waveguide," *IEEE Trans. Microwave Theory Tech.*, Vol. 45, pp. 449-453, Mar. 1997.

[56] J.J.H. Wang, *Generalized Moment Methods in Electromagnetics*. John Wiley & Sons, New York, 1992.

[57] J. Bornemann and F. Arndt, "Modal-S-matrix design of optimum stepped ridged and finned waveguide transformers," *IEEE Trans. Microwave Theory Tech.*, Vol. 35, pp. 561-567, June 1987.

[58] W. Sun and C.A. Balanis, "Analysis and design of quadruple-ridged waveguides," *IEEE Trans. Microwave Theory Tech.*, Vol. 42, pp. 2201-2207, Dec. 1994.

[59] P.K. Saha and D. Guha, "New broadband rectangular waveguide with L-shaped septa," *IEEE Trans. Microwave Theory Tech.*, Vol. 40, pp. 777-781, Apr. 1992.

[60] H. Asao, G. Hiraiwa, and A. Katayama, "A compact 90-degree twist using novel ridged waveguide for integrated waveguide subsystems," *Proc. 36th European Microwave Conf.*, pp. 1185-1188, Manchester, UK, Sep. 2006.

[61] G.L. Matthaei, L. Young, E.M.T. Jones, *Microwave Filters, Impedance Matching Networks and Coupling Structures*, New York: McGraw-Hill, 1964.

[62] S. Amari, J. Bornemann, and R. Vahldieck, "A technique for designing ring and rod dielectric resonators in cutoff waveguides," *Microwave Opt. Technol. Lett.*, Vol. 23, No. 4, pp. 203-205, Nov. 1999.

[63] K. Madsen, H. Schaer-Jacobsen, and J. Voldby, "Automated minimax design of networks," *IEEE Trans. Circuits Systems*, Vol. 22, pp. 791-796, Oct. 1975.

[64] B.T. Smith, J.M. Boyle, J.J. Dongarra, B.S. Garbow, Y. Ikebe, V.C. Klema, and C.B. Moler, Matrix Eigensystem Routines - EISPACK Guide, Lecture Notes in Computer Science, Vol. 6, 2nd Ed., Springer-Verlag, Berlin, 1976.

[65] W.A. Press, S.A. Teukolsky, W.T. Vetterling, and B.P. Flannery, *Numerical Recipes in Fortran 90: The Art of Parallel Scientific Computing*, Cambridge U. Press, Cambridge 1996.

[66] J. Huang, R. Vahldieck and H. Jin, "Frequency-domain TLM analysis of the transition from rectangular to circular waveguide," *IEEE MTT-S Int. Microwave Symp. Dig.*, pp. 705-708, Seattle, USA, June 1994.

[67] V.A. Labay and J. Bornemann, "CAD of T-septum waveguide evanescent-mode filters," *IEEE Trans. Microwave Theory Tech.*, Vol. 41, pp. 731-733, Apr. 1993.

[68] F. Alessandri, M. Mongiardo and R. Sorrentino, "Computer-aided design of beam forming networks for modern satellite antennas," *IEEE Trans. Microwave Theory Tech.*, Vol. 40, pp. 1117-1127, June. 1992.

[69] X-P. Liang, K.A. Zaki, and A.E. Atia, "A rigorous three plane mode-matching technique for characterizing waveguide T-junction, and its application in multiplexer design," *IEEE Trans. Microwave Theory Tech.*, Vol. 39, pp. 2138-2147, Dec. 1991.

[70] A. Labay and J. Bornemann, "Generalized modal scattering matrix of discontinuity-distorted waveguide multiport junctions," *J. Numer. Model*, Vol. 4, pp. 63-73, 1991.

[71] K.-L. Wu, R.R. Mansour, and H. Wang, "A full wave analysis of a conductor post insert reentrant coaxial resonator in rectangular waveguide combline filters," *IEEE MTT-S Int. Microwave Symp. Dig.*, pp. 1639-1642, San Francisco, USA, June 1996.

[72] B.L. Ooi and G. Zhao, "Element-free method for the analysis of arbitrarily shaped hollow conducting waveguides," *IEE Proc.-Microw. Antennas Propag.*, Vol. 152, pp. 31-34, Feb. 2005.

[73] U. Rosenberg, J. Ebinger, and S. Amari, "Advanced receive/transmit diplexer design for emerging mm-wave access radio applications," *IEEE MTT-S Int. Microwave Symp. Dig.*, pp. 1217-1220, San Francisco, USA, June 2006.

[74] F. Alessandri, M. Dionigi, and R. Sorrentino, "A fullwave CAD tool for waveguide components using a high speed direct optimizer," *IEEE Trans. Microwave Theory Tech.*, Vol. 43, pp. 2046-2052, Sep. 1995.

Appendix

Dimensions of Analyzed Structures

A.1 Rectangular Waveguide Structures

Please refer to Fig. 4.1 for ridge locations and cross section. All dimensions are in millimeters.

Fig. 3.4 and Fig. 3.9

19.0500 9.5250 ---------- width and height of ridged waveguide housing.

6.5250 5.0250 6.0000 4.5000 ---------- position (e_1,d_1), width (w_1), height (t_1).

length of waveguides:

20.0000

20.0000

20.0000

Fig. 4.6

15.8500 7.6250 ---------- width and height of ridged waveguide housing.

7.4750 5.3625 2.2625 0.9000 ---------- position (e_1,d_1), width (w_1), height (t_1).

7.4750 5.3625 2.2625 0.0000 ---------- position (e_2,d_2), width (w_2), height (t_2).

length of waveguides:

20.0000

2.6000

20.0000

Fig. 4.7

15.8500 7.6250 ---------- width and height of ridged waveguide housing.

7.4750 5.3625 2.2625 0.9000 ---------- position (e_1,d_1), width (w_1), height (t_1).

7.4750 5.3625 2.2625 0.0000 ---------- position (e_2,d_2), width (w_2), height (t_2).

length of waveguides:

20.0000

2.6000

10.2500

8.9500

10.5000

8.9500

10.2500

2.6000

20.0000

Fig. 4.8

15.7990 7.8990 ---------- width and height of ridged waveguide housing.

7.3995 7.2825 1.0000 0.6145 --------- position (e_{11},d_{11}), width (w_{11}), height (t_{11}).

7.3995 0.0000 1.0000 0.6145 --------- position (e_{12},d_{12}), width (w_{12}), height (t_{12}).

7.3995 6.6095 1.0000 1.2895 --------- position (e_{21},d_{21}), width (w_{21}), height (t_{21}).

7.3995 0.0000 1.0000 1.2895 --------- position (e_{22},d_{22}), width (w_{22}), height (t_{22}).

7.3995 6.0945 1.0000 1.8045 --------- position (e_{31},d_{31}), width (w_{31}), height (t_{31}).

7.3995 0.0000 1.0000 1.8045 --------- position (e_{32},d_{32}), width (w_{32}), height (t_{32}).

7.3995 5.6195 1.0000 2.2795 --------- position (e_{41},d_{11}), width (w_{41}), height (t_{41}).

7.3995 0.0000 1.0000 2.2795 --------- position (e_{42},d_{12}), width (w_{42}), height (t_{42}).

7.3995 5.1695 1.0000 2.7295 --------- position (e_{51},d_{21}), width (w_{51}), height (t_{51}).

7.3995 0.0000 1.0000 2.7295 --------- position (e_{52},d_{22}), width (w_{52}), height (t_{52}).

7.3995 4.9495 1.0000 2.9495 --------- position (e_{61},d_{31}), width (w_{61}), height (t_{61}).

7.3995 0.0000 1.0000 2.9495 --------- position (e_{62},d_{32}), width (w_{62}), height (t_{62}).

length of waveguides:

10.0000

5.9000

6.0000

7.3700

6.9000

5.6200

6.0200

5.6200

6.9000

7.3700

6.0000

5.9000

10.0000

Fig. 4.9

19.0500 9.5250 ---------- width and height of ridged waveguide housing.

0.0000 0.0000 5.0250 9.5250 ---------- position (e_1,d_1), width (w_1), height (t_1).

14.025 0.0000 5.0250 9.5250 ---------- position (e_2,d_2), width (w_2), height (t_2).

length of waveguides:

5.0000

1.1880

11.5880

6.7750

11.6900

7.9160

11.6900

6.7750

11.5880

1.1880

5.0000

Fig. 4.10

22.8600 10.1600 ---------- width and height of ridged waveguide housing.

11.1800 0.0600 0.5000 10.1000 ---------- position (e_1,d_1), width (w_1), height (t_1).

11.1800 0.0000 0.5000 0.0600 ---------- position (e_2,d_2), width (w_2), height (t_2).

length of waveguides:

7.0000

0.6260

14.3640

5.2850

14.6950

6.8470

14.7170

6.8470

14.6950

5.2850

14.3640

0.6260

7.0000

Fig. 4.11

25.4000 19.0500 ---------- width and height of ridged waveguide housing.

5.0800 2.5400 15.2400 2.5400 ---------- position (e_1,d_1), width (w_1), height (t_1).

114300 5.0800 2.5400 13.9700 ---------- position (e_2,d_2), width (w_2), height (t_2).

length of waveguides:

95.7600

2.5600

9.5200

18.5700

3.8000

24.0300

3.6600

24.6300

3.6600

24.0300

3.8000

18.5700

9.5200

2.5600

95.7600

Fig. 4.12

22.8600 10.1600 ---------- width and height of ridged waveguide housing.

9.6520 3.0480 3.5560 7.1120 ---------- position (e_1,d_1), width (w_1), height (t_1).

3.8100 0.0000 15.2400 1.0160 ---------- position (e_2,d_2), width (w_2), height (t_2).

length of waveguides:

10.0000

3.1740

11.5530

10.2860

7.7870

14.4300

7.0840

15.3000

7.0840

14.4300

7.7870

10.2860

11.5530

3.1740

10.0000

Fig. 4.13

22.8600 10.1600 ---------- width and height of ridged waveguide housing.

9.6520 5.0800 3.5560 5.0800 ---------- position (e_1,d_1), width (w_1), height (t_1).

10.1600 2.5400 2.5400 2.5400 ---------- position (e_2,d_2), width (w_2), height (t_2).

length of waveguides:

10.0000

4.9380

10.0190

12.4410

7.3160

15.5490

6.8480

16.1190

6.8480

15.5490

7.3160

12.4410

10.0190

4.9380

10.0000

Fig. 4.14

16.0000 8.0000 ---------- width and height of first waveguide housing.

16.0000 16.0000 ---------- width and height of ridged waveguide housing.

8.0000 16.0000 ---------- width and height of last waveguide housing.

0.0000 0.0000 3.5000 3.5000 ---------- position (e_1,d_1), width (w_1), height (t_1).

12.5000 12.5000 3.5000 3.5000 ---------- position (e_2,d_2), width (w_2), height (t_2).

length of waveguides:

10.0000

19.0000

10.0000

A.2 Circular Waveguide Structures

Please refer to Fig. 5.1 for ridge locations and cross section. All dimensions are in millimeters and angles (p and w) are in degree.

Fig. 5.5

6.0000 ---------- radius of circular ridged waveguide housing.

2.0000 -97.50 4.0000 15.00 ---------- position (a_1, p_1), radius (r_1), width (w_1).

2.0000 82.50 4.0000 15.00 ---------- position (a_2, p_2), radius (r_2), width (w_2).

length of waveguides:

20.0000

7.0000

20.0000

Fig. 5.7

6.5000 ---------- radius of circular ridged waveguide housing.

4.0000 90.00 2.5000 360.00 ---------- position (a_1, p_1), radius (r_1), width (w_1).

6.5000 0.00 0.0000 0.00 ---------- position (a_2, p_2), radius (r_2), width (w_2).

length of waveguides:

10.0000

0.3010

12.8560

3.2970

13.5060

4.1900

13.5570

4.1900

13.5060

3.2970

12.8560

0.3010

10.0000

Fig. 5.8

6.5000 ---------- radius of circular ridged waveguide housing.

1.0000 84.00 5.5000 12.00 ---------- position (a_1, p_1), radius (r_1), width (w_1).

1.0000 264.00 5.5000 12.00 ---------- position (a_2, p_2), radius (r_2), width (w_2).

length of waveguides:

10.0000

3.3680

4.5130

9.4090

3.6330

10.8240

3.6330

9.4090

4.5130

3.3680

10.0000

Fig. 5.9

6.5000 ---------- radius of circular ridged waveguide housing.

1.0000 84.00 5.5000 12.00 ---------- position (a_1, p_1), radius (r_1), width (w_1).

1.0000 219.00 5.5000 12.00 ---------- position (a_2, p_2), radius (r_2), width (w_2).

1.0000 309.00 5.5000 12.00 ---------- position (a_3, p_3), radius (r_3), width (w_3).

length of waveguides:

10.0000

2.4730

8.9900

7.2510

8.1970

8.5290

8.1970

7.2510

8.9900

2.4730

10.0000

Fig. 5.10

6.5000 ---------- radius of circular ridged waveguide housing.

1.0000 84.00 5.5000 12.00 ---------- position (a_1, p_1), radius (r_1), width (w_1).

1.0000 174.00 5.5000 12.00 ---------- position (a_2, p_2), radius (r_2), width (w_2).

1.0000 264.00 5.5000 12.00 ---------- position (a_3, p_3), radius (r_3), width (w_3).

1.0000 -6.00 5.5000 12.00 ---------- position (a_4, p_4), radius (r_4), width (w_4).

length of waveguides:

10.0000

3.1970

4.9410

9.0980

3.9630

10.5410

3.9630

9.0980

4.9410

3.1970

10.0000

Fig. 5.11

6.5000 ---------- radius of circular ridged waveguide housing.

0.0000 84.00 6.5000 12.00 ---------- position (a_1, p_1), radius (r_1), width (w_1).

0.0000 264.00 3.0000 12.00 ---------- position (a_2, p_2), radius (r_2), width (w_2).

3.0000 180.00 0.7500 180.00 ---------- position (a_3, p_3), radius (r_3), width (w_3).

length of waveguides:

10.0000

3.5910

2.0850

9.0130

0.8880

10.1720

0.8880

9.0130

2.0850

3.5910

10.0000

Fig. 5.12

6.5000 ---------- radius of circular ridged waveguide housing.

1.5000 84.00 5.0000 12.00 ---------- position (a_1, p_1), radius (r_1), width (w_1).

1.0000 0.00 0.5000 360.00 ---------- position (a_2, p_2), radius (r_2), width (w_2).

length of waveguides:

10.0000

2.3300

5.1940

7.5760

4.1030

9.0390

4.1030

7.5760

5.1940

2.3300

10.0000

Fig. 5.13

6.5000 ---------- radius of circular ridged waveguide housing.

1.5000 84.00 5.0000 12.00 ---------- position (a_1, p_1), radius (r_1), width (w_1).

1.0000 45.00 0.5000 90.00 ---------- position (a_2, p_2), radius (r_2), width (w_2).

1.0000 225.00 0.5000 90.00 ---------- position (a_3, p_3), radius (r_3), width (w_3).

1.0000 264.00 5.0000 12.00 ---------- position (a_4, p_4), radius (r_4), width (w_4).

length of waveguides:

10.0000

3.0590

4.8950

8.4520

3.6950

9.7710

3.6950

8.4520

4.8950

3.0590

10.0000

Fig. 5.14

5.4000 ---------- radius of circular ridged waveguide housing.

3.6600 85.00 1.7400 10.00 ---------- position (a_1, p_1), radius (r_1), width (w_1).

2.0000 85.00 3.4000 10.00 ---------- position (a_2, p_2), radius (r_2), width (w_2).

2.0000 103.00 3.4000 10.00 ---------- position (a_3, p_3), radius (r_3), width (w_3).

2.0000 121.00 3.4000 10.00 ---------- position (a_4, p_4), radius (r_4), width (w_4).

2.0000 139.00 3.4000 10.00 ---------- position (a_5, p_5), radius (r_5), width (w_5).

2.0000 157.00 3.4000 10.00 ---------- position (a_6, p_6), radius (r_6), width (w_6).

2.0000 175.00 3.4000 10.00 ---------- position (a_7, p_7), radius (r_7), width (w_7).

2.0000 175.00 1.7400 10.00 ---------- position (a_8, p_8), radius (r_8), width (w_8).

length of waveguides:

10.0000

5.3390

6.2740

5.7930

6.6960

6.6960

5.7930

6.2740

5.3390

10.0000

PUBLICATIONS

[1] S.Y. Yu and J. Bornemann, "Classical eigenvalue mode-spectrum analysis of multiple ridged rectangular and circular waveguides for the design of narrowband waveguide components", Accepted to be published at International Journal of Numerical Modeling.

[2] S.Y. Yu and J. Bornemann, "Mode spectrum eigenvalue formulation for irregular waveguides and its application to waveguide component design", *Proc. German Microwave Conf. (GeMiC)*, pp. 360-363, Hamburg, Germany, Mar. 2008.

[3] K. Rambabu, H.A. Thiart, J. Bornemann and S.Y. Yu, "Ultrawideband printed-circuit antenna", *IEEE Trans. Antennas Propagat.*, Vol. 54, pp. 3908-3911, Dec. 2006..

[4] S.Y. Yu and J. Bornemann, "A simple eigenvalue formulation for the mode spectrum analysis of nonstandard waveguides", *PIERS 2003 Proceedings*, p. 230, Singapore, Jan. 2003.